AD_____

A FINITE-ELEMENT MODEL ANALYSIS OF THE PROTECTION PROVIDED BY ARMY AVIATOR HELMETS TO THE HUMAN HEAD AND NECK

FINAL REPORT

by

Y. King Liu
Robert L. Benedict
Sachio Nakamura
Glen O. Njus

April 1983

Supported by:

US Army Medical Research and Development Command
Fort Detrick, Frederick, Maryland 21701

Contract No. DAMD17-81-C-1186

College of Engineering
University of Iowa
Iowa City, Iowa 52242

SECURITY CLASSIFICATION OF THIS PAGE (When Data Entered)

REPORT DOCUMENTATION PAGE

READ INSTRUCTIONS BEFORE COMPLETING FORM

1. REPORT NUMBER	2. GOVT ACCESSION NO. / 3. RECIPIENT'S CATALOG NUMBER
4. TITLE (and Subtitle): A Finite-Element Model Analysis of the Protection Provided by Army Aviator Helmets to the Human Head and Neck	5. TYPE OF REPORT & PERIOD COVERED: Final Report Sept. 1, 1981 - Sept. 1982 / 6. PERFORMING ORG. REPORT NUMBER
7. AUTHOR(s): Y. King Liu, Robert L. Benedict, Sachio Nakamura and Glen O. Njus	8. CONTRACT OR GRANT NUMBER(s): DAMD17-81-C-1186
9. PERFORMING ORGANIZATION NAME AND ADDRESS: College of Engineering, University of Iowa, Iowa City, IA 52242	10. PROGRAM ELEMENT, PROJECT, TASK AREA & WORK UNIT NUMBERS: 62777A. 3E162777A878. AG.146.
11. CONTROLLING OFFICE NAME AND ADDRESS: US Army Medical Research and Development Command, Fort Detrick, Frederick, Maryland 21701	12. REPORT DATE: April 1983 / 13. NUMBER OF PAGES: 84
14. MONITORING AGENCY NAME & ADDRESS(if different from Controlling Office): U.S. Army Aeromedical Research Labs., Fort Rucker, Alabama 36362	15. SECURITY CLASS. (of this report): Unclassified / 15a. DECLASSIFICATION/DOWNGRADING SCHEDULE

16. DISTRIBUTION STATEMENT (of this Report)

Approved for public release; distribution unlimited

17. DISTRIBUTION STATEMENT (of the abstract entered in Block 20, if different from Report)

18. SUPPLEMENTARY NOTES

19. KEY WORDS (Continue on reverse side if necessary and identify by block number)

Helmets (Army aviator, football); Shell; Stiffness properties; Inertial properties; Contact; Impact; Biomechanics; Three-dimensional digitizer

20. ABSTRACT (Continue on reverse side if necessary and identify by block number)

This report documents the results of a study aimed at obtaining the spatial and temporal distribution of loads on the headform as a result of a crown impact to Army aviator helmets using a classic headform-helmet drop test. In the actual drop test, only 2 measurements were made: the impact force time history between the helmet shell and a rigid surface and the acceleration time history of the center of gravity (C.G.) of the magnesium headform.

A mathematical model of the drop test was developed using a flexible body

DD FORM 1 JAN 73 1473 EDITION OF 1 NOV 65 IS OBSOLETE

SECURITY CLASSIFICATION OF THIS PAGE (When Data Entered)

extension to DADS, a general-purpose nonlinear dynamic analysis program previously completed at the University of Iowa. To exercise the model, it was necessary to experimentally determine the following helmet and headform input parameters:

(1) The center of gravity (C.G.) was obtained using a variant of the differential weighing technique.

(2) The principal mass moments of inertia about the C.G. was found by the repeated application of the well-known torsional pendulum method.

(3) The 3-dimensional (3-D) coordinates of many points of the helmet shell surface was determined via an innovative technique for 3-D digitization using an electronic caliper with a computer algorithm.

(4) The dimensions of the gap between the headform and helmet liner were obtained using an alginate dental impression material as a cast between the two objects.

(5) The material properties of the helmet shell and liner were found through standard materials testing methods using a MTS machine.

In the mathematical model, the headform and the contact surface are assumed to be rigid. The liner material is modeled as a series of nonlinear springs attached to a flexible shell. The area of contact between the crown of the helmet and the rigid surface is also modeled by a series of 5 nonlinear springs of high stiffness.

The model, with the appropriate geometric, material and inertial properties simulating the SPH-4 and Al Army aviator helmets, was run on the PRIME 750 computer. The results permit the following conclusions and recommendations:

I. Comparing the predicted response of the SPH-4 and the Al, we see that helmets which exhibit similar gross behavior, i.e., the acceleration of the C.G. of the headform and the ground contact force, may have entirely different headform contact pressure responses.

II. The flexibility of the Al shell allows a large crown contact pressure to develop. The stiffer SPH-4 distributes the contact pressure to the front and back of the headform. The peak headform contact pressure is higher in the Al than the SPH-4.

III. For the liner material used, a shell stiffness somewhere between the Al and the SPH-4 will allow the most uniform contact pressure distribution.

IV. The spatial and temporal distribution of loads on the rigid headform could serve as a more sensitive method of comparing the performance of different helmets via the drop test.

V. The analysis procedure used here is capable of incorporating the flexibility of the headform, e.g., humanoid headforms and/or cadaveric heads.

PREFACE

Funding for this project was provided primarily through Contract No. DAMD 17-81-C-1186 from the U.S. Army Medical Research & Development Command (USAMRDC), Ft. Detrick, MD. Mr. Joseph Haley of USAARL acted as the contracting officer's technical representative (COTR). His understanding of the fluctuations in any research effort are very much appreciated. After the expiration of the contract period, the partial support provided by the Helen Streiffer Fund of the University of Iowa Foundation and Grant No. GM 26608-03 from the National Institutes of General Medical Sciences (NIGMS) of the NIH is gratefully acknowledged.

The flexible body extension version of the general purpose nonlinear dynamics analysis program, DADS, used in the modeling effort, was developed under the sponsorship of the Army Research Office under Project ARO 16635-M. The authors would like to acknowledge the courtesy of Drs. A.A. Shabana and R.A. Wehage in permitting us to use their program.

Citations of commercial organizations and trade names in this report do not constitute an official Department of Army endorsement of approval of the products or services of these organizations.

TABLE OF CONTENTS

TABLES

FIGURES

I. Introduction

Simulation of the head and neck during an impact event requires knowledge of the spatial and temporal distribution of loads on the head. A headform-helmet drop test is often used to determine the helmet impact force and headform acceleration history. These global measures, while useful, are not sufficient for a head and neck simulation. This study developed a model for helmets that predict the transient distribution of loads applied to the headform during an impact event. In order to verify the developed computational technique, the headform-helmet drop test is simulated and the resulting global force and acceleration measures are compared to experiments.

The Army Aviator production helmet, SPH-4, and an experimental helmet designated A1 were used in this study for both drop tests and simulations. Simulations were also performed for two helmets with the same shell shape and liner material as the SPH-4 and A1 but with a "rigid" as well as a soft shell.

II. Analysis Procedure

The system was divided into four components: the impact surface, the shell, the liner, and the headform. The headform and the impact surface were modeled as rigid bodies. Only the shape and rigid body inertial properties of the headform were used in the analysis. Figure 1 depicts a plane view of the three-dimensional model.

The dynamic analysis was carried out by a flexible body extension to the DADS[1] nonlinear dynamic analysis program. This method for transient dynamic analysis of mechanical systems consisting of constrained rigid and flexible bodies was developed at the University of Iowa[2]. Overall displacement of elastic bodies was represented by superposition of small elastic displacements on the large displacement of the body reference frames. For each elastic body two sets of generalized coordinates were employed. First, reference

generalized coordinates defined the location of a body-fixed coordinate system with respect to an inertial reference frame. This coordinate system had its origin rigidly affixed to a point on the body. Second, the generalized coordinates corresponding to elastic deformation were introduced through a modal analysis method. This set of coordinates was defined with respect to the body-fixed coordinate system.

The system equations of motion were formulated using Lagrange's equations. Since elastic coordinates associated with a given elastic body are defined locally, a finite element approach was used to assemble the elements within the body, thus eliminating excess dependent variables. However, constraints between adjacent bodies were not used to explicitly eliminate additional dependent variables. Rather, a Lagrange multiplier technique was employed. Substructuring methods and generalized coordinate partitioning were employed to reduce the number of degrees of freedom. The large displacements resulted in inertia-variant problems with a corresponding variant eigenspectrum. The method allowed for adjustment of the number of elastic degrees of freedom so that the dominant modes are included in the dynamic model. The elastic deformation was represented by lower (dominant) mode dynamic response and higher mode static effects.

The equations of motion and constraints were solved numerically using a direct integration method. Numerical examples have shown that the results obtained by this method and those available in the literature are in good agreement.

As the deformations of the helmet shell were expected to be small during the impact under consideration, the shell was modeled using linear elastic small deformation plate theory. The shell is discretized into three-node triangular plate finite elements. Figures 2 and 3 depict the discretized

model of the helmet shell. The SPAR finite element program was used to obtain the shell stiffness matrix, mass matrix, and mode shapes.

Modeling of the foam liner material was the most complex aspect of the analysis. The material was expected to undergo relatively large deformations during impact and thus the response of the material cannot be reasonably modeled by using a linear constitutive relationship. Since not all of the liner is in initial contact with the headform, the gap between the headform and the liner material must be taken into account in the simulation. In order to model these aspects of the liner, it was divided into small regions and each region is represented by a nonlinear one-dimensional element. A typical force-deformation curve for an element is shown in Fig. 4. The gap was taken to be the average distance between the liner and the headform over the element area. Until the headform has advanced to close the gap, there was no response from the liner. The use of a trilinear force-deformation relation was well justified by the form of the experimentally determined force-deformation relation shown in Fig. 5. Several typical liner materials have been observed to display this stiffening character.

The impact surface was modeled as a set of linear elements with a gap capability. These elements were distributed around the crown of the helmet over the region which was reasonably expected to come into contact with the impact surface. The impact surface was assumed to be flat and the element gaps were determined by the shell geometry.

The initial condition assumed the same pre-impact velocity to the helmet and headform. The headform initial position was one that just touched the helmet liner at two points located in the posterior and anterior regions of the plane of mid-sagittal symmetry. An initial gap between the helmet liner and headform existed over the crown region. The initial position of the

helmet was one that yielded a small initial gap between the shell and the impact surface, i.e., the condition of the system at the instant before the impact.

A constant gravitational force was included on the helmet and the headform. The helmet was constrained to move straight downward and rotation was prevented. The headform was also constrained to move straight downward but rotations were allowed.

In this study the simulation was performed from the instant before impact until the time when the helmet has rebounded from the impact surface.

III. Material and Geometric Properties

A. Shell

The shell material properties for the Al and SPH-4 helmets were obtained by material testing. All samples were cut with a table saw using a laminated blade. The width of the specimens was approximately 1 cm. for a length of 8 to 10 cm. The samples from the Army helmets were cut such that half of them had a surface layer fiber orientation directed along the length of the specimen. The remainder were cut such that the surface fiber direction was transverse to the axis of loading. A total of 15 tests were conducted, three for each condition. For typical results, see Figures 6 and 7. Density was determined using a volumetric displacement procedure.

All tests were conducted on a closed loop servo-hydraulic Materials Testing System (MTS) machine. Specimens were mounted in friction grips and tests were run with a ramp extension rate of 1.27 mm/min (0.05 in/min). Strain was measured using 120 Ω strain gages in a Wheatstone bridge circuit. Two arm bridges were used for both longitudinal and latitudinal strains and so placed that bending effects were eliminated. The bridge circuit was amplified using Honeywell Accudata 218 signal conditioners. Hardcopy output was

recorded on an X-Y plotter which graphed the force output versus the strain obtained.

Due to the strip nature of the specimens, no complete stress-strain curves were generated. However, for the purposes of this study, Young's modulus, E, and Poisson's ratio, ν , were the only material properties needed. Some difficulty was encountered while testing the Army Al helmet specimens. At approximately 250 N the fiberglass layers failed in shear and the specimens would pull out of the grips. Until this point though, there was little or no relative displacement between the fiberglass layers. This was determined by coating the edges with a polyurethane layer, step loading the specimen, and at each load increment, looking for cracks in the plastic. As can be seen in Fig. 6 there was little difference in the curves with respect to different surface fiber directions. For the modeling aspect of this report a single Young's modulus was chosen for each Army helmet.

B. Foam Liner

New helmet foam liners and the liners from an Al and SPH-4 were tested. The density of all liners was determined using a volumetric displacement procedure and was found to be 0.077 ± 0.003 g/cm. No difference in impact characteristics were seen between different liner sources and they will not be distinguished in the remainder of this report. Sheet specimens were taken from the lateral aspect of the crown such that the radius of curvature was minimized. Cylindrical samples were chosen at random and were cut with a one inch plug cutter.

All impact tests were conducted on a closed loop servo-hydraulic Materials Testing System (MTS) machine (Model 810) rated at 10 kN. Displacements were monitored with a LVDT attached as an integral part of the MTS actuator. Hardcopy output was a photograph from a storage oscilloscope

which displayed the outputs of the LVDT and MTS machine's load cell. Displacement control, with a triangle wave forcing function, was used and peak displacements ranged from 3 to 12 mm. Rise times varied from 12 to 26 msec. All tests were run with the specimen being placed on a large steel plate bolted to the top of the actuator. Specimens were oriented such that the line of impact would be normal to the inner liner surface. The impactor was a one-inch diameter steel rod attached to a stationary load cell (see Fig. 8). Initial geometries were determined with the aid of a precision micrometer.

As indicated above, two different types of tests were run. The first of these was with a piece of foam liner where the area was much larger than that of the impactor, i.e., an "infinite" sheet. Due to the radius of curvature a backing was needed for complete support. This was achieved by molding PMMA to the piece of foam in the orientation desired. A preload of 5 N was used to maintain position prior to the test. The second type of specimen was cylindrical in shape with the same diameter as that of the impactor. These tests were run with a 20 N preload. As would be expected, the two different types of tests had similar shaped force displacment curves. However, sheet specimens tended to absorb approximately 15 percent more energy due to tearing of the compressed plug from the surrounding material (see Figures 9-11). All curves were characterized by an initial linear region where the foam approximated an isotropic linear elastic material (see curve 7 in Figure 11). At about 20 percent strain and 500 N there was a fairly abrupt region of transition. Beyond this point there was a much lower slope where disruption of the foam cellular structure occurs. It was in this area that most of the energy absorption took place. There was a second transition region (see curve 3 in Fig. 9) at about 75 percent strain where the stiffness increased. This

behavior has been termed "lock-up" and occurred when the cellular form of the foam acted as a stiff unit. At this strain level the foam was almost a uniformly dense material with very little energy absorption capabilities. It should be kept in mind that the impact force-displacement curves were very much dependent on loading rates, i.e., rise times.

C. Gap Generation

The contact area between the metal headform and the helmet liner was experimentally determined. Selected points on the helmet shell were marked. At these points 1/16 inch holes were drilled through the helmet shell and the liner. This hole was angled such that it would be normal to the shell surface. Using a pen, these points were labeled by indenting the foam liner. The metal headform was also marked using labeling tape (periods for the points) with an identifying numerical tag.

An alginate dental impression material Jeltrate® was used for casting the gap. This material when mixed is a liquid of low viscosity but quickly (180 sec) sets to a rubbery consistency. The helmet was filled with the liquid impression material and the metal headform positioned. Once the Jeltrate® had set, the headform and cast were removed. The casting clearly showed the metal headform and the helmet liner points. The cast was then cut at these points and the thickness measured with a micrometer.

For several selected helmet drop tests a sheet of carbon paper was placed between the metal headform and the helmet foam liner. The carbon side was positioned facing the liner. The drop tests were then conducted according to standard procedure. In this manner regions were marked on the liner where the headform caused deformations during the drop. In addition, using shading patterns, rough estimates of relative displacements could be made. The outlines of these impact contact regions were demarcated by indenting the

liner with a pen. Then using the same procedure as above a casting was made. The cast was highlighted with ink and then photographed.

IV. Helmet — Headform Drop Tests

The behavior of the helmet in a dynamic environment was evaluated by drop tests. A medium-size magnesium headform was provided by the Contract technical Monitor (CTM), U.S. Army Aeromedical Research Laboratories, Ft. Rucker, AL. At the approximate center of gravity of the headform an accelerometer (Endevco 2264, 2000 G) was attached with its sensitive axis oriented vertically. The drop method conformed in general to the ANSI/ASTM F 429-75 standard. The testing setup, purchased from Humanoid Systems, Canson, CA, used no guide assembly since only crown impacts were conducted. The experimental setup shown in Fig. 12 consisted of a channel frame with an electromagnet attached at the center of its horizontal cross member. The helmet, fitted with the headform, was held by the electromagnet. The base of the apparatus was a structural steel plate 5.08 cm thick. The midportion of the plate was machined out to accomodate CNSTUL 20 kN force transducer (manufactured by PCB Piezotronics, Inc.). The height from the base to the electromagnet was 86 cm. For both the SPH-4 and the Al helmet, the drop height was approximately 59 cm.

The drop test begins with the interruption of the current to the electromagnet by flipping a switch. The transient events were recorded by the appropriate above-mentioned transducers, signal conditioners (Honeywell Accudata 218 series), tape recorder (Honeywell FM Tape Recorder System 5600E and storage oscilloscope (Tektronix 7623A). The acquired analog signals were converted to digital form, through A/D conversion available on our PDP 11/34 minicomputer for further processing. The final display can be either in Polaroid photographs of the storage oscilloscope or computer graphics display.

V. Models

Initially three separate simulations were performed: one with a rigid helmet shell, one with a helmet shell model based on the Al, and one with a model based on the SPH-4. The shapes of the helmet shell and liner were found to be identical in the Al and the SPH-4. The shell material in the Al is much less stiff than that of the SPH-4 and the Al material is thinner. The three simulations represented a series of helmets with identical shell shape and liner material but differing shell stiffness.

The shell was constructed of a laminated fibrous composite material. The orientations of the lamina varied from point to point on the shell and from helmet to helmet at the same point. A number of rectangular specimens were cut from each helmet at various locations and orientations. It was found that the material properties of the laminate are not heavily orientation dependent. The material was then assumed to be transversely isotropic. The values obtained in the tensile tests were averaged to obtain a single Young's modulus and Poisson ratio for each shell material. Shell material properties used in the analysis are presented in Table 1.

Sample helmets were cut into radial sections so that the shell and liner thickness could be measured. Neither the shell nor the liner thickness varied abruptly. The shell shape and the headform shape were measured using either a 3-D sonic digitizer (Graf-Pen) or the electronic caliper system described in Appendix A. The measured shell shape was used to construct the finite element model mesh.

It was expected that the contact stress distribution will depend heavily on the initial gap between the headform and liner. Rather than computing this gap by differencing the measured headform and shell plus liner shape, it was decided to measure the gap directly. A quick setting liquid plastic was

poured into an inverted helmet with the headform in place. After the plastic had set, it was removed, sectioned and its thickness measured. These measurements were used to specify the initial gap used in the analysis.

The SPAR[3] finite element program was used to compute the shell stiffness matrix, mass matrix, eigenvalues, and mode shapes. The mass of the liner material was distributed over the shell in the areas of labeled nodes in Fig. 13. Each finite element shell model consisted of 83 nodes connected by triangular plate elements. The first 16 modes were used in the analysis of the SPH-4 and the first 17 modes were used for the A1. Table 2 contains the eigenvalues used. Plots of the mode shapes are found in Appendix B.

Compression tests were performed on samples of the shell liner material. Figure 5 displays some typical results. Based on these tests the liner material was modeled as being trilinear as shown in Fig. 4. The stress-strain slopes used are found in Table 3. The effective spring constants of the one-dimensional elements used to model the liner were computed on the basis of the material properties and the extent of liner material around each node. A viscous damping factor was included in the liner material.

The liner was modeled as 32 one-dimensional elements that were attached to the shell at the points labeled in Fig. 13. The area over which the liner elements are distributed was chosen to cover the possible contact area noted from the carbon paper impressions made during drop tests. An additional 5 linear one-dimensional gap elements were used to model the impact surface. These were attached to the nodes labeled 3, 12, 13, 29 and 64 in Fig. 13.

VI. Results and Discussion

The headform helmet drop test was simulated using the finite element model of Army helmets developed in Section IV. In this section, computational results for the SPH-4, A1 and the rigid shell are presented.

Figures 14(a) to (d) are the plots of the numerical predictions for the SPH-4 helmet, corresponding to (a) position, (b) velocity, (c) acceleration, and (d) impact force between the ground and the SPH-4 shell. Similarly, Figs. 15(a-d) and 16(a-d) present the corresponding results for the Al and rigid shell, respectively. In Fig. 14(a), the solid line shows the position of the crown of the SPH-4 shell (node 3 in Fig. 3) and the dotted line shows the position of the crown of the headform, as functions of time. Nonlinear springs, simulating the ground, became active when the distance between the origin and the shell surface was less than 10 millimeters. In these figures, it was observed that the distance between the SPH-4 shell and the headform did not change very much during impact. The same was true for the rigid shell, as shown in Fig. 16(a). On the other hand, the distance between the Al shell and the headform changes substantially as shown in Fig. 15(a). This was an expected result, since the stiffness of the Al shell was about 30 times lower than that for the SPH-4. The Al shell can deform more easily so that two points can approach more closely than those in the SPH-4. Figure 14(b) shows the velocity history of the SPH-4 shell and the headform. During experimental head drop, the velocity of the shell and headform at impact was -3.42 m/sec. Therefore, the initial conditions of the numerical experiment were chosen so that the same velocity can be observed. In Fig. 14(b), both the SPH-4 shell and the headform approached the ground at a downward velocity of -3.24 m/sec. The shell, hitting the ground first obtained positive upward velocity gradually after t = 0.004 sec. due to the upward reaction force from the ground. The headform moving toward the ground, hits the liner at t = 0.006 sec giving the shell a negative velocity. The shell bounces between the ground surface and the headform. This oscillatory behavior can be observed in Fig. 14(b). The numerical solution for the rigid shell gave almost identical

results as that of the SPH-4, as shown in Fig. 16(b). Because of the flexibility of the shell, the numerical results for the Al helmet gave a smaller amplitude of velocity oscillatory behavior (Fig. 15[b]) than the other two helmets.

Fig. 14(c) is a plot of the acceleration history of the SPH-4 shell and the headform. In this figure, one can see the reaction forces between the shell and the headform as a result of impact. At t = 0.008 sec., the headform obtains an upward acceleration and the shell receives downward acceleration due to the impact between these two. By observing this feature, one can see that the next impact happens just after 0.01 sec. Thus, the acceleration of the shell changes sign several times during a single impact event. The acceleration history of the rigid shell yields a similar magnitude and pattern but fewer impacts between the shell and the headform can be seen in Fig. 16(c). In Fig. 14(c), the acceleration of the headform for the SPH-4 shell has two peaks. One peak is 1900 (m/sec^2) = 194 g at t = 0.008 and the second is 1250 (m/sec^2) = 127 g at t = 0.015, with a time difference of 0.0025 sec. Figure 17 is a plot of the experimental results. The observed acceleration history of the headform also has two peaks. The first peak has a magnitude of 160 g and the second peak 130 g, with a time difference of 0.002 sec. Thus, the acceleration histories of the numerical simulation and the actual experiment are in good agreement, not only in pattern but also in their magnitudes.

Figure 15(c) shows the numerical result of the acceleration time histories for the Al headform and helmet. One observes that the peak headform acceleration has a magnitude 1300 (m/sec^2) = 132 g. Figure 18 is a plot of the acceleration of the Al experimental data, whose peak is 120 g. Though the patterns look different, the magnitudes are close.

Figure 14(d) shows the computed impact force between the SPH-4 shell and the ground, and Fig. 17 shows the corresponding experimental result. For the computed results, the peak force is 3700 N with a time duration of 0.011 sec., while the experimental results show a peak force of 7500 N with a time duration of 0.010 sec. Even though the computed force is almost half the magnitude of the experimental results, the patterns are similar, having two almost identical peaks and time durations. Computed results for the rigid shell are plotted in Fig. 16(d) showing a peak value slightly higher than the results for the SPH-4. Figure 15(d) is a plot of the computed impact force between the Al helmet and the ground and Fig. 18 shows the experimental results for the Al helmet. The peak force of the computed results was 3700 N and for the experimental results, 6000 N. The pattern is also different and the numerical results has two peaks while the experimental results are unimodal.

Figures 19 (a) to (c) are the distribution history for the pressure between the shell and the headform for the SPH-4 helmet. First, the spatial three-dimensional helmet is projected to the x-y plane. Then the pressure levels at each node are expressed as the z-coordinate. Only selected time instances are presented here. At each time instance, two figures are drawn. One is a side view and the other a rear view of the pressure distribution. At $t = 0.0039$ sec., no pressure is observed between the shell and the headform. At $t = 0.0051$ sec., some small pressures are observed at the front and rear portions of the helmet. At time $t = 0.0060$ sec., shown in Fig. 19(a), no significant contact pressure is observed, even though the shell is at the lowest position in Fig. 14(a), the impact between shell and headform has not occurred yet. At time $t = 0.0072$, some of the liner material is compressed due to the impact and high pressure observed at the rear portion of the shell

(Node 10) with values of 0.58×10^6 N/m^2 at time t = 0.0072. Similar high pressure appears at the front portion of the shell (node 4) at time t = 0.0075. The contact area increases at time t = 0.0081. Then after t = 0.0099, those contact pressures decrease and die out at t = 0.0159 sec. During the impact, the crown of the shell (Node 3) never experiences the contact pressure. This is in good agreement with the experimental result.

Figures 20(a) to (c) show the pressure distribution of the Al helmet. The behavior is very different from the SPH-4 and it has some pressure at the crown (Node 3) at time t = 0.0069 and t = 0.0072. At time t = 0.0075 sec., high pressure appears at the rear portion (Node 10) and very high pressure (0.52×10^6 N/m^2) is generated at the crown at time t = 0.0081 sec. The same pressure can be observed at t = 0.0099 sec. After t = 0.012 sec., the pressure decreases at the crown and the pressures at the front and rear portions are not significant. The pressure at the crown disappears at t = 0.0159 sec. The significant difference between SPH-4 and Al is that the front and rear portions are load bearing portions for SPH-4, while the crown is the load bearing part for the Al helmet.

Figures 21(a) to (c) show pressure distribution for the rigid shell and gives behavior similar to the SPH-4 helmet, i.e., the SPH-4 helmet is more like a rigid shell.

Although the global SPH-4 predictions agree well with the drop test results, the agreement of the Al predictions with the drop test is less satisfactory. In order to further understand the effect of shell stiffness on the global predictions, a "soft" shell model was constructed. The shell of this model again used the same geometry as the SPH-4 and the Al, but the shell stiffness was 30 times smaller than that of the Al. The liner material characteristics and distribution were identical to those used in the Al and SPH-4.

Figures 22 (a) to (d) are plots of the predicted position, velocity, acceleration and impact force between the "soft" shell and ground. The impact force prediction for this model agrees qualitatively with that seen experimentally for the Al shell. The two peaks for the force curve (see the SPH-4 case) have merged into a single peak.

VII. Conclusions

From the above results, one can conclude the following:

1. The analysis procedure used is capable of good qualitative agreement with experimental results. Features observed in the gross behavior, i.e., acceleration of the center of gravity of the headform and the ground contact force, are predicted.
2. From the analysis, it is confirmed that the multiple peaks seen in the contact force in drop tests are due to the shell bouncing between the headform and the ground during the contact event.
3. Comparing the predicted response of the SPH-4 and the Al we see that helmets which exhibit similar gross behavior may have entirely different headform contact pressure responses.
4. Helmet shell flexibility can affect gross response measures only for a sufficiently large change in shell stiffness.
5. Comparing the predicted headform contact pressure distribution of the SPH-4 and the Al we note that the flexibility of the Al allows a large crown contact pressure to develop. The stiffer SPH-4 distributes the contact pressure over two regions in the front and back of the headform. The peak headform contact pressure is higher for the Al than for the SPH-4.
6. The headform acceleration and the shell contact force time history are gross measures of the helmet performance. Whether or not the pressure magnitudes are diminished, and by how much, can only be ascertained by examining the details of the contact impact phenomenon.

VIII. Recommendations

1. The most uniform contact pressure distribution is produced by a shell that is sufficiently stiff to prevent "large" local deformations at the point of impact, yet sufficiently flexible to allow a wide load distribution. For the liner material studied, a shell stiffness somewhere between that of the Al and the SPH-4 is recommended. It is suggested that a parametric optimization be conducted to determine the optimal shell stiffness.
2. Increasing the liner thickness in general decreases the initial stiffness but may also shift the transition or "toe" regions of the load-deformation curve. The effects of increasing liner thickness should be experimentally determined prior to exercising the model for different liners and/or thicknesses.
3. To augment the headform-helmet drop tests, ensemble quasistatic and dynamic tests of the helmet-headform system in a servo-controlled closed loop hydraulic material test machine should be undertaken.
4. The flexibility of the headform in drop tests involving humanoid headforms and cadavera should be incorporated in any future analyses. The analysis procedure used here is potentially capable of performing such a task; however, a general-purpose finite element program, e.g., ANSYS, will be less time consuming in the long run.
5. The spatial and temporal distribution of loads on the head predicted by this model could serve as a more appropriate load input to the homeomorphic finite element model of the head and neck[4].

References

1. Shabana, A.A. and Wehage, R.A. "A Coordinate Reduction Technique for Transient Analysis of Spatial Substructures with Large Angular Rotations," to be submitted to the Journal of Structure Mechanics, December 1982.

2. Shabana, A.A. and Wehage, R.A. "Variable Degree of Freedom Component Mode Analysis of Inertia Variant Flexible Mechanical Systems," ASME Paper No. 82-DET-93, to appear in the Journal of Mechanical Design.

3. SPAR Structural Analysis System Reference Manual, Whetstone, W.D., NASA CR 158970-1, December, 1978.

4. Hosey, R. and Liu, Y.K., "A Homeomorphic Finite Element Model of the Human Head and Neck," Chapter 18, Finite Element Methods in Biomechanics (Eds. Gallagher, Simon, Johnson, and Gross) John Wiley & Son, 1982, pp. 379-401.

Table 1: Shell Material Properties

Young's modulus E	17.914×10^9 erg/msec^2	0.6889×10^9 erg/msec^2
Poison's ratio ν	0.25	0.22
Mass density ρ	2100.0 erg/m^3	2100.0 erg/m^3

Table 2: Helmet Eigenvalues

Eigenvalues: 1)	6.902×10^3	8.912×10^6
2)	1.118×10^4	9.056×10^6
3)	1.942×10^5	9.157×1^6
4)	3.1068×10^5	9.235×10^6
5)	6.724×10^5	9.380×10^6
6)	1.9150×10^6	9.562×10^6
7)	4.0013×10^6	9.607×10^6
8)	4.9206×10^6	9.734×10^6
9)	5.7738×10^6	9.744×10^6
10)	6.0937×10^6	10.04×10^6
11)	9.845×10^6	10.23×10^6
12)	1.275×10^7	10.39×10^6
13)	1.8587×10^7	10.42×10^6
14)	2.1561×10^7	10.49×10^6
15)	2.6467×10^7	10.77×10^6
16)	2.6842×10^7	$10.[illegible]7 \times 10^6$
17)		11.21×10^6

Table 3: Liner Element Characteristics

Spring Displacement	< 0	0-3	3-7	7-15
Stiffness Modulus (Pa)	0	5×10^6	1×10^6	5×10^7

Plane View of Model

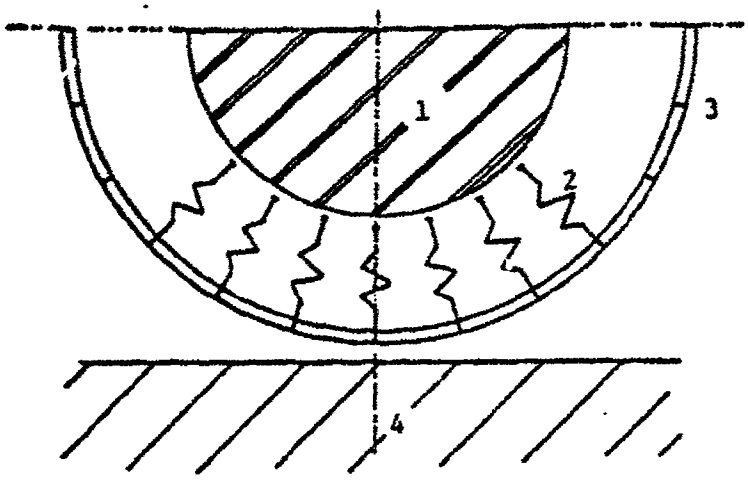

Figure 1. 1. Rigid Headform
2. Liner Material
3. Helmet Shell
4. Impact Surface

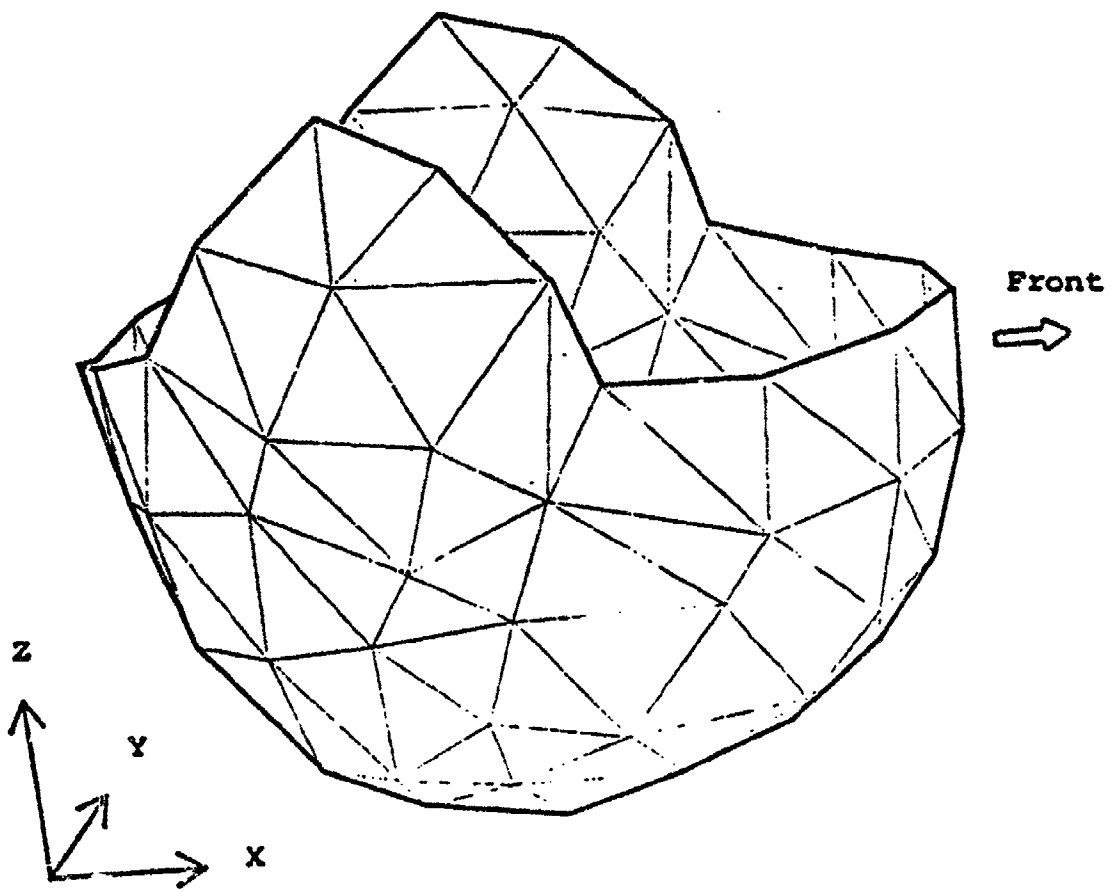

Figure 2. Three Dimensional View of U.S. Army Helmet

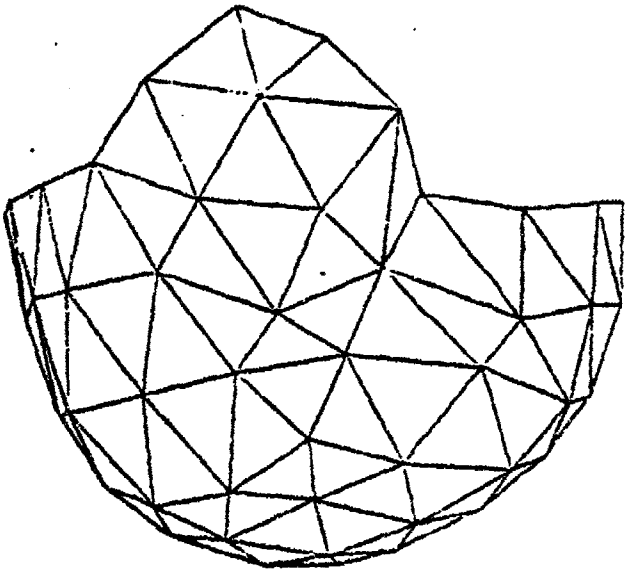

(a)

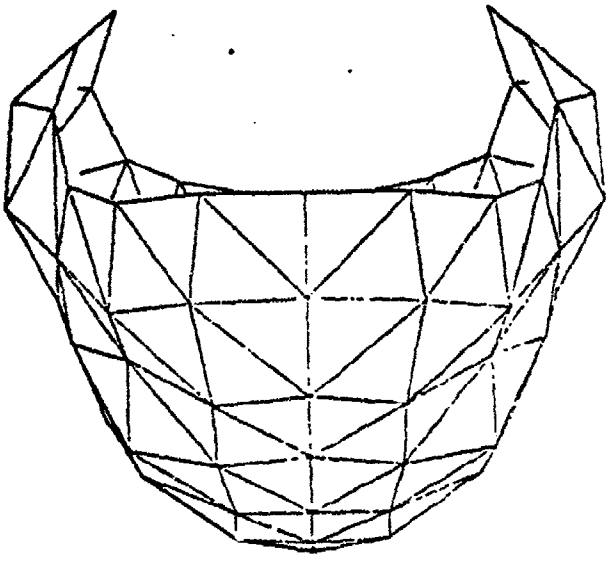

(b)

Figure 3. Side and Front Views of Army Helmet
(a) side view
(b) front view

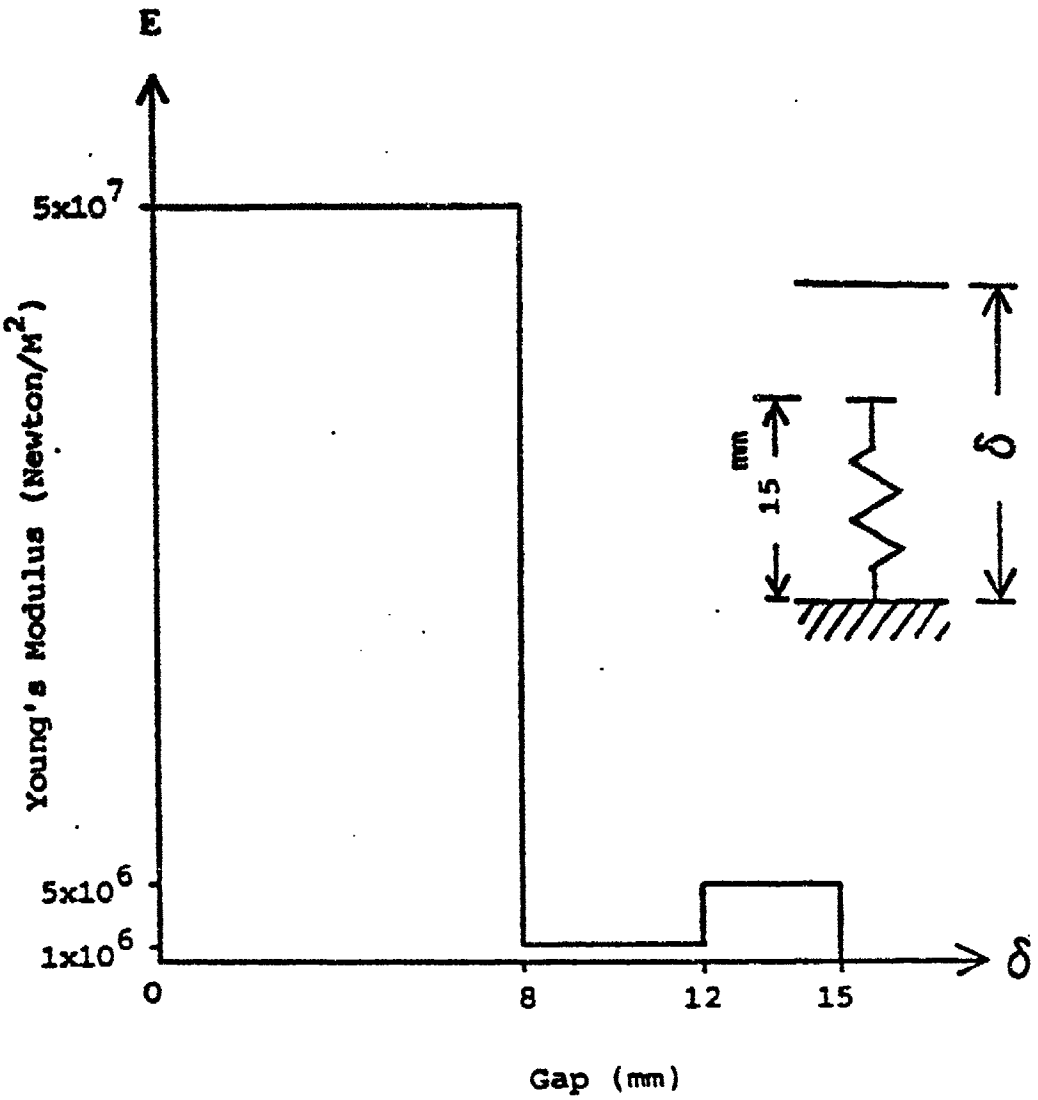

Fig. 4 Nonlinear Spring Characteristics

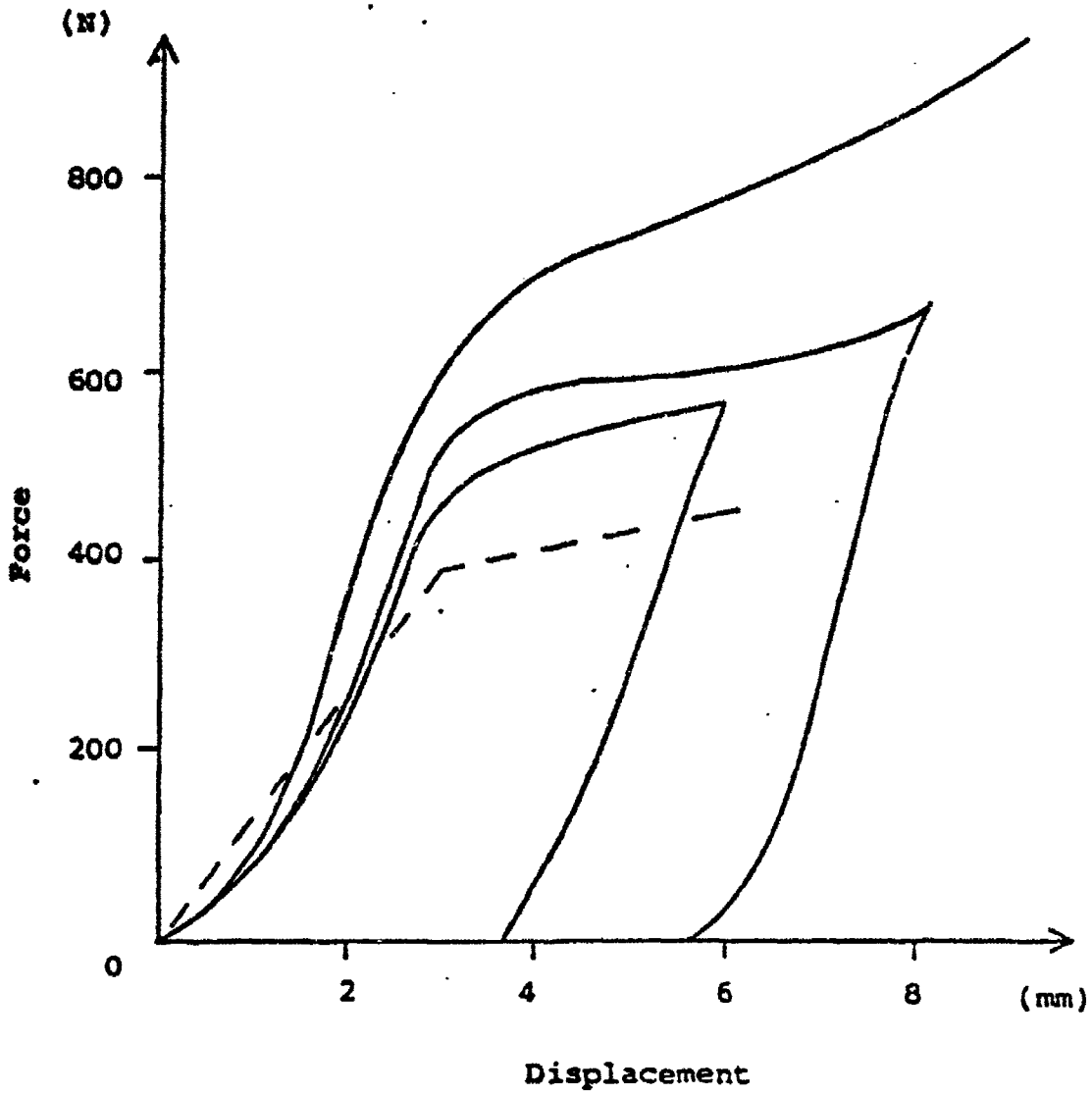

Fig. 5 Experimental Results of Liner Material

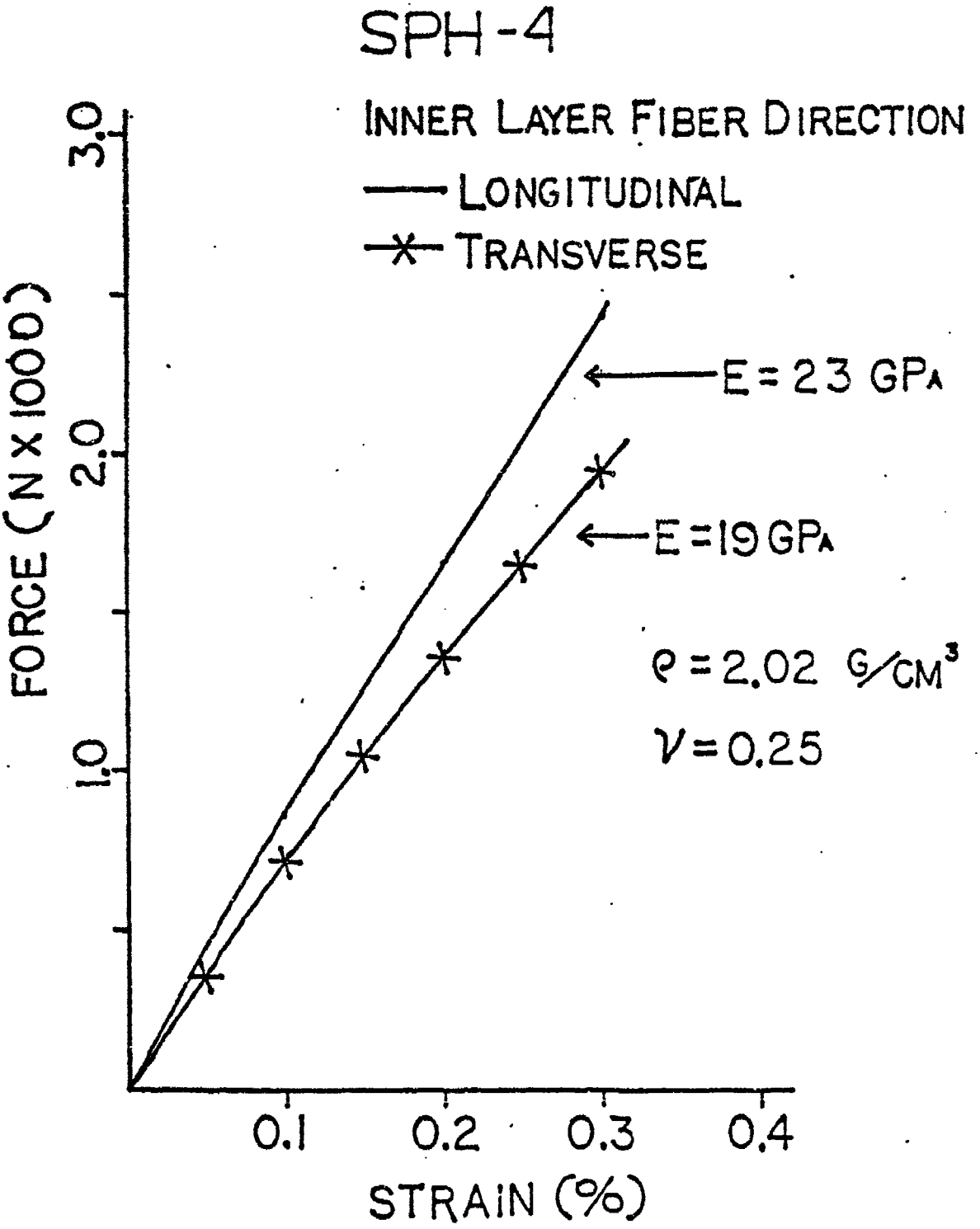
SPH-4
INNER LAYER FIBER DIRECTION
LONGITUDINAL
TRANSVERSE
E = 23 GPA
E = 19 GPA
ρ = 2.02 G/CM³
ν = 0.25
FORCE (N X 1000)
3.0
2.0
1.0
0.1
0.2
0.3
0.4
STRAIN (%)

Fig. 6

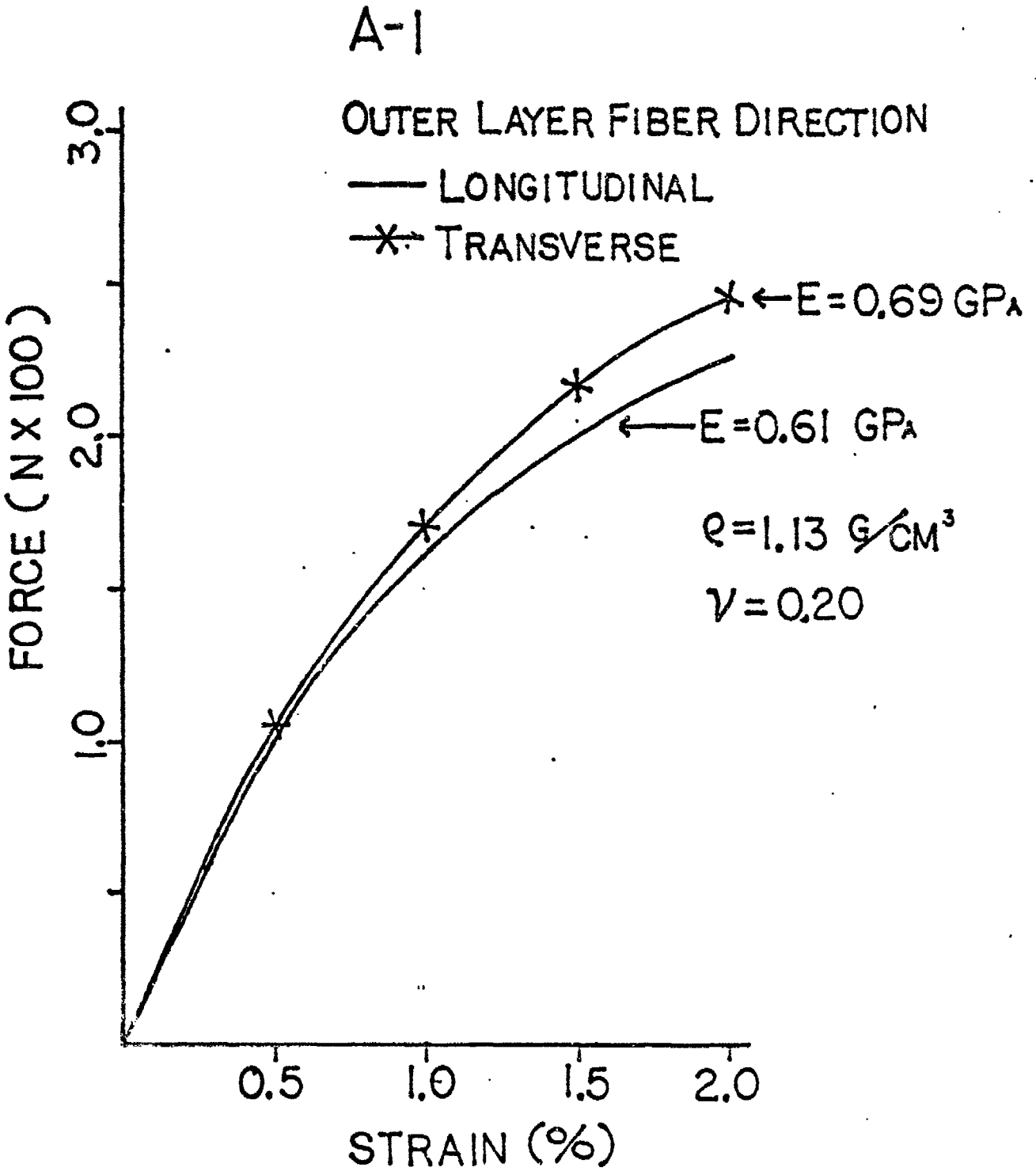
A-1
OUTER LAYER FIBER DIRECTION
LONGITUDINAL
TRANSVERSE
E=0.69 GPA
E=0.61 GPA
ρ=1.13 G/CM³
ν=0.20
FORCE (N X 100)
3.0
2.0
1.0
0.5
1.0
1.5
2.0
STRAIN (%)

Fig. 7

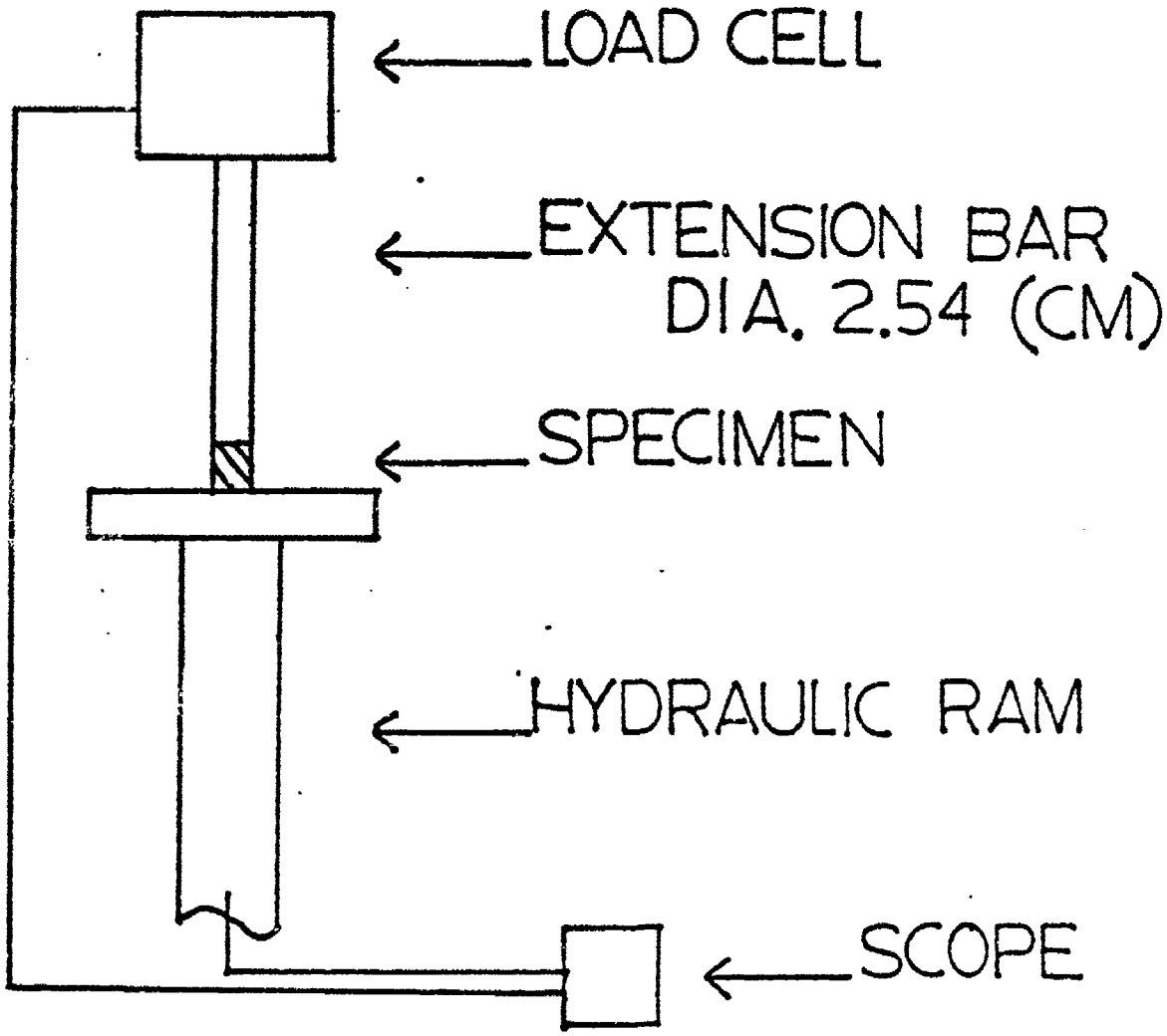
LOAD CELL
EXTENSION BAR
DIA. 2.54 (CM)
SPECIMEN
HYDRAULIC RAM
SCOPE

Fig. 8

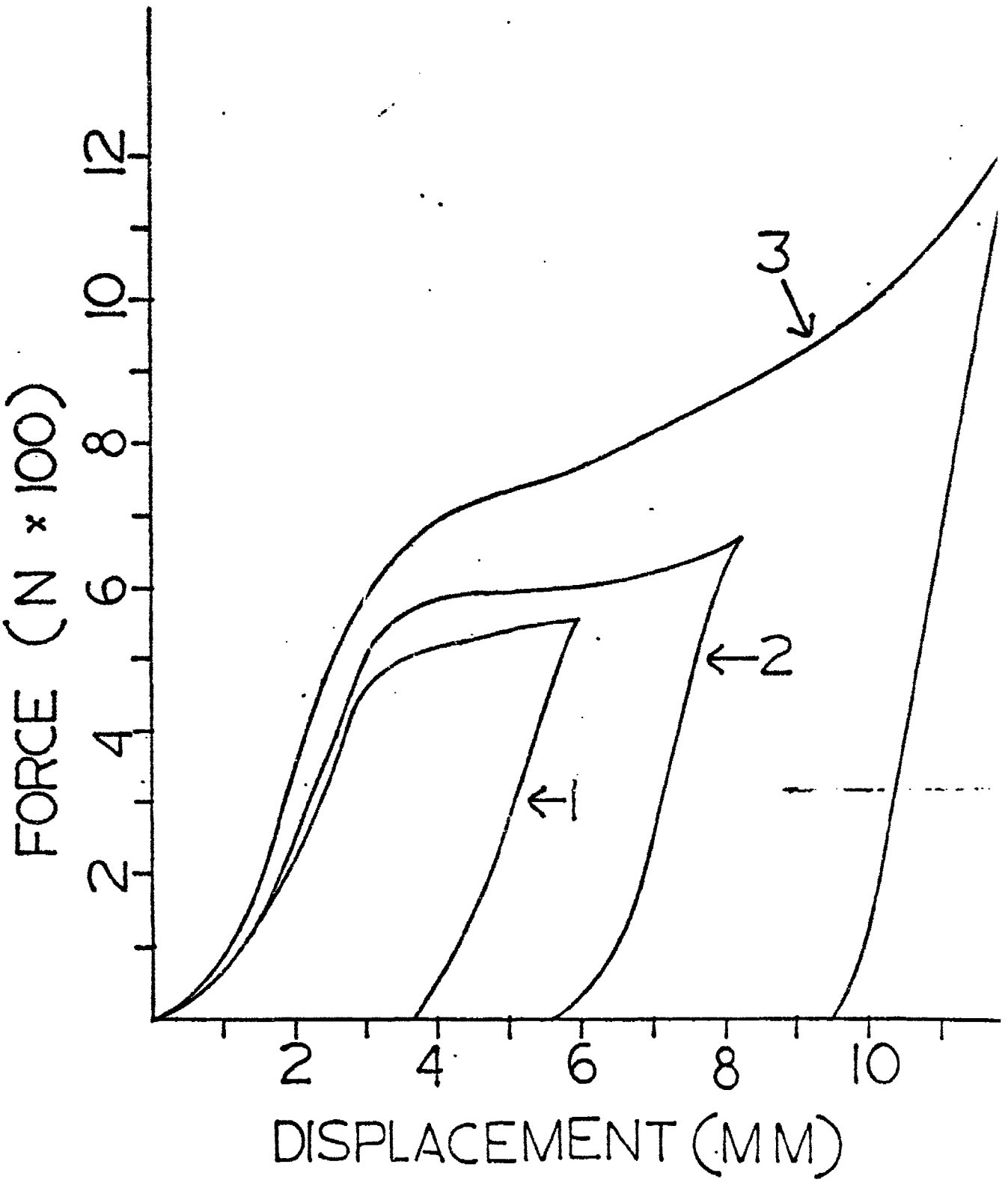

Fig. 9

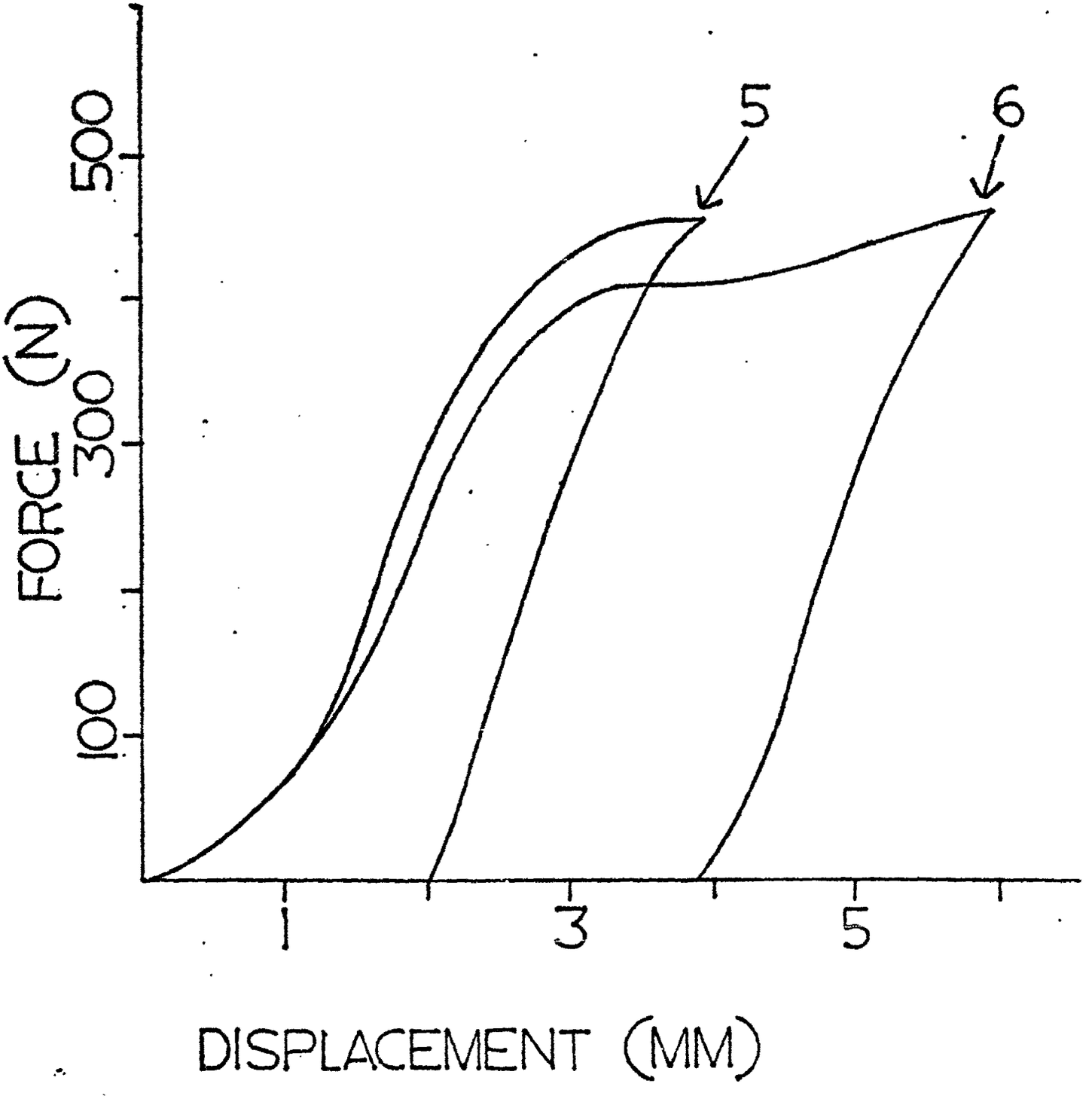

Fig. 10

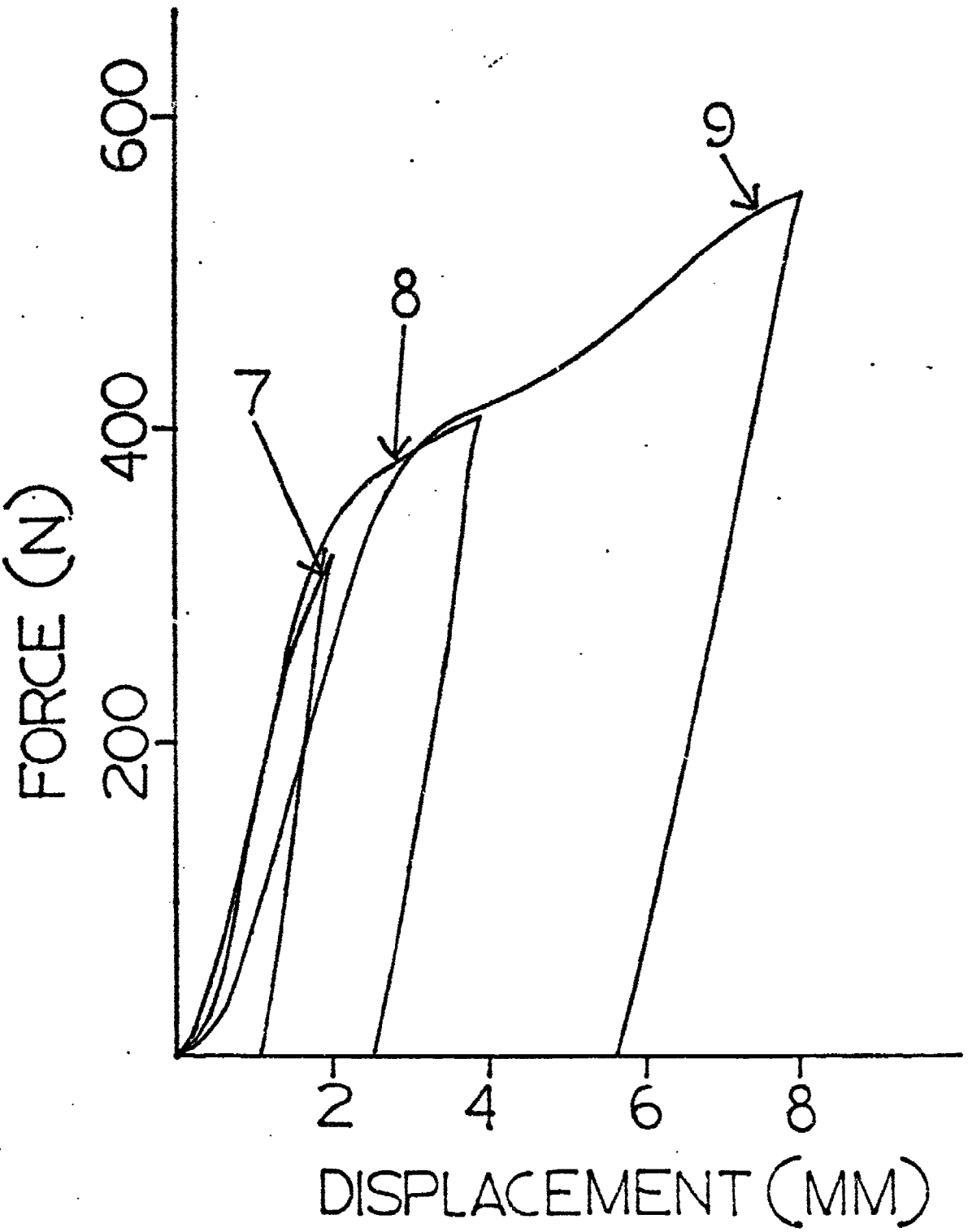

Fig. 11

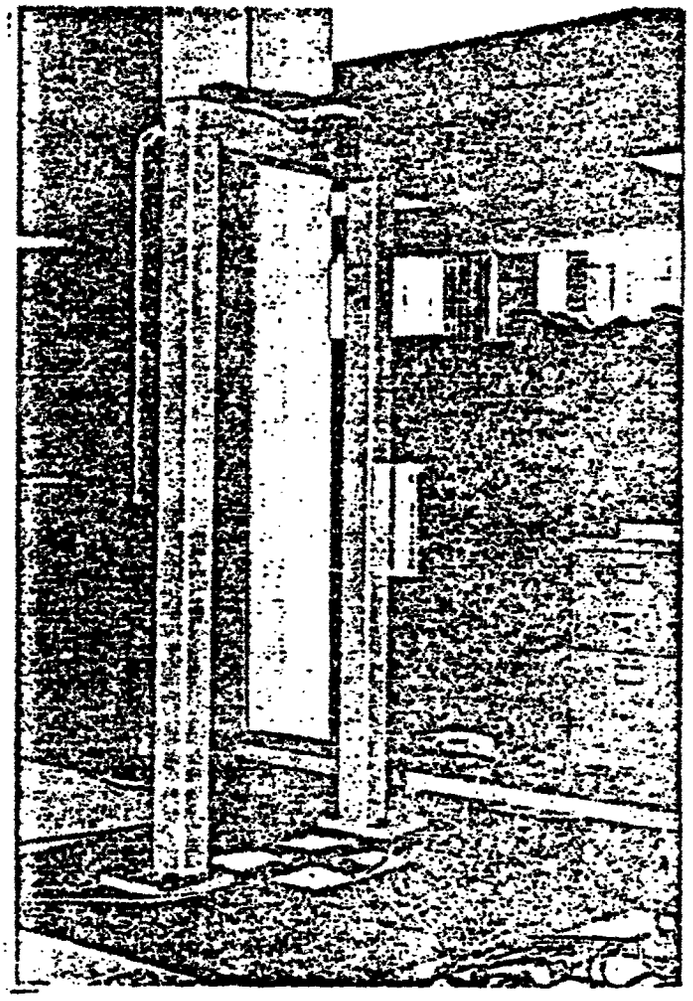

Figure 12. Helmet-Headform Drop Apparatus showing Electromagnet Above and Force Transducer Marked by a Cross at the Bottom of Picture

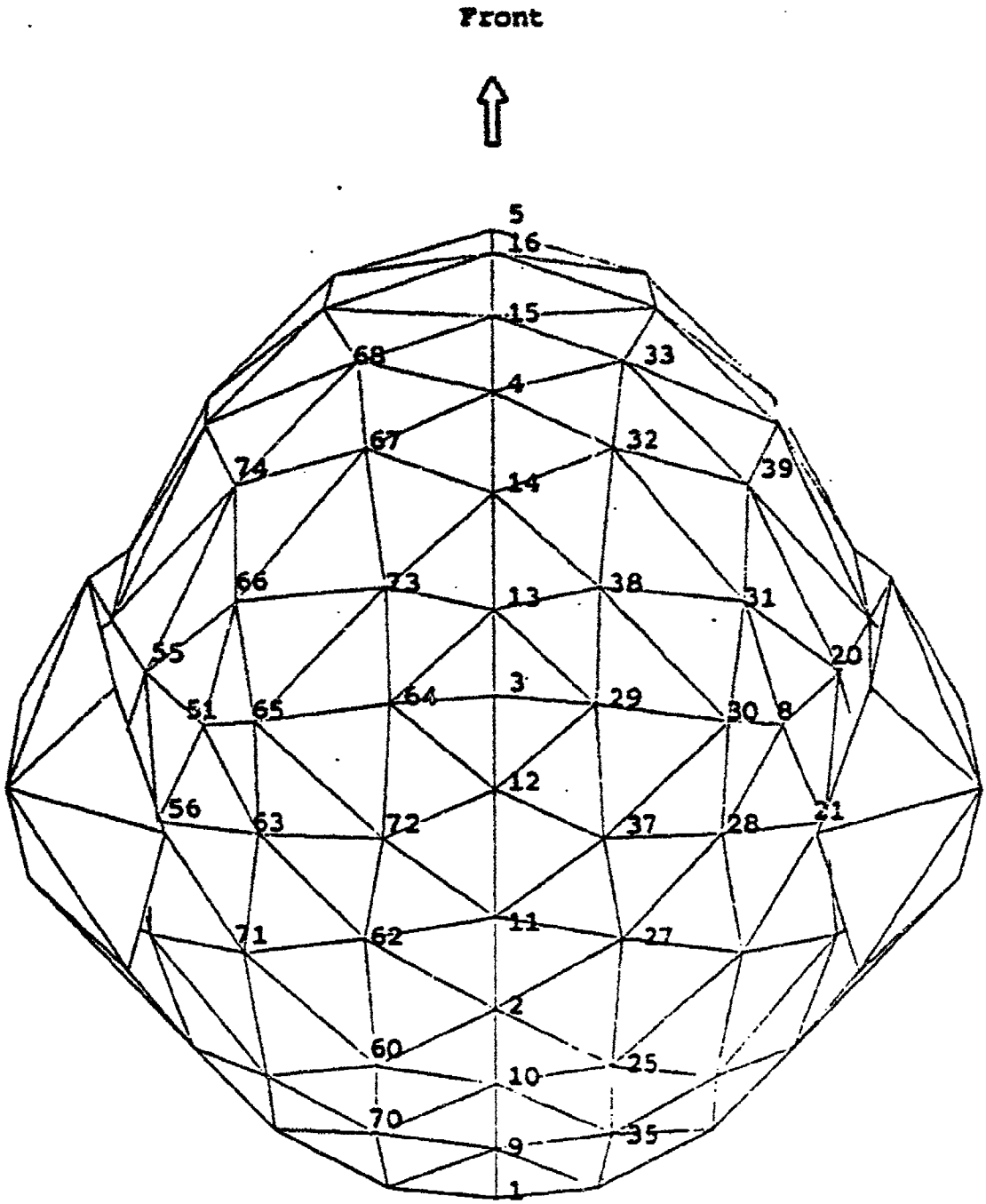

Figure 13. Node Numbers of Army Helmet

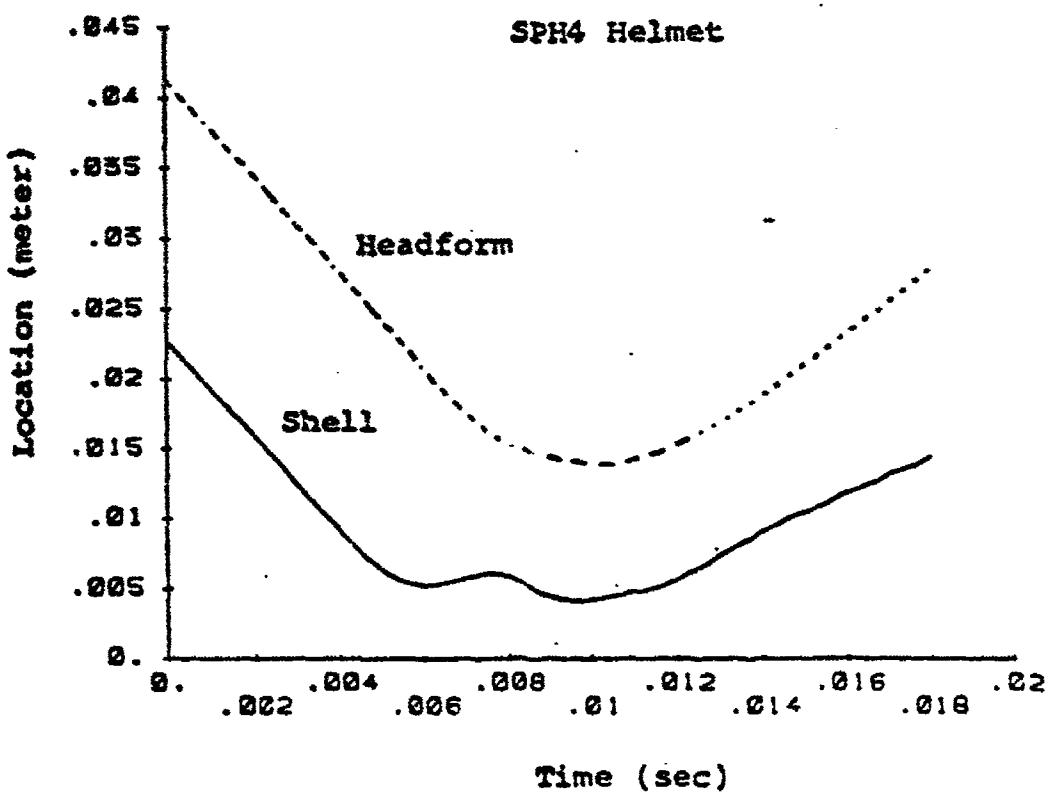

Fig. 14(a) Time History of the Position of Crowns of Shell and Headform for SPH4 Helmet

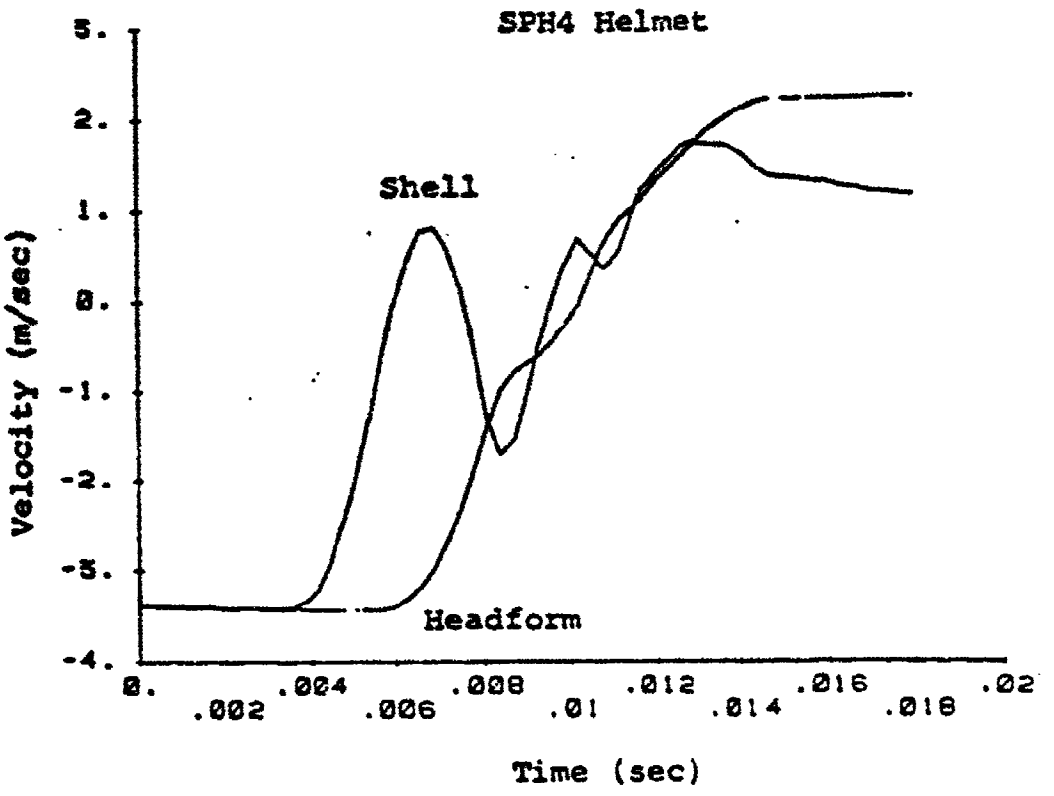

Fig. 14(b) Time History of the Velocity at the Crowns of Shell and Headform for SPH4

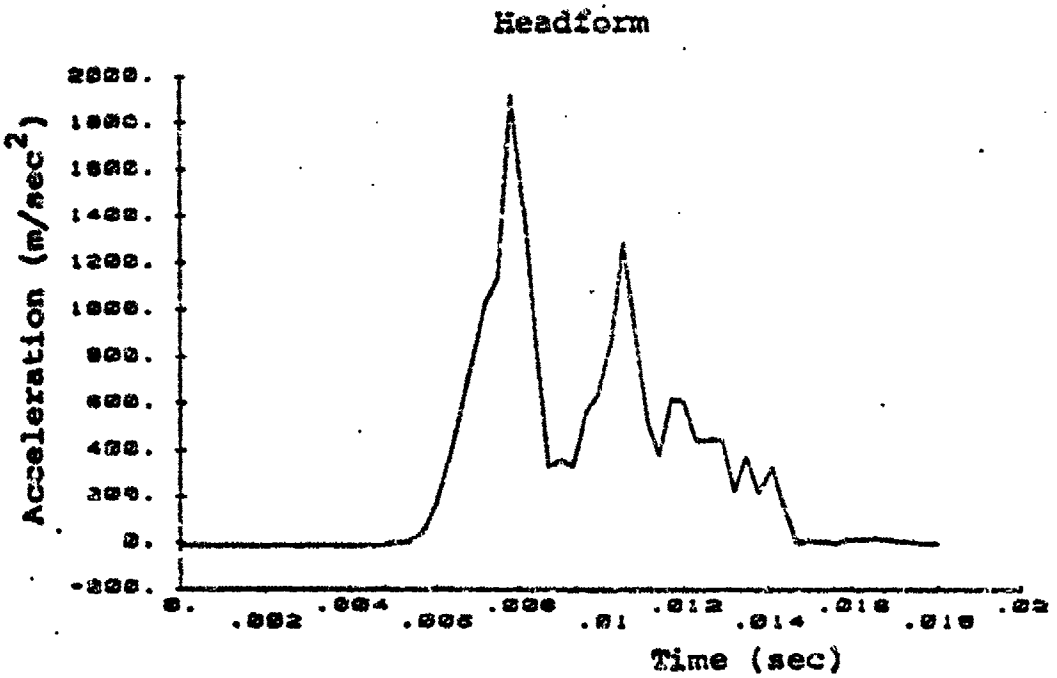

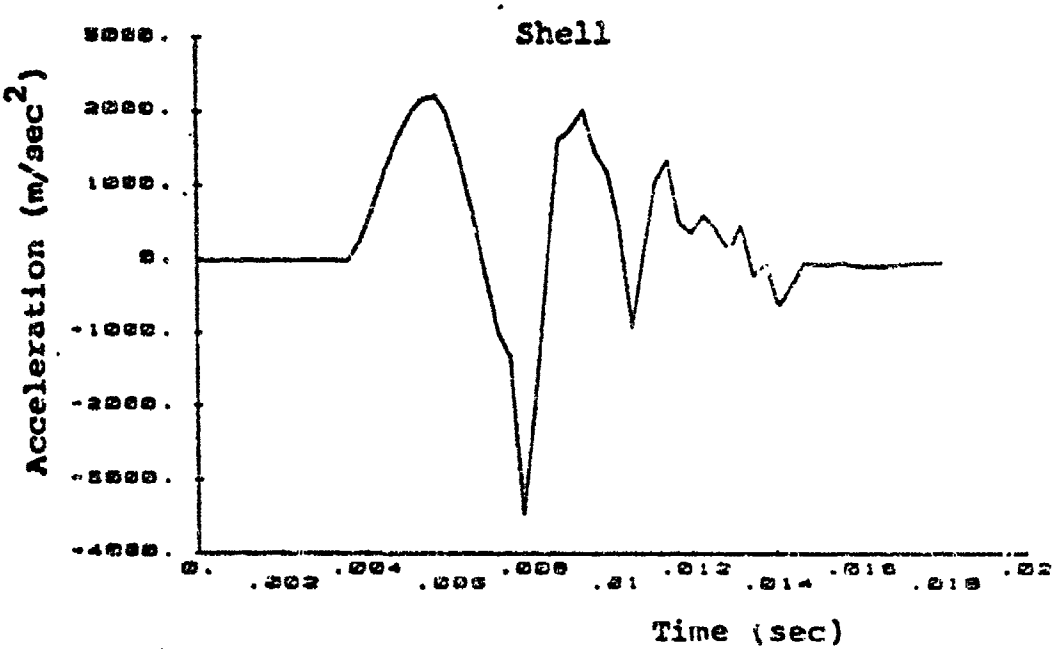

Fig. 14(c) Time History of the Acceleration of Shell and Headform at the Crowns for SPH4

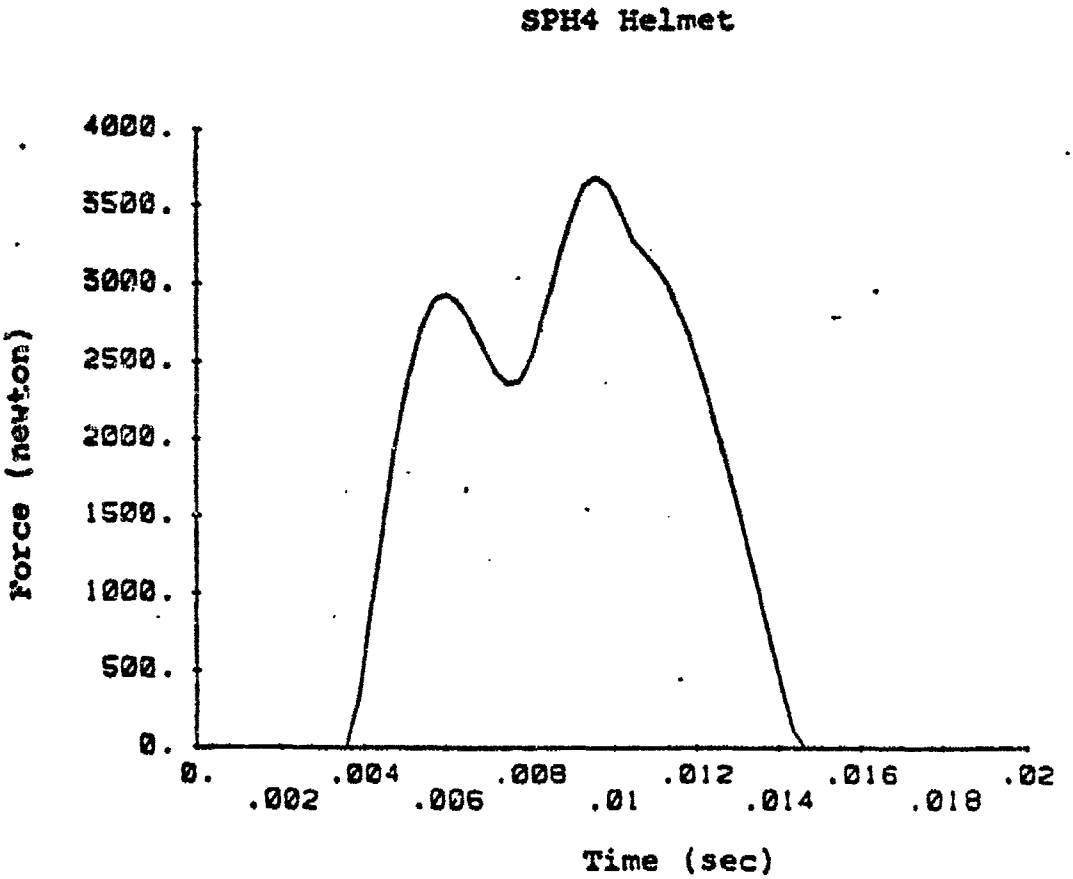

Fig. 14(d) Time History of Impact Force between Shell and Ground for SPH4 Helmet

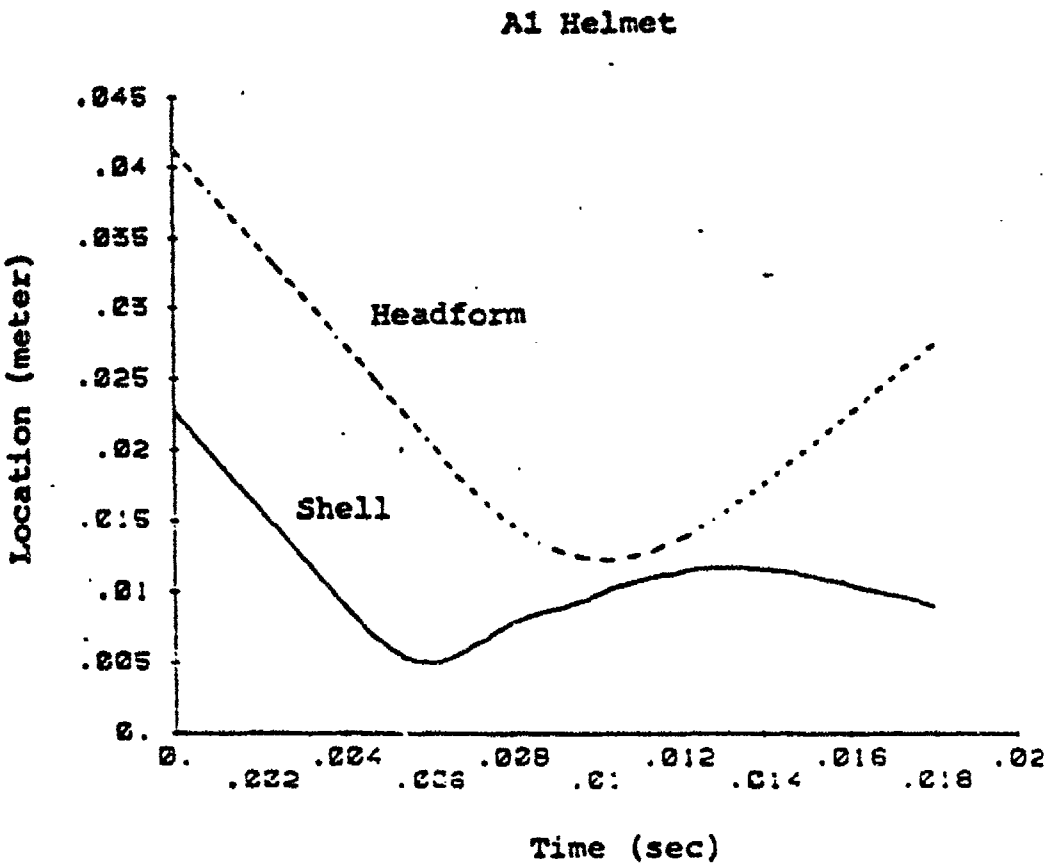

Fig. 15(a) Time History of the Position of Crowns of Shell and Headform for A1 Helmet

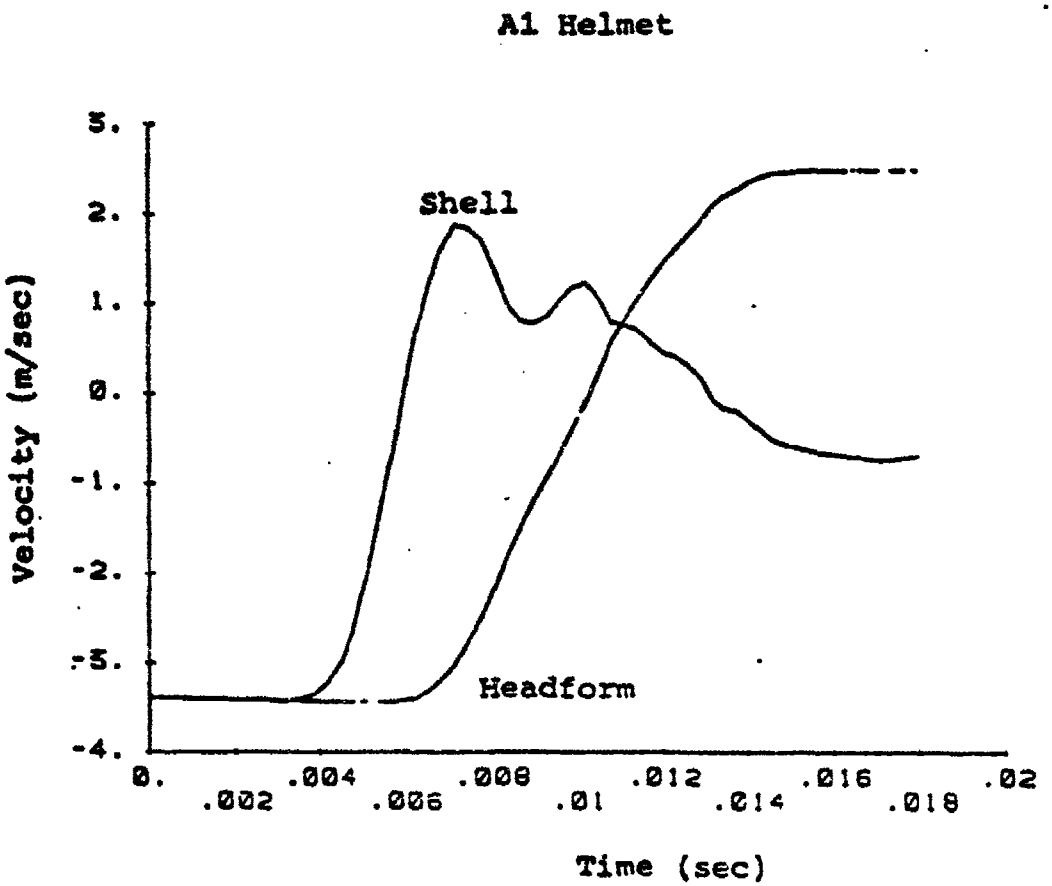

Fig. 15(b) Time History of the Velocity at the Crowns of Shell and Headform for SPH4

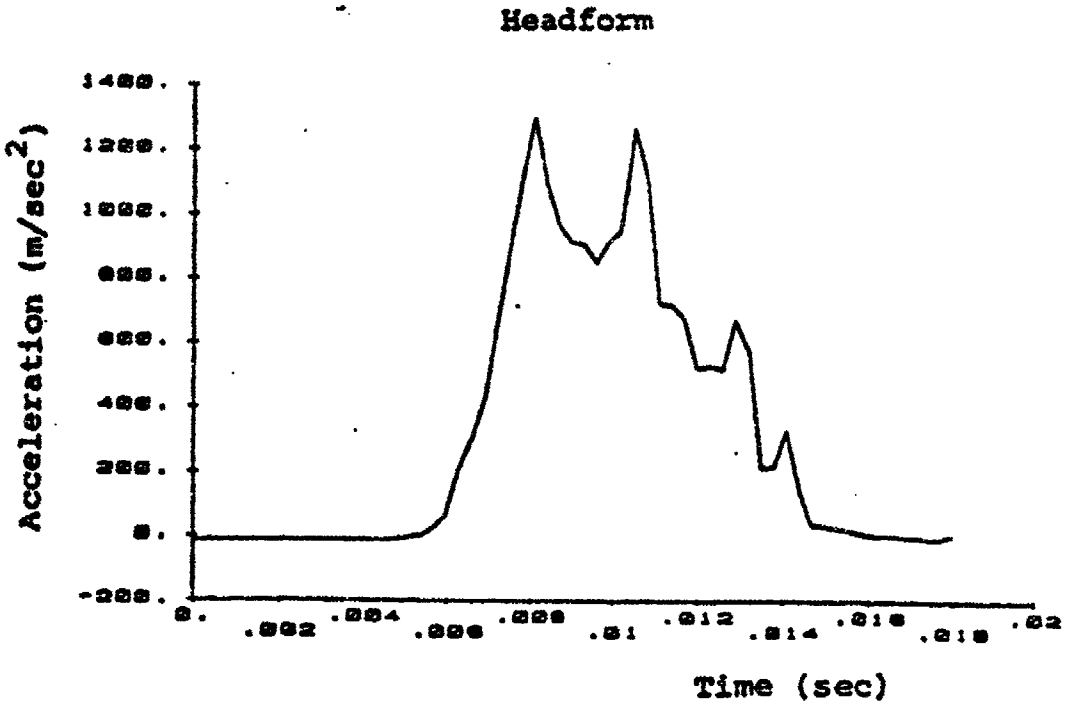

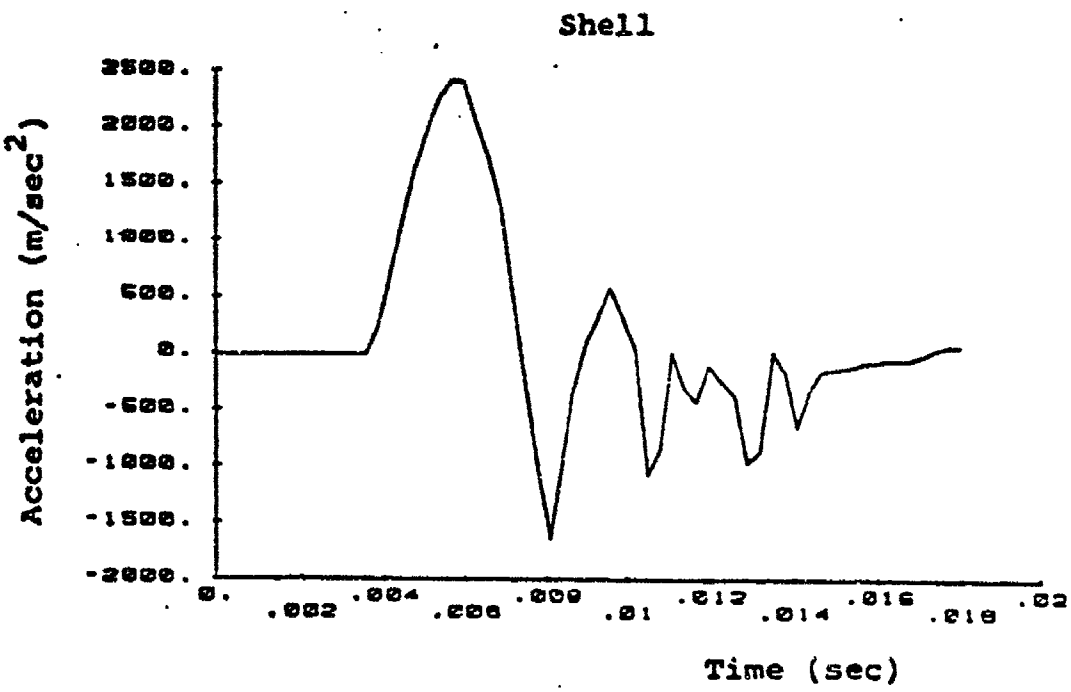

Fig. 15(c) Time History of the Acceleration of Shell and Headform at the Crowns for A1

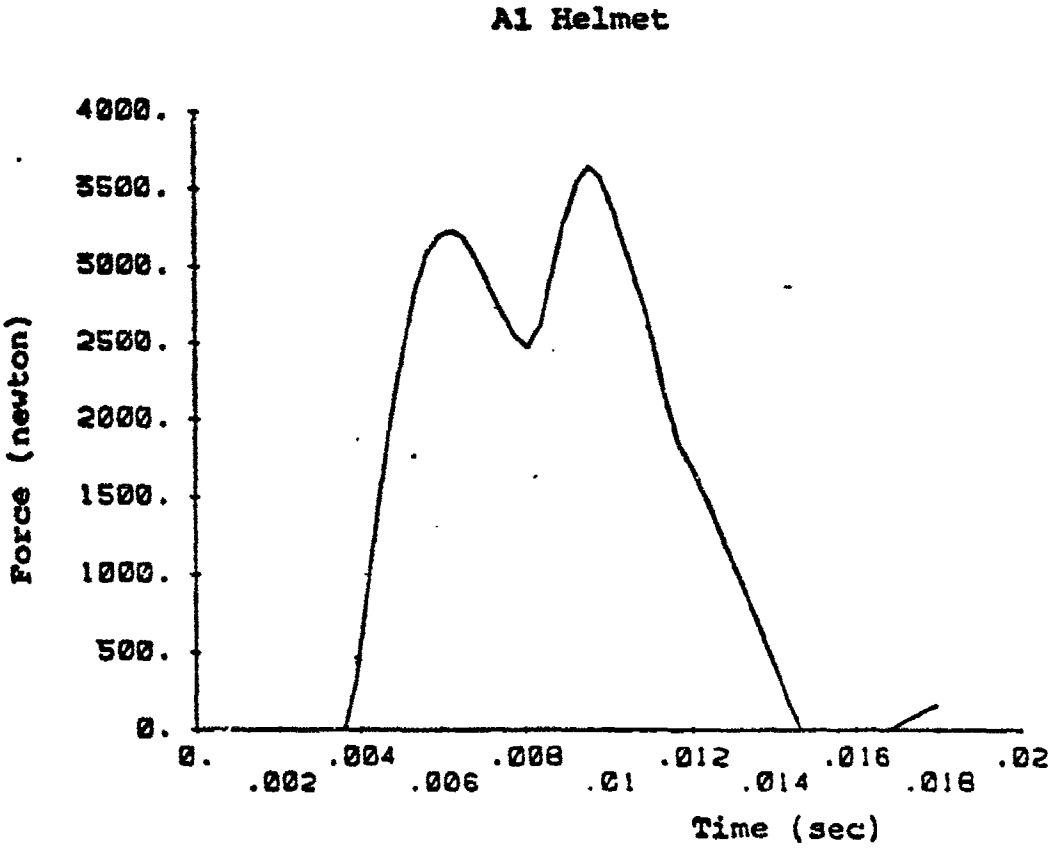

Fig. 15(d) Time History of Impact Force between Shell and Ground for Al Helmet

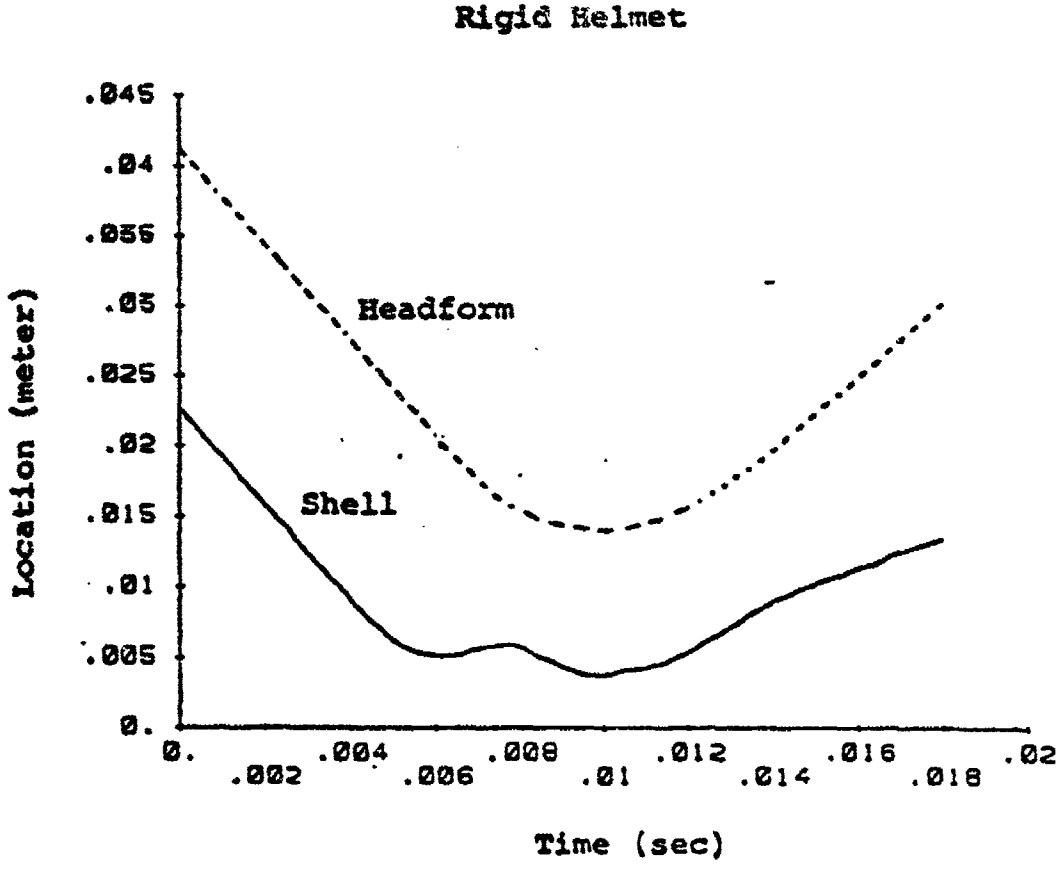

Fig. 16(a) Time History of the Position of Crowns of Shell and Headform for Rigid Helmet

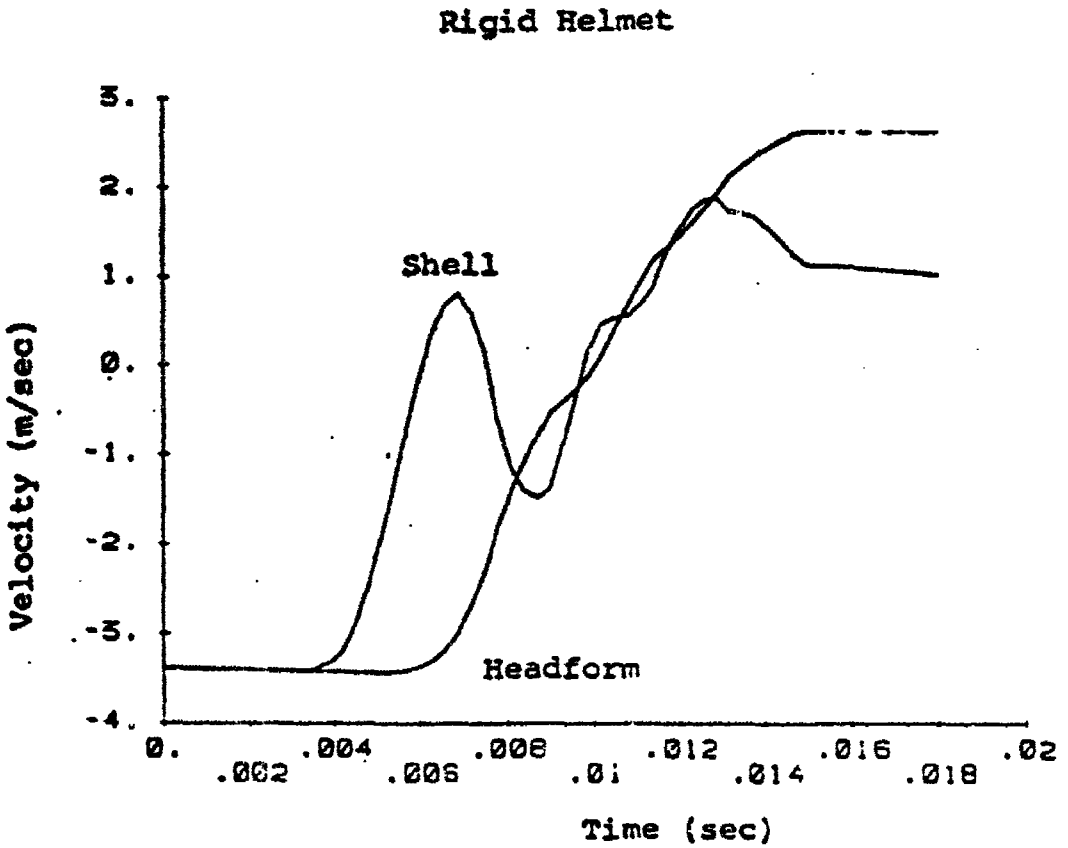

Fig. 16(b) Time History of the Velocity at the Crowns of Shell and Headform for Rigid Helmet

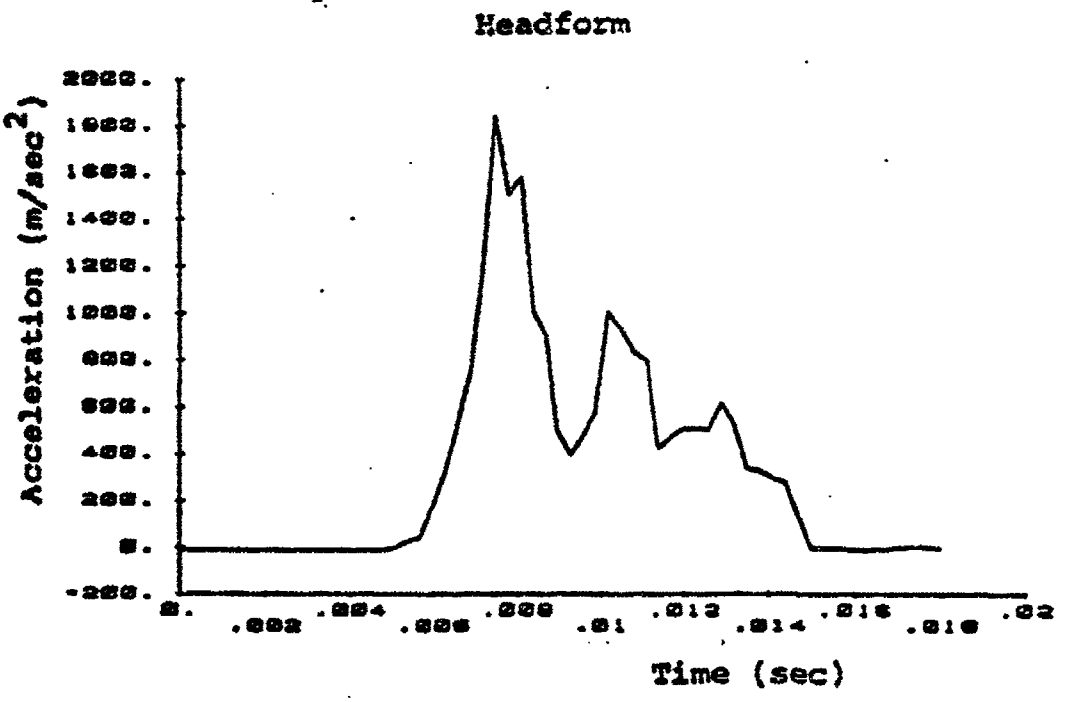

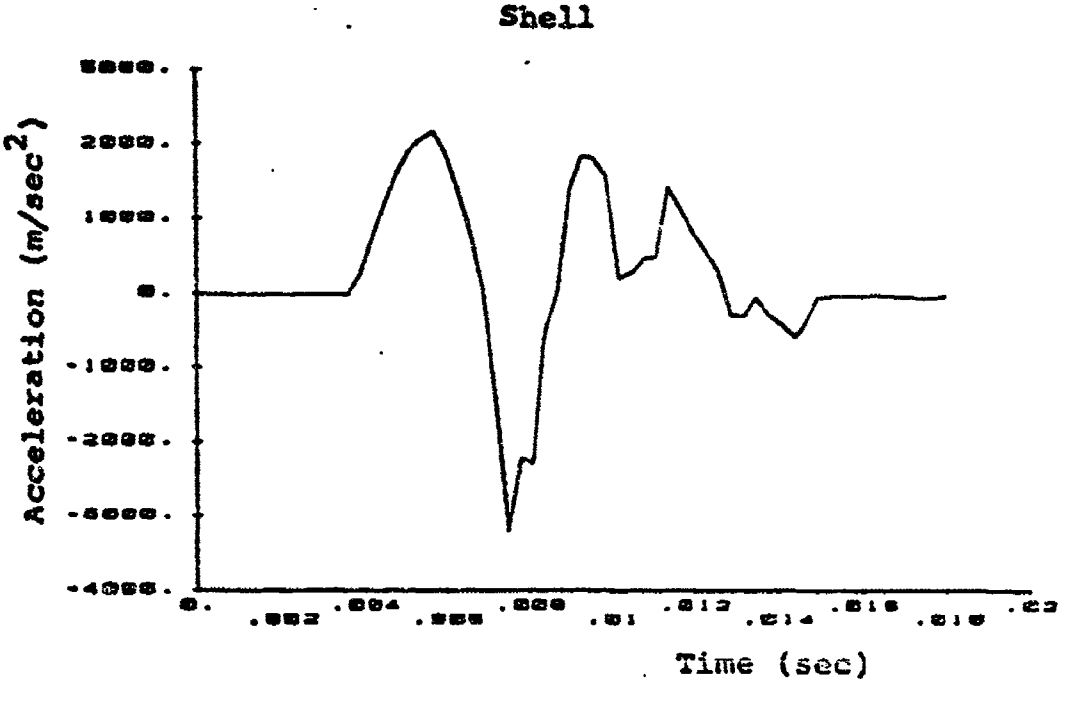

Fig. 16(c) Time History of the Acceleration of Shell and Headform at the Crowns for Rigid

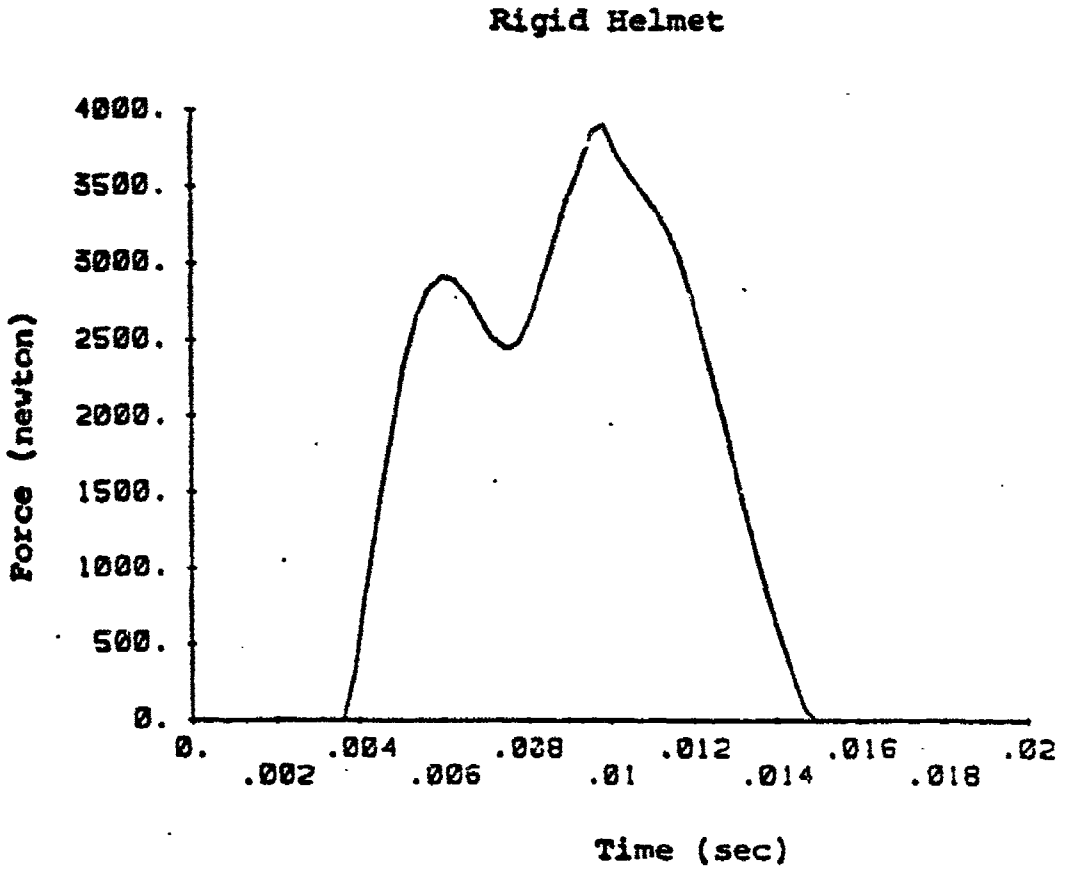

Fig. 16(d) Time History of Impact Force between Shell and Ground for Rigid Helmet

Fig. 17 Experimental Results of Force and Acceleration for SPH4

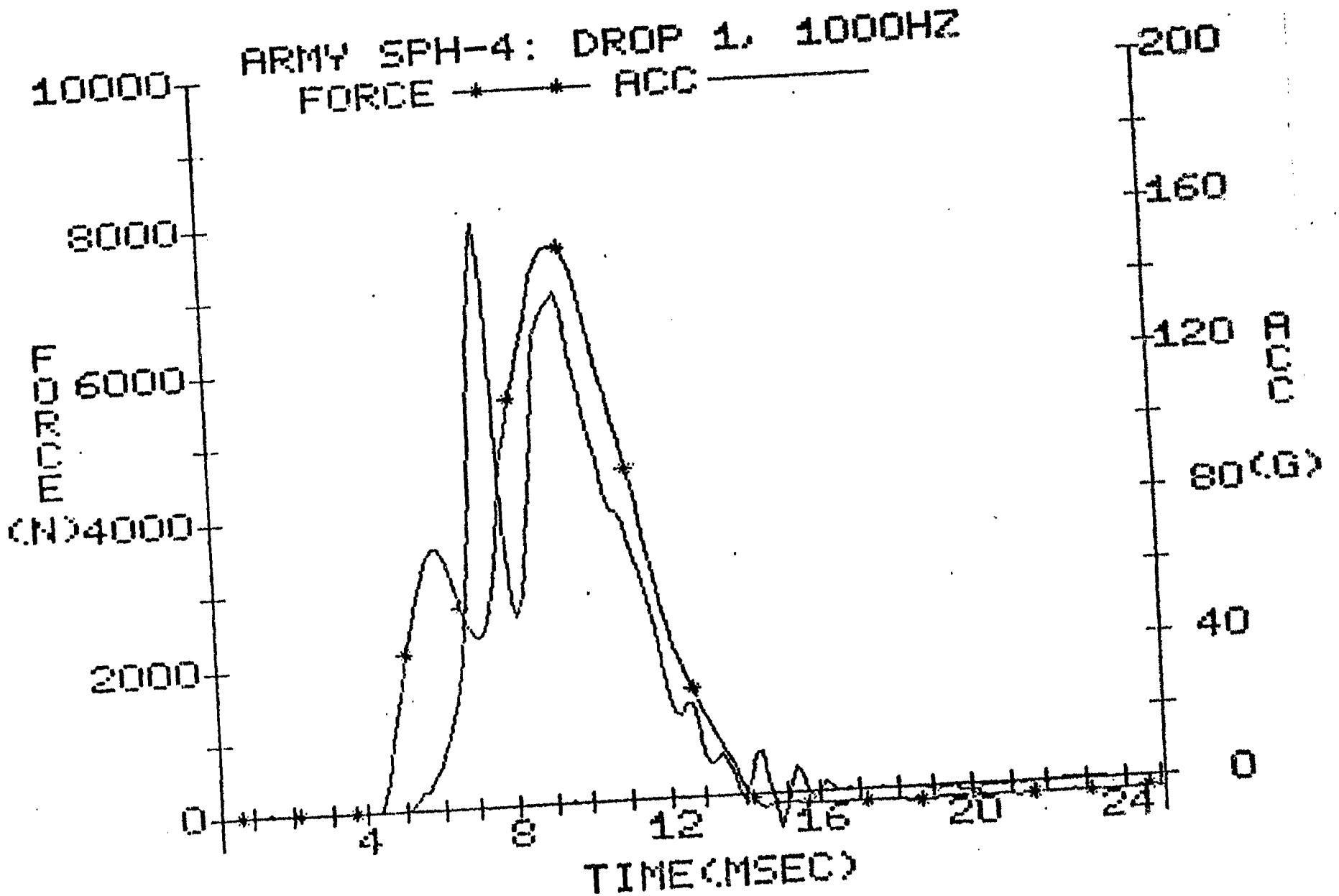

Fig. 18 Experimental Results of Force and Acceleration for A1

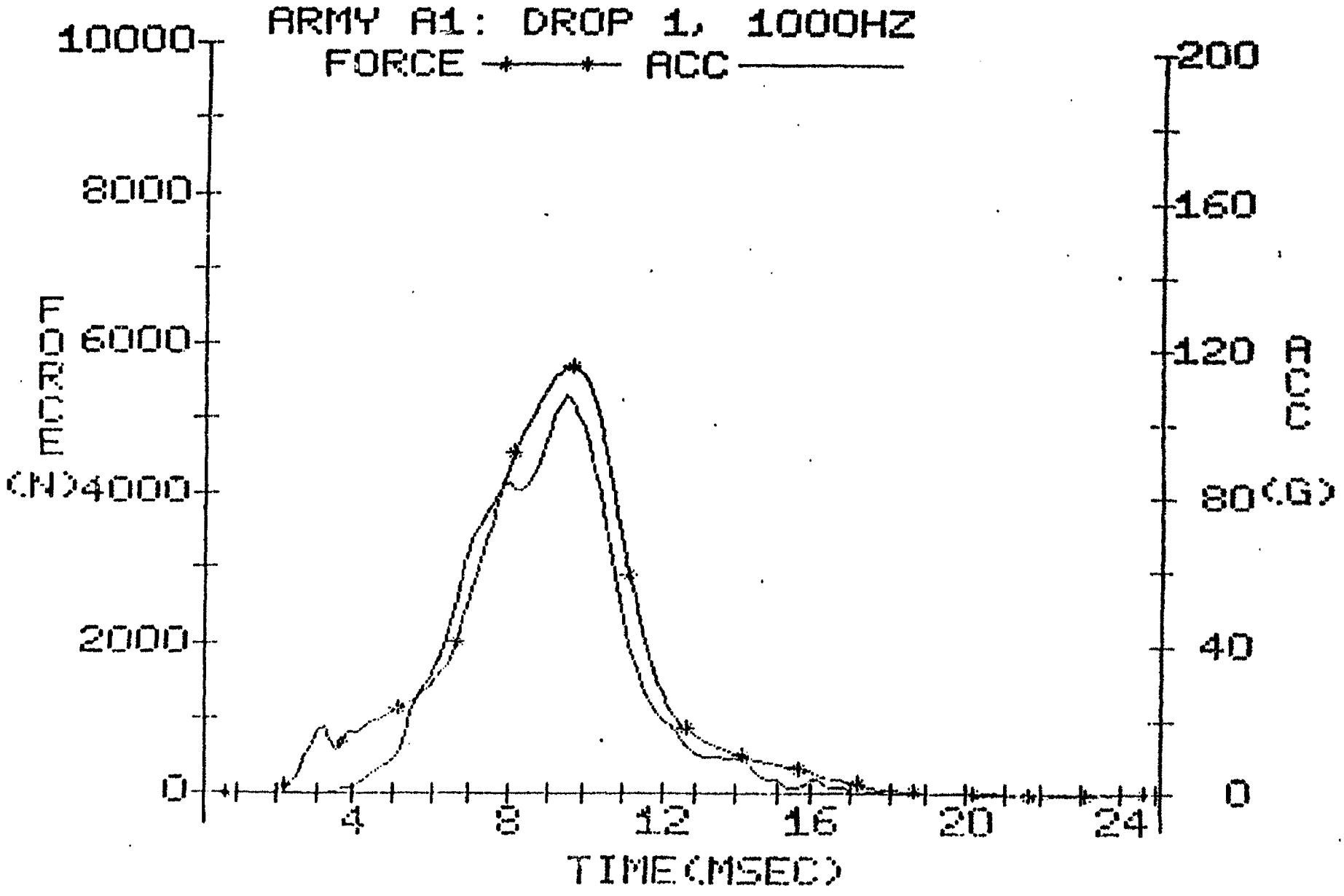

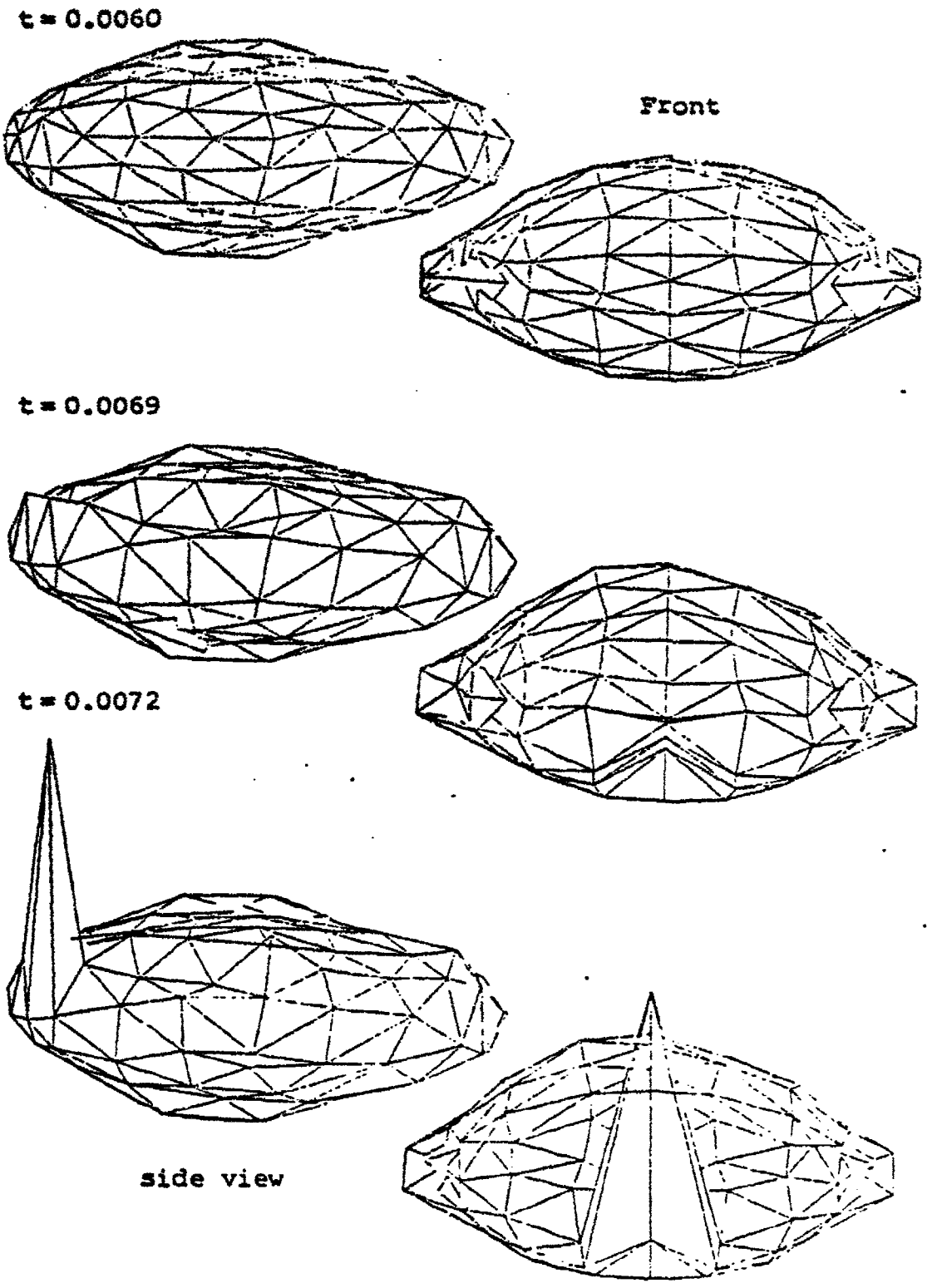

Fig. 19 (a) Pressure Disribution of SPII4

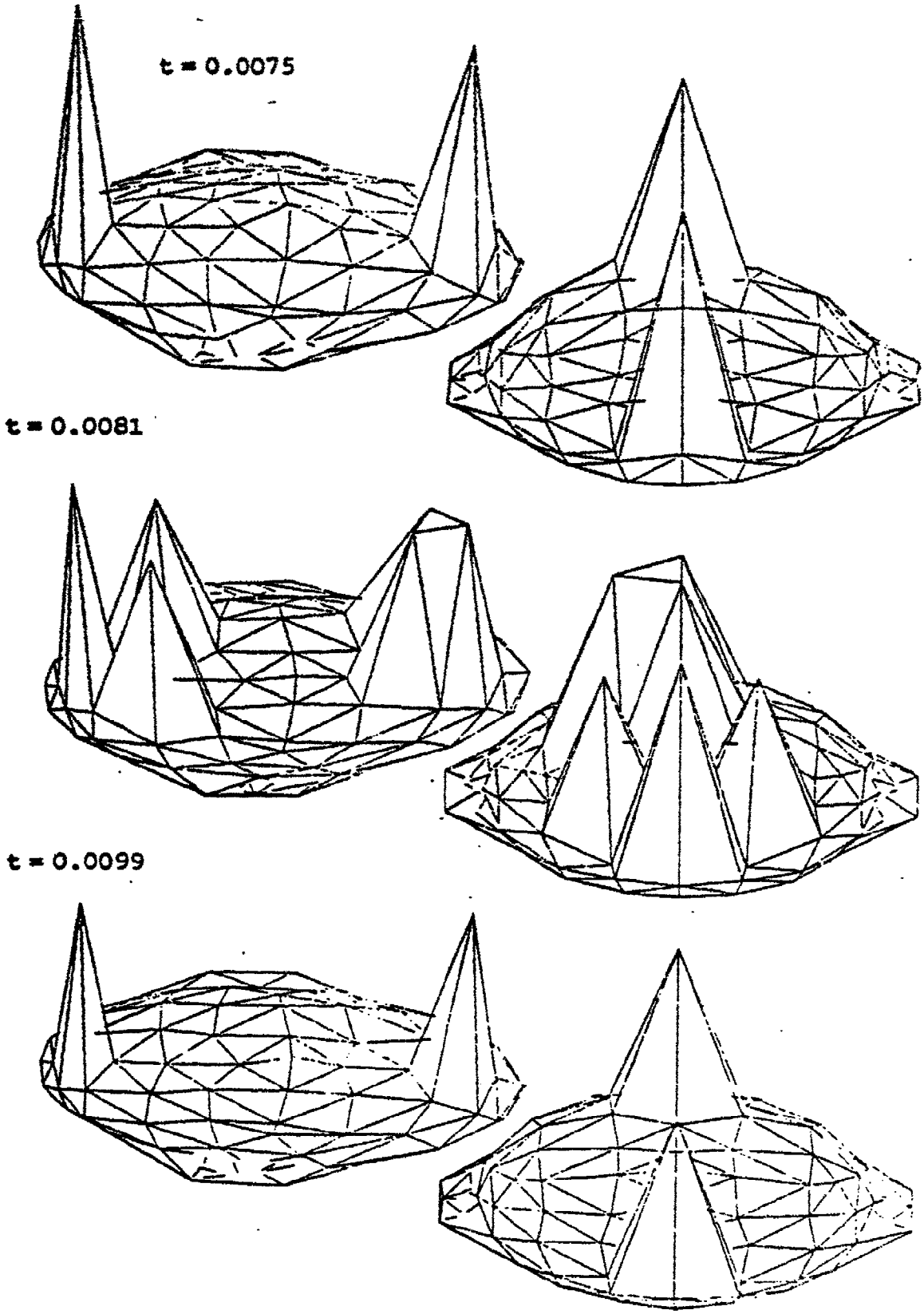

Fig. 19 (b) Pressure Distribution of SPH4

t = 0.0120

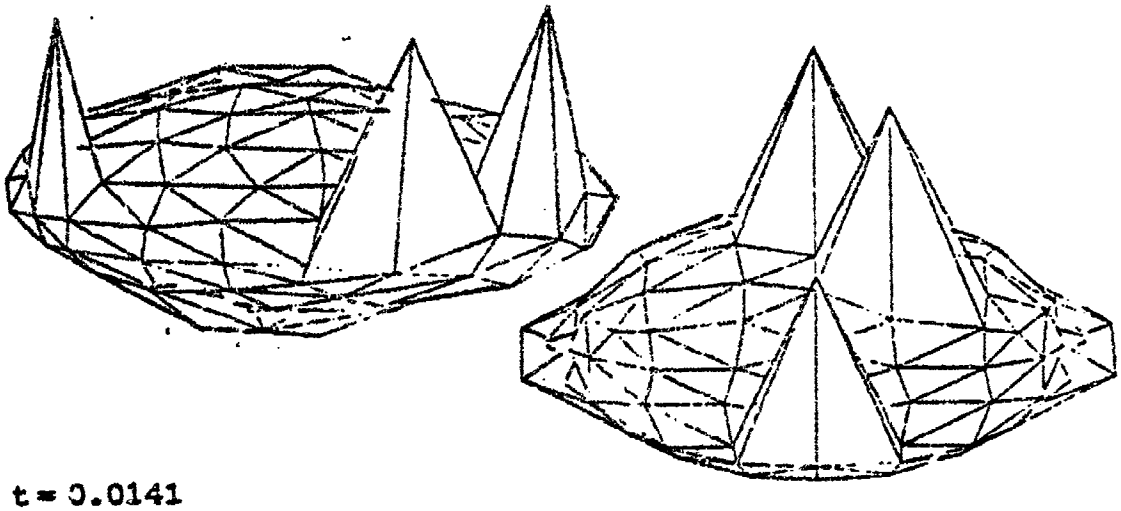

t = 0.0141

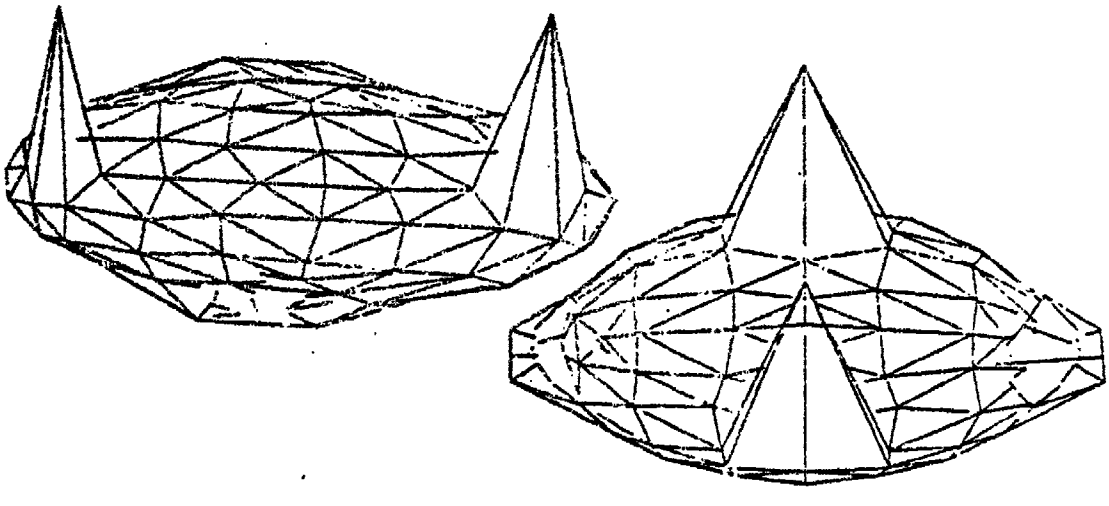

t = 0.0159

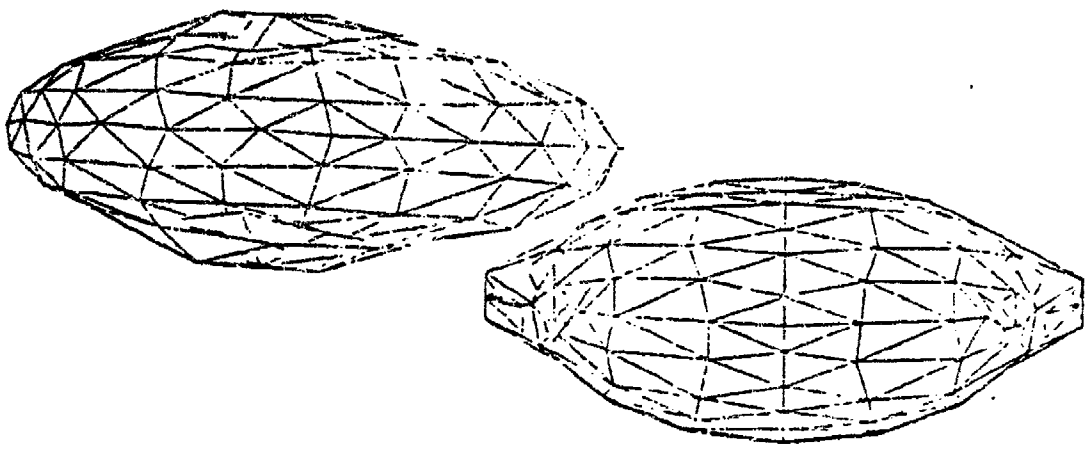

Fig. 19 (c) Pressure Distribution of SPH4

t = 0.0060

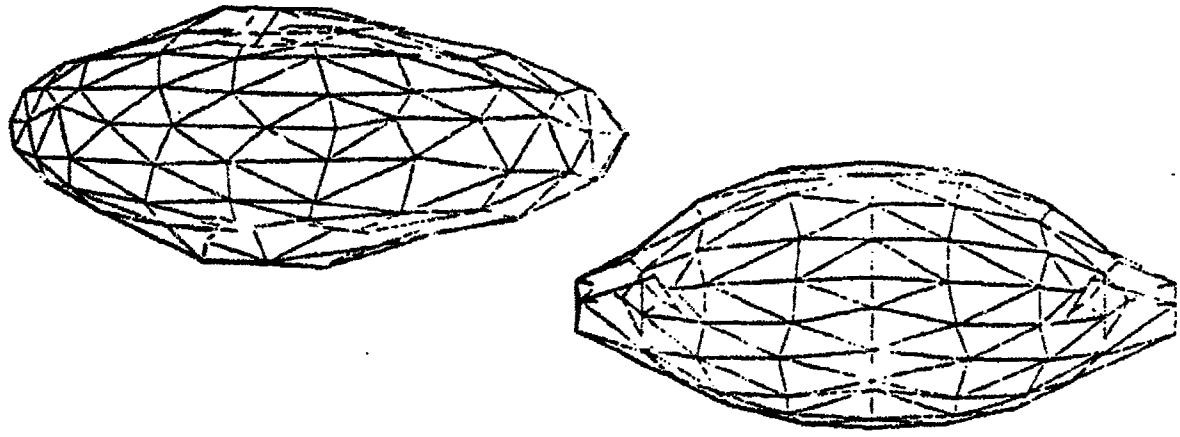

t = 0.0069

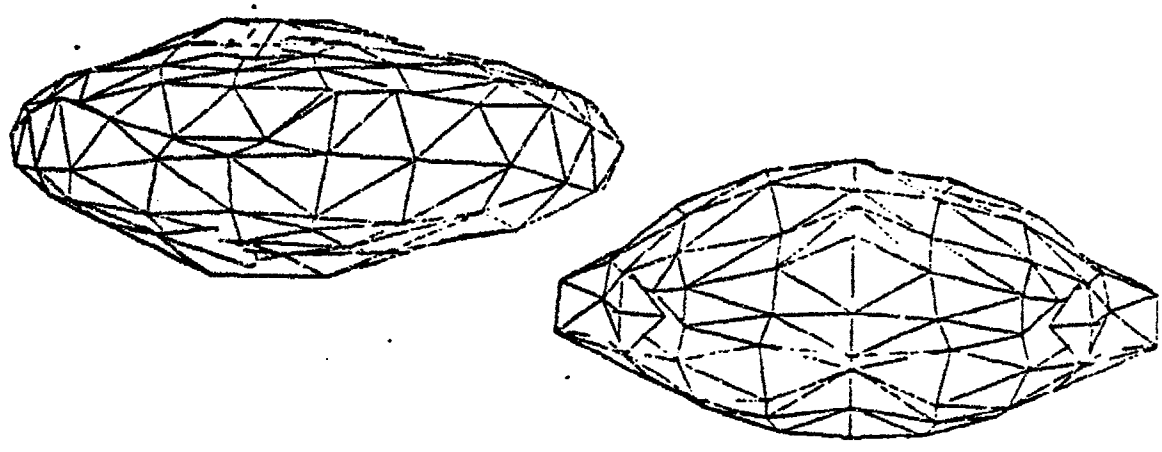

t = 0.0072

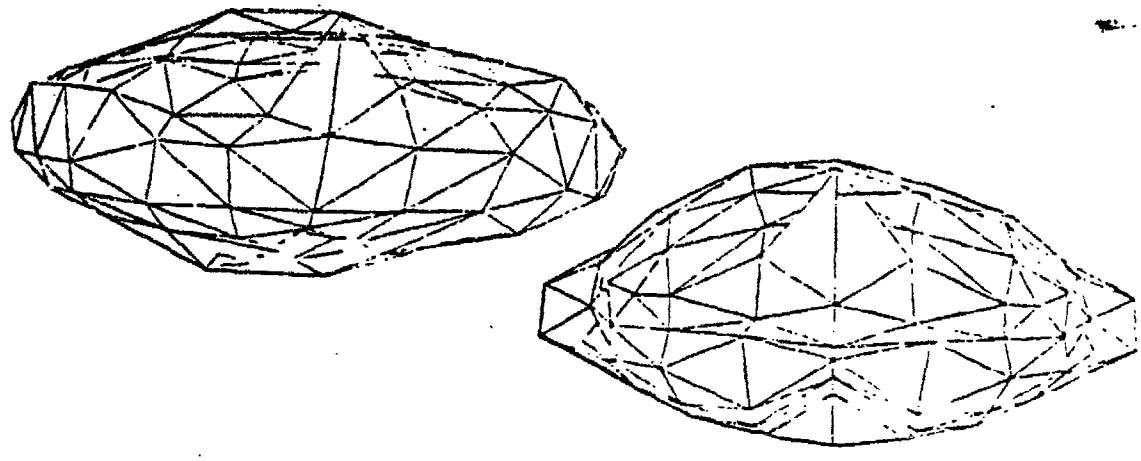

Fig. 20 (a) Pressure Distribution of A1

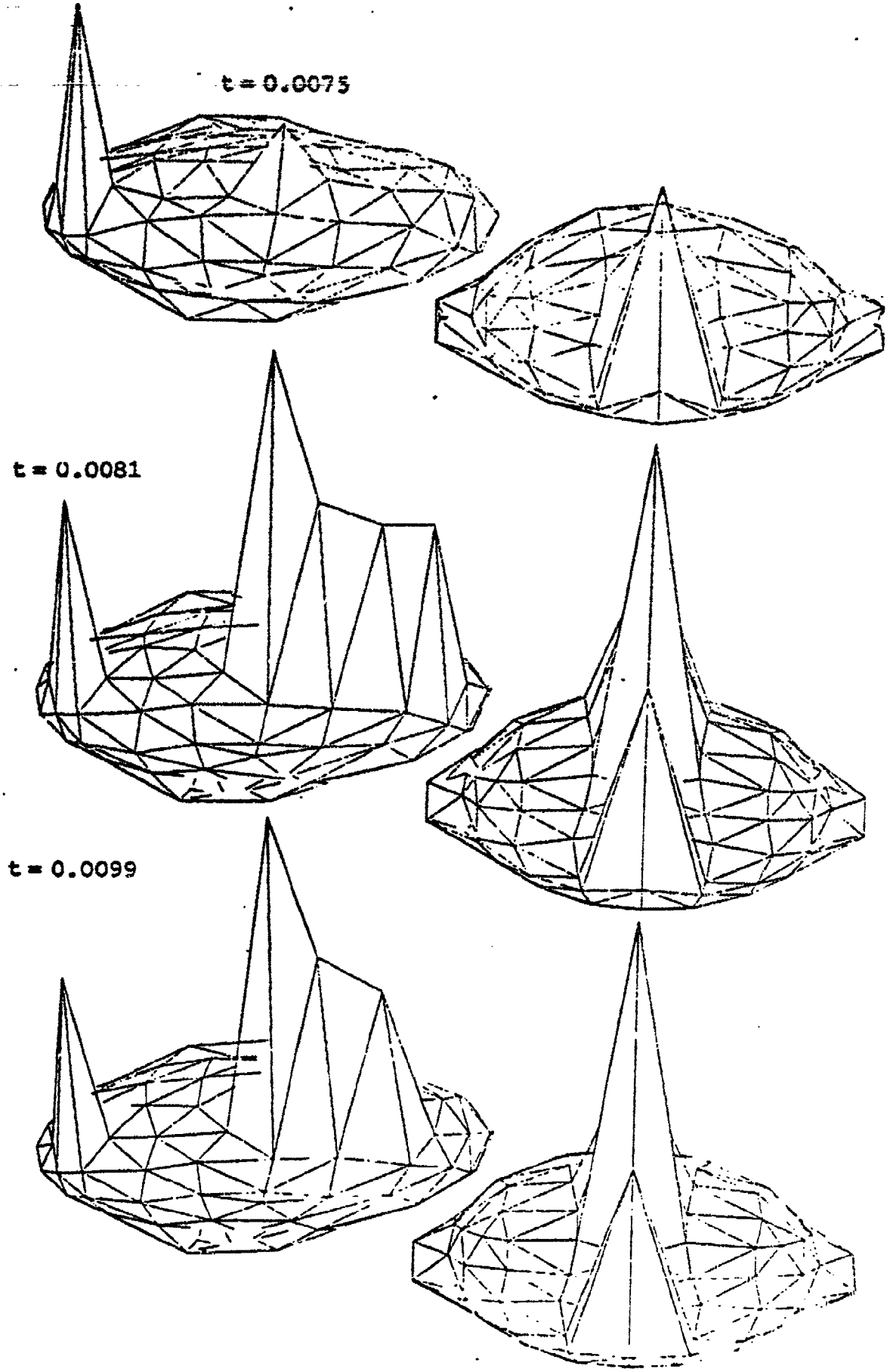

Fig. 20 (b) Pressure Distribution of A1

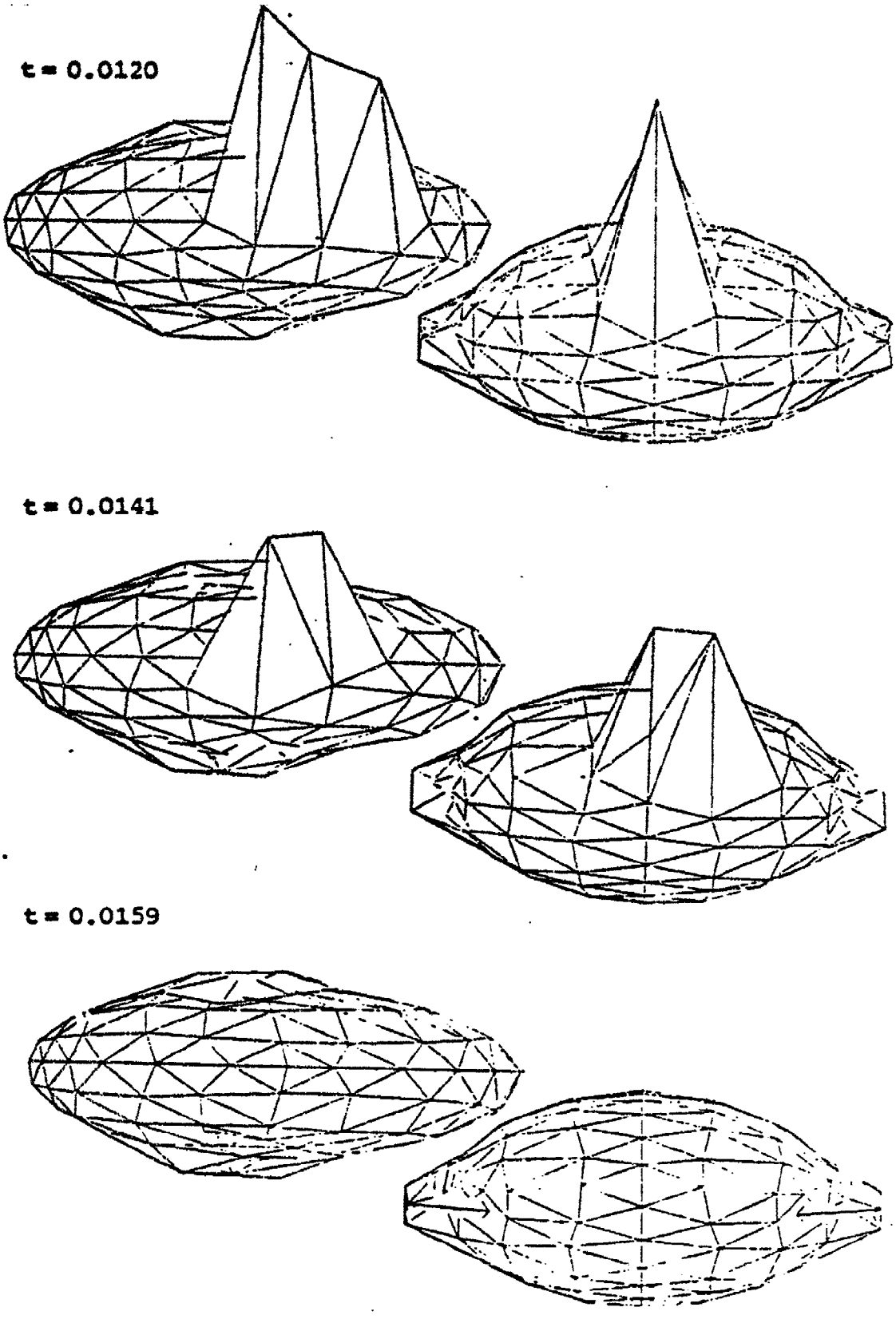

Fig. 20 (c) Pressure Disribution of A1

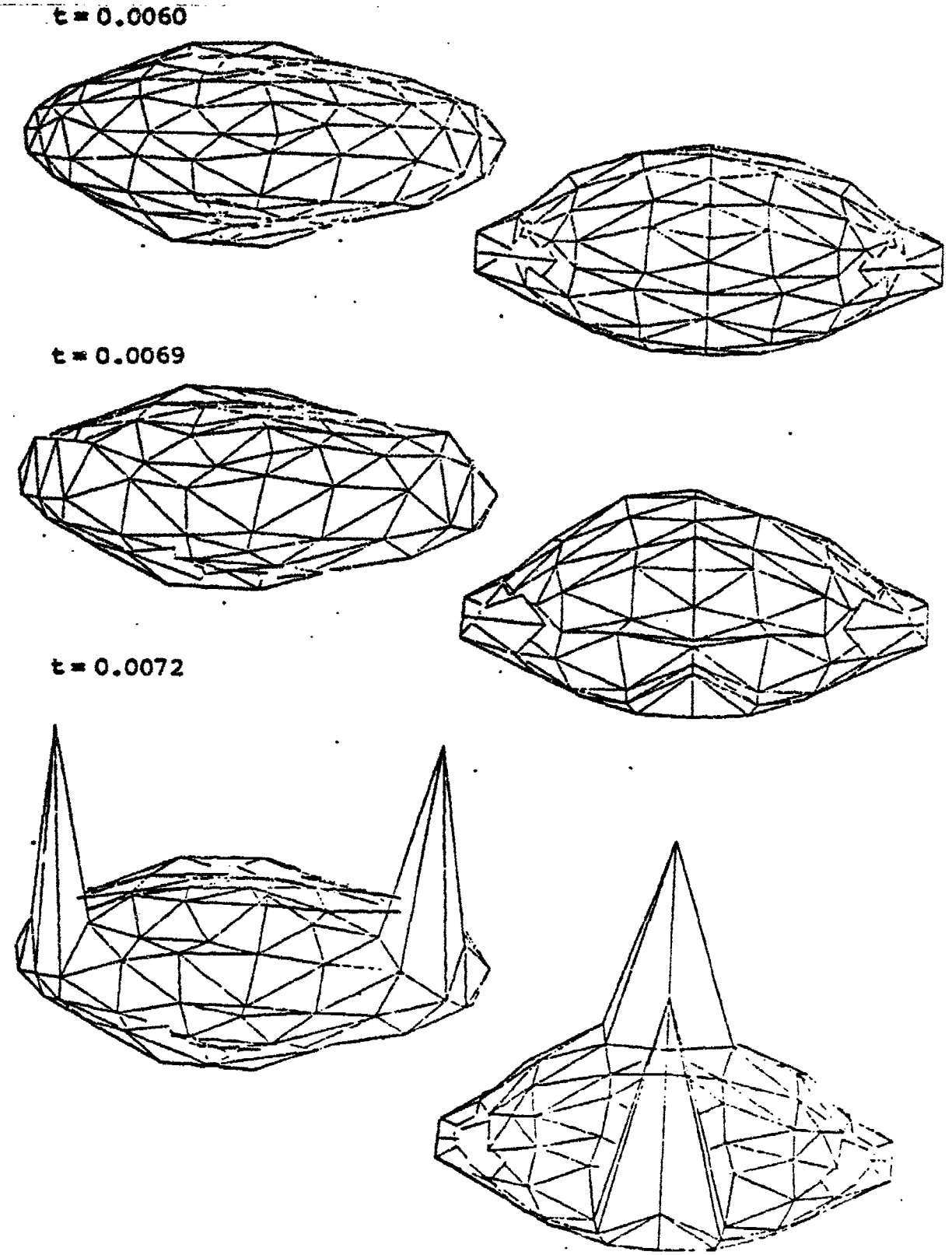

Fig. 21 (a) Pressure Disribution of Rigid

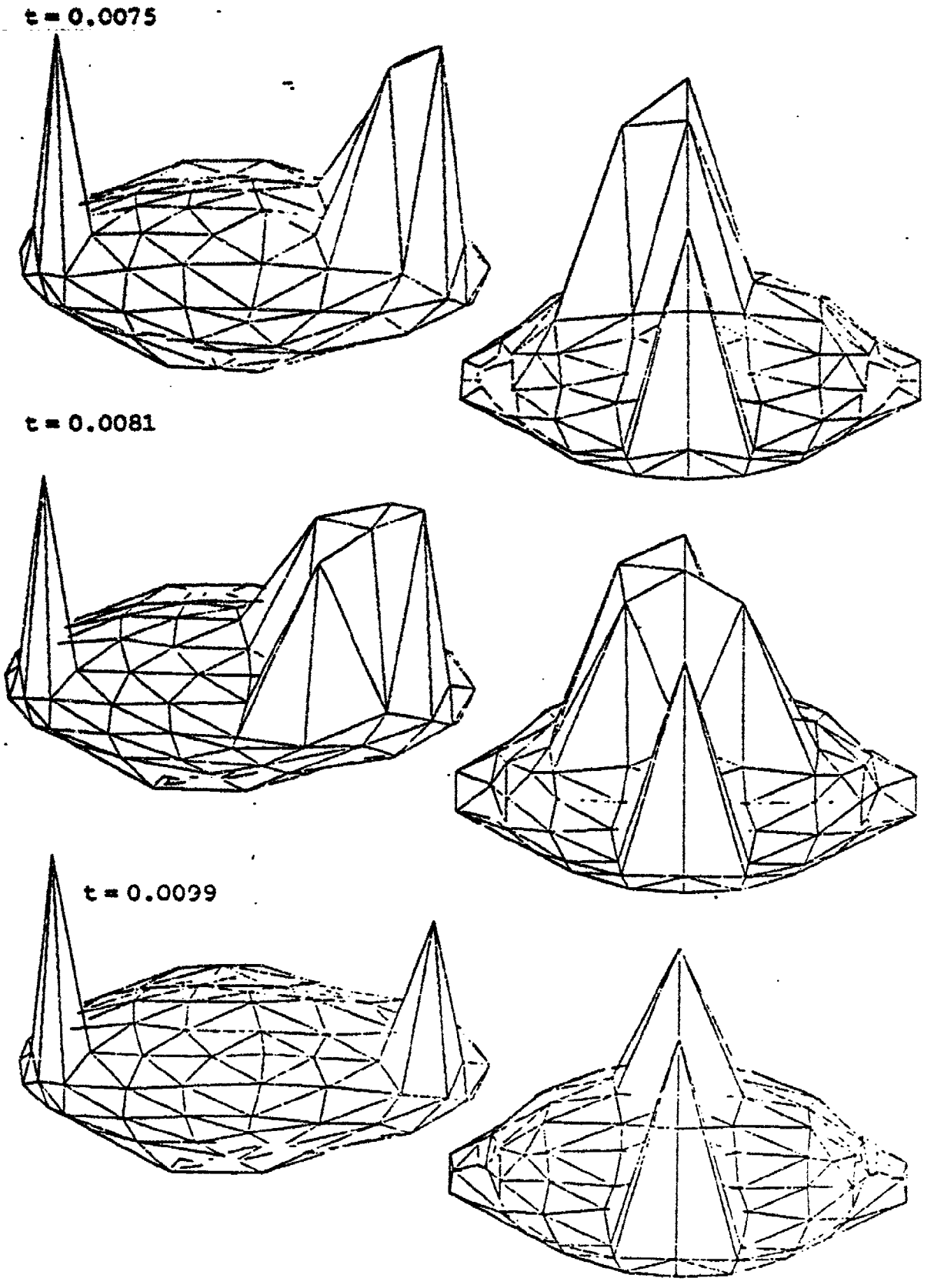

Fig. 21 (b) Pressure Distribution of Rigid

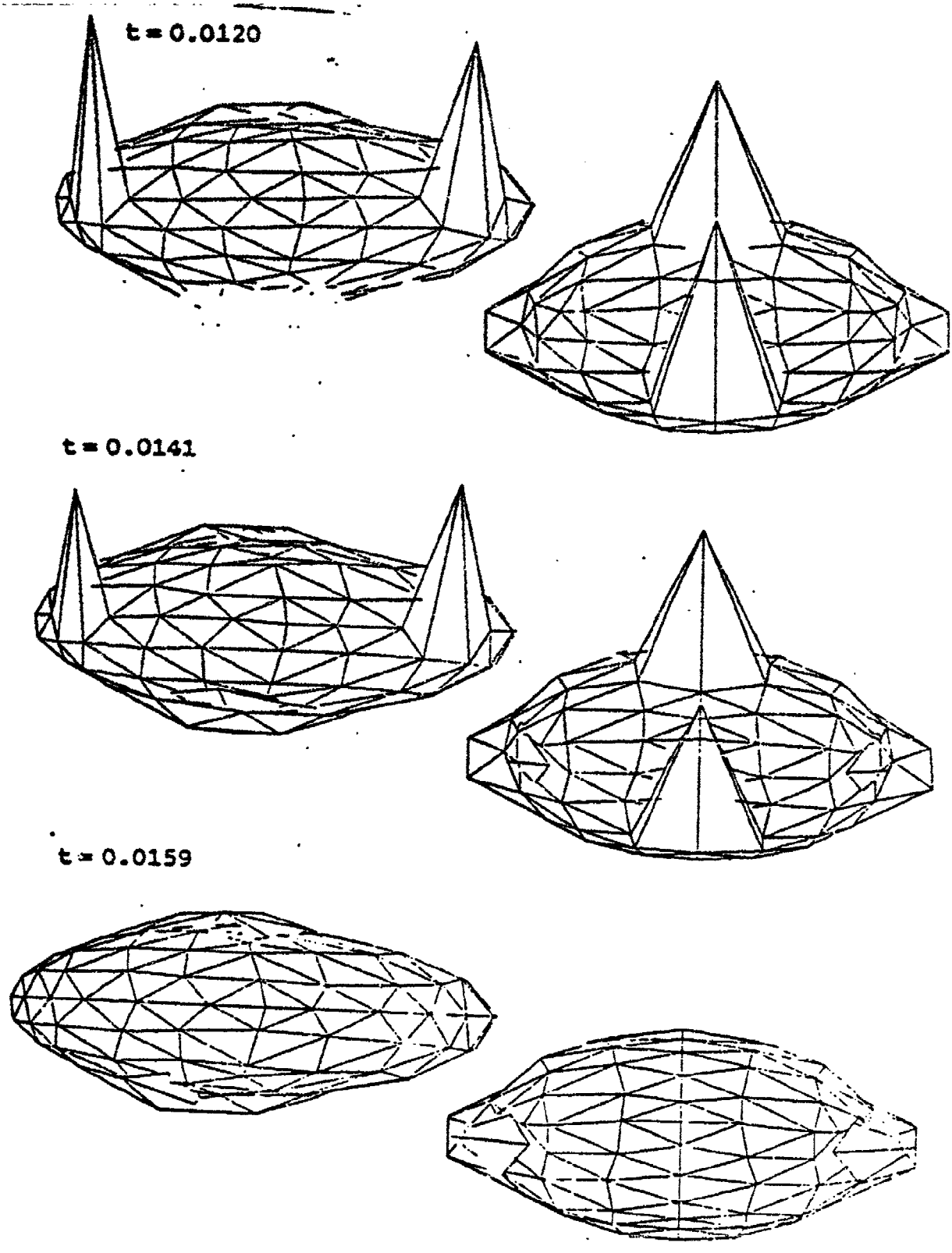

Fig. 21 (c) Pressure Distribution of Rigid

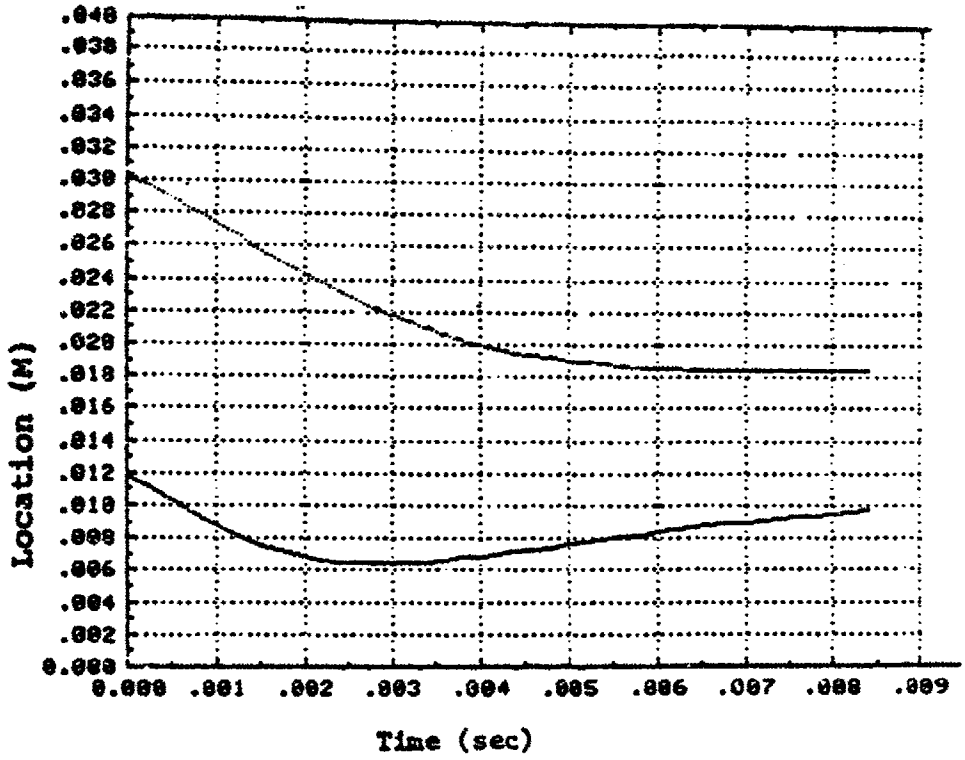

A

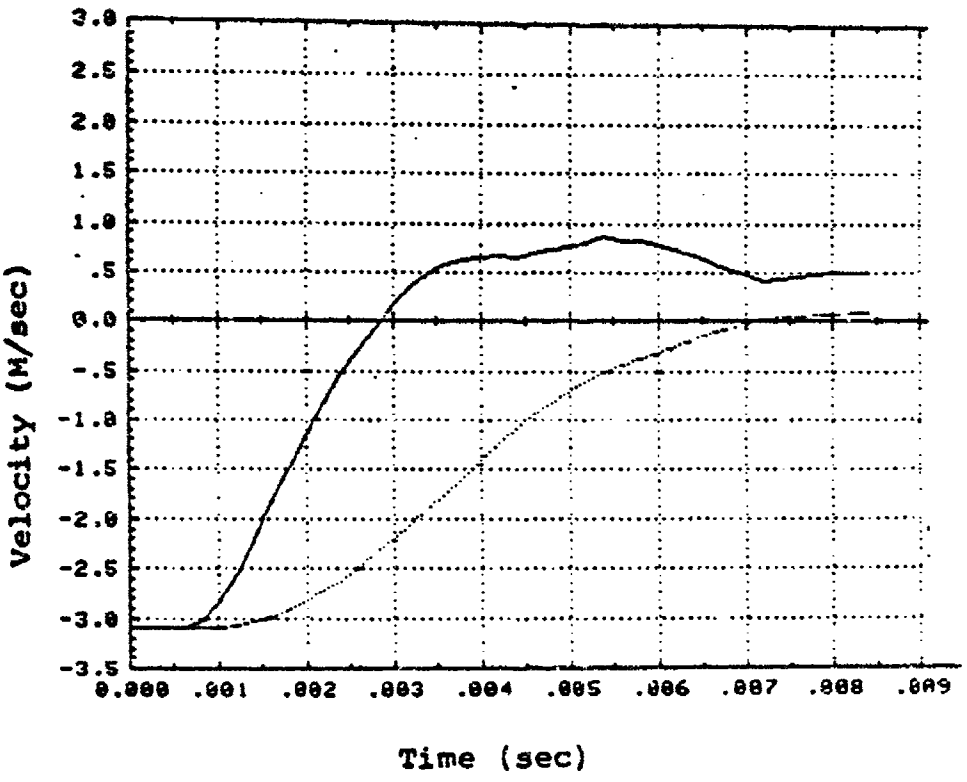

B

Fig. 22 Time History of the Position and Velocity of Shell and Headform for Soft Case

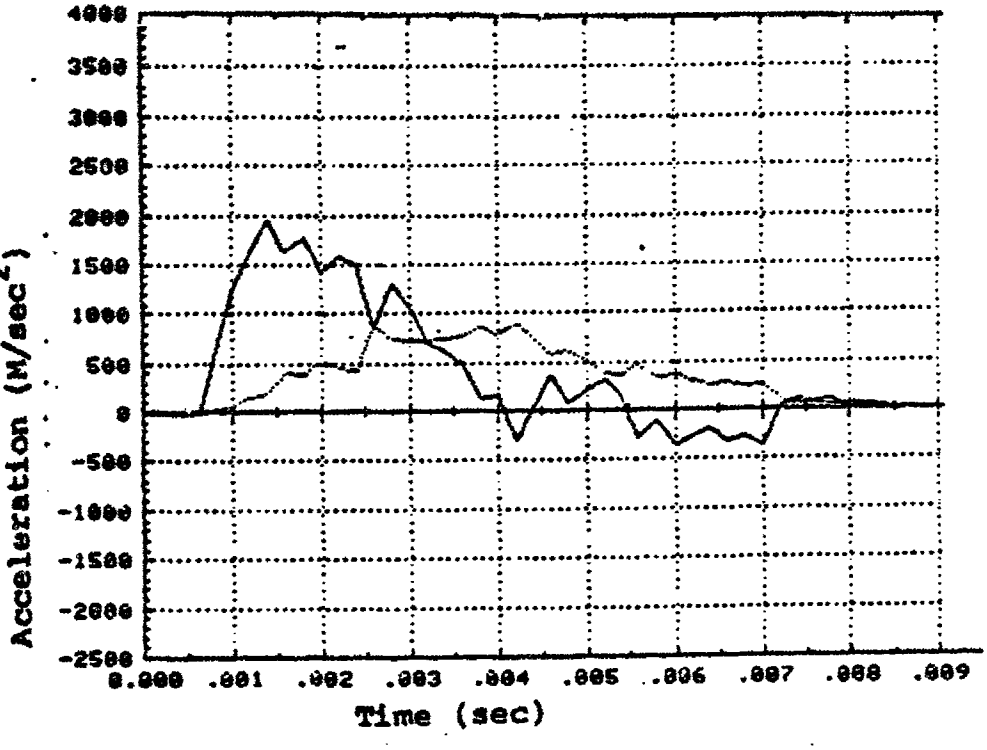

C

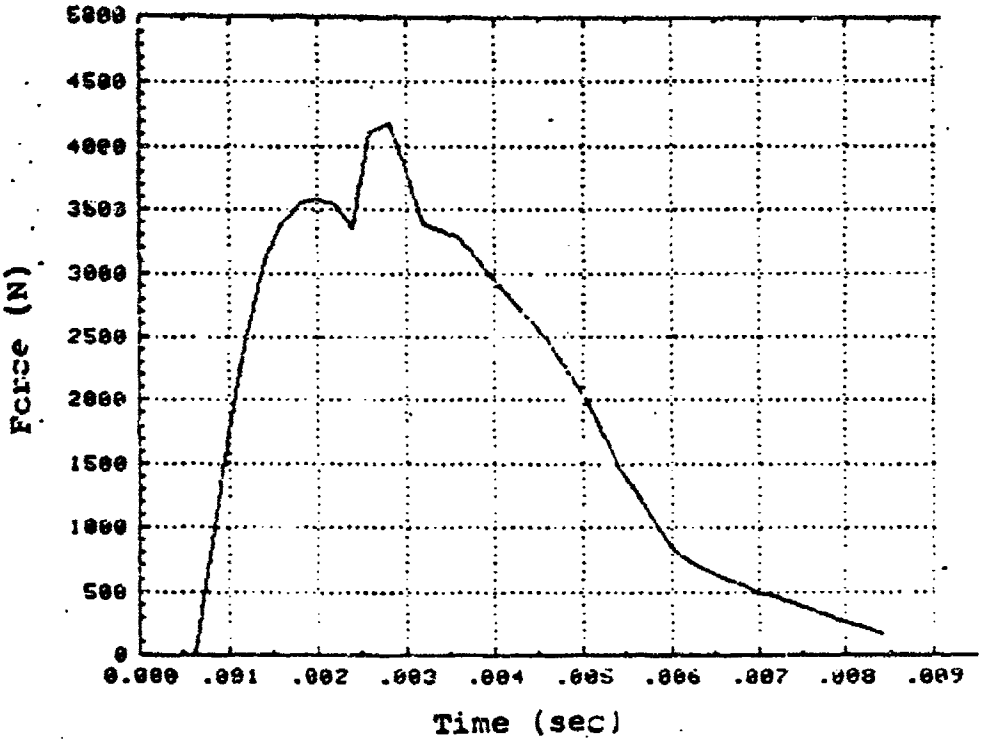

D

Fig. 22 Time History of the Acceleration of Shell and Headform and Impact Force between Ground and Shell for Soft Case

APPENDIX A

MEDICINE AND SCIENCE IN SPORTS AND EXERCISE
Vol. 16, No. 5, pp. 498–505, 1984
0195-9131/84/1605-0498/$03.00/0

The inertial and geometrical properties of helmets

GLEN O. NJUS, Y. KING LIU, and THOMAS A. NYE

Department of Biomedical Engineering, College of Engineering, The University of Iowa, Iowa City, IA 52242

ABSTRACT

NJUS, GLEN O., Y. KING LIU, and THOMAS A. NYE. The inertial and geometrical properties of helmets. *Med. Sci. Sports Exerc.*, Vol. 16, No. 5, pp. 498–505, 1984. The center of gravity (CG) and the principal mass moments of inertia about the CG of Army aviator, American football, and bicycle helmets were experimentally determined by a variation of the classic differential weighing and torsional pendulum techniques. In the course of these experiments, an innovative method for three-dimensional (3D) digitization was found. An electronic caliper, which measured length, was used with a computer algorithm to achieve 3D digitization. The results of the above measurements show that the weight of the helmet and the distances from the CG to the orthogonal coordinate axes intercepts with the outer shell surface were highly correlated with its principal mass moments of inertia. A set of regression equations was derived on theoretical considerations and served to unify the experimentally obtained data. Our results indicate that the principal mass moments of inertia of helmets vary linearly with its mass but nonlinearly with size and shape. For a helmet, given its weight and certain geometrical distances, the regression equations estimate the principal mass moments of inertia to within 5% of its experimentally-determined values. For the helmets studied in this series, a modified linear-regression relationship between the principal mass moments of inertia and its mass was found. This result is reasonable because the mass distribution of the current generation of helmets are set primarily by the head size and secondarily by helmet size, shape, and materials.

FOOTBALL HELMET, AVIATOR HELMET, CENTER OF GRAVITY, MASS MOMENT OF INERTIA, BIOMECHANICS

The determination of the center of gravity (CG) and the magnitude of the principal mass moments of inertia (with its associated principal directions) are prerequisites to the solution of any problem in rigid-body dynamics. Several experimental methods exist to determine these inertial properties of a rigid body.

For a flat object, the method of suspension is ideal. The object is placed in suspension about some arbitrary point until equilibrium, then the center of gravity must lie on a vertical line through the point of suspension; the procedure is repeated for a second arbitrary point. The center of gravity lies at the point of intersection of the first and second lines. The method of balance consists of resting the flat object on a knife edge until precarious equilibrium is achieved; the procedure is also repeated for additional orientations. The intersection of the lines formed by the knife edge determines the center of gravity.

For an irregular three-dimensional (3D) object, the above procedure needs considerable modification before it becomes practical. A method developed by Williams and Lissner (5) for finding the weight of an in vivo body segment consists of weighing the entire body on two knife edges, with one of the knife edges resting on a weight scale. The distances from the other knife edge to the centers of gravity are assumed known. The center of gravity of the segment of interest is altered through an appropriate joint. The changes in the center of gravity location and the change in scale readings between the first and second weighing are noted. The segment weight is equal to the distance between the knife edges multiplied by the difference between scale readings and divided by the horizontal displacement of the center of gravity of the segment.

The procedure for the experimental determination of the mass moment of inertia matrix using either a torsional or planar pendulum oscillation technique has been delineated by Wells (4) and extensively reviewed and developed by Chandler et al. (1).

In the present study we determined the center of gravity (CG) of various helmets using a modification of the differential weighing technique. The torsional pendulum technique was adapted for the measurements of the mass moment of inertia of helmets about the CG with one plane of symmetry. Having determined the CG, the coordinates of any point on the rigid body, with respect to an orthogonal system about the CG, is very often a necessity. We have developed an electronic caliper for length measurements together with the appropriate software to convert these length data into three-dimensional coordinates.

MATERIALS AND METHODS

Determination of the inertial and geometrical properties was accomplished in three stages: 1) localization of the center of gravity (CG) and placement of a local

Submitted for publication May, 1983.
Accepted for publication March, 1984.

body fixed-Cartesian coordinate system at the CG, 2) determination of geometry of any point on the rigid body, and 3) determination of the principal mass moments of inertia and its associated directions about the CG. Each of these topics will be addressed individually.

Center of gravity determination. A modified version of the differential weighing method was used for localization of the helmet's CG. The use of the balance plate for differential weighing rests theoretically on the principles of statics. The experimental arrangement consisted of an aluminum balance plate supported by knife edges; the supports were maintained parallel to each other at a known distance apart by placing them in machined grooves at each end. Under one knife edge a weight balance or a force transducer was mounted. With only the balance plate in place, the summation of moments about knife-edge A in Figure 1a yields:

$$W_{bp}D_{bp} = F_{\beta}D_{\beta}, \qquad [1]$$

where W_{bp} is the weight of the balance plate acting through its CG at a distance D_{bp} from A, and F_{β} is the initial transducer output with a span length of D_{β} from A. With the helmet on the balance plate, we get:

$$W_hD_h + W_{bp}D_{bp} = (F_{\beta} + \Delta F_{\beta})D_{\beta}, \qquad [2]$$

where W_h is the helmet weight acting through its CG at a distance of D_h from A, and ΔF_{β} is the increase in the transducer output. Subtracting equation 1 from 2, we get either

$$D_h = \Delta F_{\beta}W_h/D_{\beta} \qquad [3a]$$

or

$$\Delta F_{\beta} = W_hD_h/D_{\beta}. \qquad [3b]$$

Because W_h and D_{β} can be predetermined and ΔF_{β} measured, one can either mark the helmet by moving some indicator through the distance D_h calculated from equation 3a or by fixing D_h and moving the helmet until a calculated ΔF_{β} from equation 3b is read on the transducer.

In our setup, we surrounded the balance plate on three sides with a C-channel frame positioned such that it spanned the midsection of the balance plate (see Figure 1b). Across the top of this frame was a linear series of small holes. The frame was placed such that the vertical plane passing through these holes intersected the balance plate along a line parallel to the knife edges. Care was taken to ensure that the vertical plane and the balance plate surface were perpendicular. Once this orientation had been achieved, the frame and plate supports were rigidly fixed.

A Cartesian coordinate system based on the CG was mapped onto the helmets using the following procedure. Prior to mapping, the system orientation was defined as the helmet in an upright position, i.e., point contact with a flat surface occurs at the back and at the ear flaps. For those helmets where these points were poorly defined, 20-gauge hypodermic needles were placed in the helmet shell such that point contact occurred. In all helmets, the contact points on the ear flaps were essentially symmetric about the midsagittal plane.

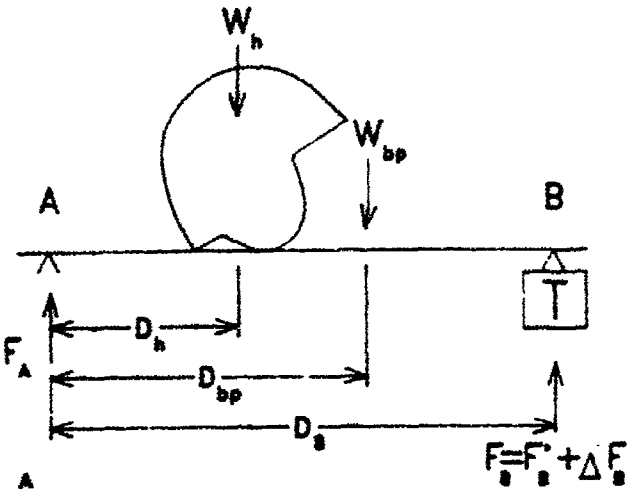

Figure 1a—Schematic diagram showing the differential weighing technique adapted for helmets. The helmet is shown in its reference orientation, i.e., contact with a flat surface occurs at three points: one at the back of the helmet and one at each ear flap.

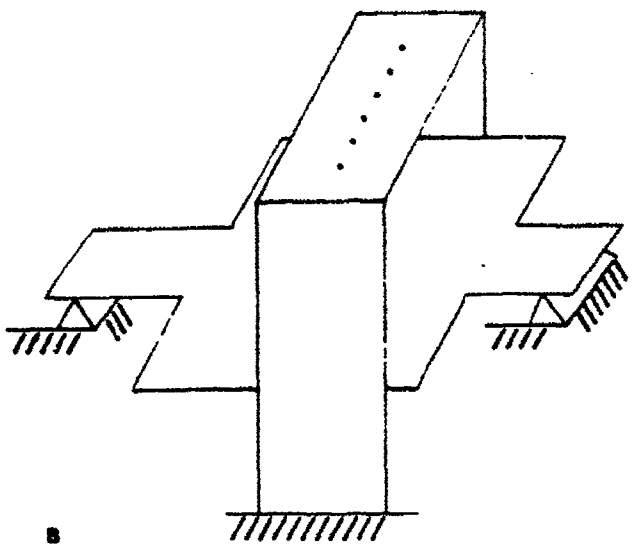

Figure 1b—Isometric view of C-channel frame surrounding the balance plate. Across the top of this frame are a linear series of small holes to allow a pendulum bob carrying a felt-tip pen to mark the outside surface of the helmet.

The distance, D_h, was set to be the horizontal distance from edge A to the vertical plane passing through the holes in the channel frame. Using equation 3b, a value of ΔF_{β} was calculated. The helmet was moved along the plate in planar motion until the calculated ΔF_{β} coincided with the output from the transducer. At this point, the CG of the helmet is contained in the vertical plane passing through the C-channel frame. The helmet was then marked using a pendulum with an inked felt-tip pen which was successively suspended from each hole in the frame, and a line was drawn through the marked points. The helmet was then rotated through increments of approximately 60° until three intersecting lines were drawn. A perspective view of the helmet axis system and inter-

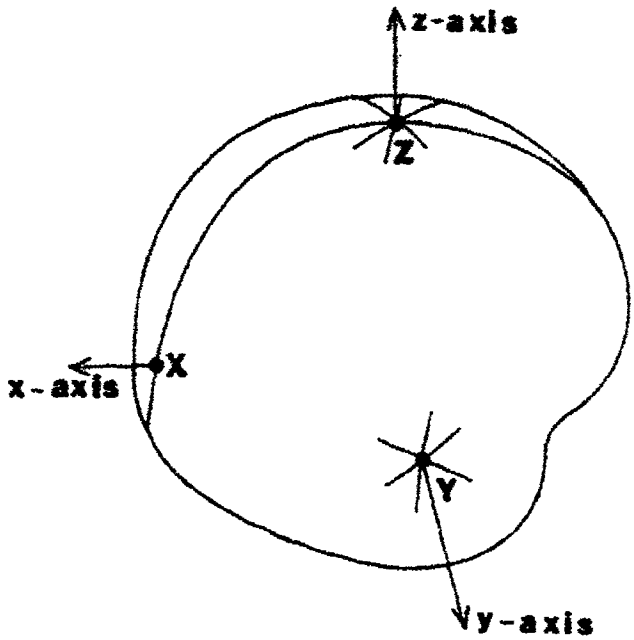

Figure 2—Perspective view of helmet axis system and mapping lines.

secting mapping lines is shown in Figure 2. This intersection ideally should be, and in fact was, consistently within 1 mm of being a point. This point, Z, on the helmet should be along a vertical line passing through the CG, i.e., the z-axis intercept.

To obtain the y-axis intercept, the helmet was rotated until the z-axis was in a horizontal plane. This was accomplished with the aid of a precision rectangular Plexiglas block. The block was placed on a horizontal surface and the helmet positioned with the aid of lightweight styrofoam wedges such that the two ear-flap contact points were vertical, i.e., along the edge of the block. Once this position was attained, the wedges were bonded to the helmet surface. The differential weighing procedure was repeated to obtain the +y-axis intercept. The −y-axis intercept, i.e., −Y, was mapped with the aid of a sharp pointer inserted into the center of the balance plate at a distance of D_b from A. The helmet was placed on the balance plate with the +Y point on the pointer. The helmet was then tipped with the aid of styrofoam shims until the transducer output reached the calculated ΔF_b. The plumb bob was used to mark −Y point. The x-axis intercept, X, was found by positioning the helmet in the reference orientation and measuring the vertical distance from the ear flap contact points to ±Y. This measured distance was marked as a line above the contact point of the back of the helmet. The x-z plane was inscribed by rotating the helmet forward (about a line parallel to the Y-axis) about the ear-flap contact points. The intersection between the previously marked horizontal line and the inscribed line determined the X point. The distances XY and −YX should be equal.

Upon obtaining the three marked points on the surface of the helmet, the actual location of the CG is found by assuming an orthogonal coordinate system which intersects the three points simultaneously. Figure 3a illustrates the geometrical relationship between the three points, X, Y, and Z, and the CG. By the Pythagorean Theorem, we get three nonlinear algebraic equations:

$$a^2 + b^2 = A^2 \quad [4]$$

$$a^2 + c^2 = C^2 \quad [5]$$

$$b^2 + c^2 = B^2, \quad [6]$$

where A, B, and C represent the physical distances XY, YZ, and XZ, respectively, on the helmet and a, b, and c represent the distances from the CG to the points X, Y, and Z, respectively. Subtracting [6] from [5] and adding the resultant to [4] yields

$$a = [(C^2 - B^2 + A^2)/2]^{1/2}. \quad [7]$$

Similarly,

$$b = [(A^2 - C^2 + B^2)/2]^{1/2} \quad [8]$$

$$c = [(B^2 - A^2 + C^2)/2]^{1/2}, \quad [9]$$

where positive signs were used in the above equations due to physical reasons.

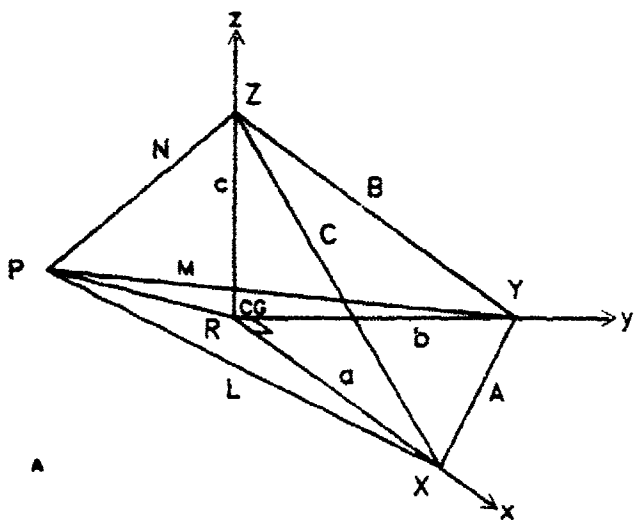

Figure 3a—The geometrical relationship between the center of gravity (CG) of the rigid body and the x, y, and z axis intercepts: X, Y, and Z, as well as a generic point (P).

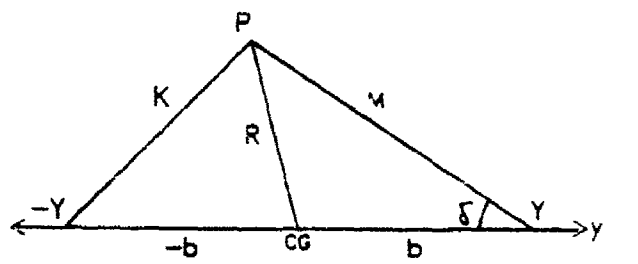

Figure 3b—The geometrical relationship between the center of gravity (CG) of the rigid body and the ±Y intercepts as well as a generic point (P).

Three-dimensional coordinate determination. Having an orthogonal coordinate system fixed to the CG, it is theoretically possible to obtain the coordinates of any generic point, P, on the helmet. Referring again to Figure 3a, we note from the law of cosines that

$$L^2 = R^2 + a^2 - 2aR_x \quad [10a]$$

$$M^2 = R^2 + b^2 - 2bR_y \quad [10b]$$

$$N^2 = R^2 + c^2 - 2cR_z \quad [10c]$$

where R_x, R_y, and R_z represent the vector components of $\bar{R}$, the position vector from the CG to the point, P. Because the direction cosines, l, m, and n, of the vector $\bar{R}$ are defined by : $l = R_x/|R|$, $m = R_y/|R|$, and $n = R_z/|R|$, we obtain R_x, R_y, and R_z from equation 10 to yield

$$l = (a^2 - R^2 - L^2)/2|\bar{R}|a \quad [11a]$$

$$m = (b^2 + R^2 - M^2)/2|\bar{R}|b \quad [11b]$$

$$n = (c^2 + R^2 - N^2)/2|\bar{R}|c. \quad [11c]$$

In theory, if we can measure the distances, L, M, N, and $|\bar{R}|$, we can solve for the direction cosines via equation 11 because a, b, and c are given in [7] – [9]. Practically, however, $\bar{R}$ is physically difficult to obtain. To get $|\bar{R}|$, we take advantage of midsagittal plane symmetry and pick a convenient auxiliary point, −Y, on the shell. Referring to Figure 3b, we apply the law of cosines twice: once for the entire triangle and once for the smaller triangle on the right, it can be easily shown that

$$R^2 = (M^2 + K^2 - 2b^2)/2, \quad [12]$$

where K is the distance from −Y to the generic point, P. Thus, by making an additional distance measurement, we can obtain R.

In practice, we used equation 12 to estimate R, substituted it into equation 11 to obtain the direction cosines l, m, and n. These calculated values were substituted into the well-known constraint equation:

$$l^2 + m^2 + n^2 = 1. \quad [13]$$

If the sum of the squares of the direction cosines is $1 \pm \epsilon$ (where ϵ is a small number), the values of l, m, and n were considered adequate. Otherwise, the value of R was iterated until the criterion was met. The above iteration procedure is in the form of an efficient computer algorithm and yields results almost as soon as the physical measurements are completed. Thus, given the distances A, B, C, L, M, N, and K, a simple vector analysis yields the position vector, i.e., three-dimensional digitization, from a reference point. What is required is a device to accurately measure these distances.

Electronic caliper. An electronic caliper, shown in Figure 4, was designed to make these linear measurements. It consists of a three-bar planar linkage arranged in a U-shape configuration. The two hinge joints are two linear, high-precision rotational potentiometers. The voltage output of each potentiometer is proportional to the angle between the associated free arm and a known reference position. The analog signals are converted to digital ones through a minicomputer (PDP 11/34) and all subsequent processing is in the digital mode. Digitization is at a rate of 1 kHz and duration of 0.1 s. A foot switch triggers A/D conversion and enters the distance being measured

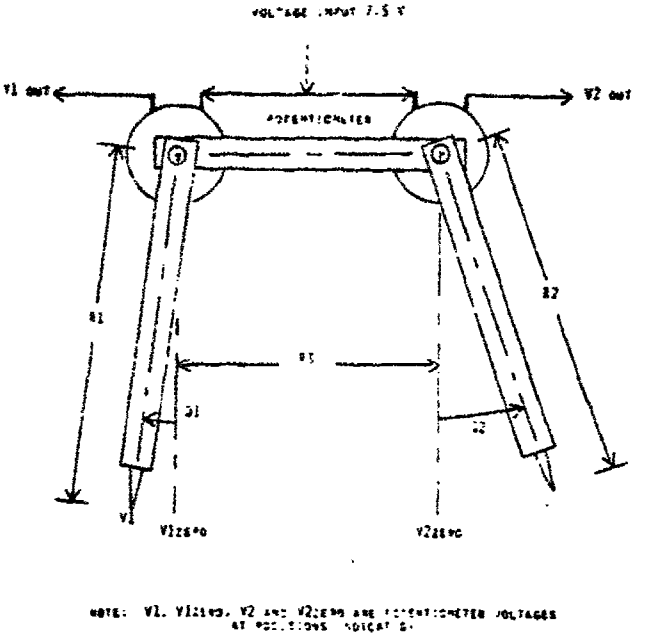

Figure 4—The electronic caliper used to obtain length measurements. The two hinge joints are two linear, high-precision rotational potentiometers. The voltage output of each potentiometer is proportional to the angle between the free arm and a known reference position.

by the hands holding onto the two arms of the caliper. Accuracy was ± 0.4 mm over a range of 40 cm.

Using the caliper device an operator can do three-dimensional digitization. In this mode the first three distances entered determine an orthogonal coordinate system. Each subsequent set of four distances uniquely determines the Cartesian coordinates of a given point relative to the system established. As stated previously, the value of R was iterated because its input value was only approximate. This iteration was continued until the right side of equation 13 was equal to 1 ± 0.01. Convergence was always achieved within 30 steps and usually within 10. While the electronic caliper was used to determine the coordinates of selected points on the helmet shell in this project, it is potentially suitable for three-dimensional digitization of any geometry.

Mass moment of inertia. If one assumes midsagittal plane symmetry, e.g., x-z plane, the mass moment of inertia matrix about the CG reduces to five non-zero components:

$$I_{ij} = \begin{matrix} I_{xx} & 0 & I_{xz} \\ 0 & I_{yy} & 0 \\ I_{xz} & 0 & I_{zz} \end{matrix}$$

The method for the determination of the mass moments of inertia about a given axis via the torsional pendulum technique is well-known, see e.g., Liu et al. (2). The only non-zero off-diagonal term is I_{xz}. It is quite well-established, see e.g., Wells (4), that

$$I_{xz} = \frac{I_{xx}\lambda^2 + I_{yy}\mu^2 + I_{zz}\nu^2 - I_{qq}}{2\nu\mu}, \quad [14]$$

where I_{qq} is the mass moment of inertia about an arbitrary q-q axis and λ, μ, ν are its direction cosines.

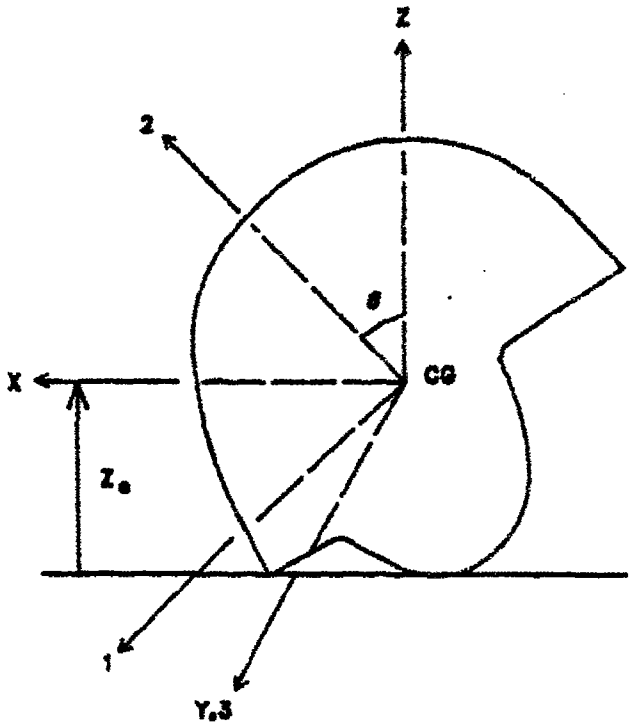

Figure 5—Due to midsagittal symmetry, one of the principal axes coincides with y-axis. The other two are located through an angular rotation, θ, as given in equation 17.

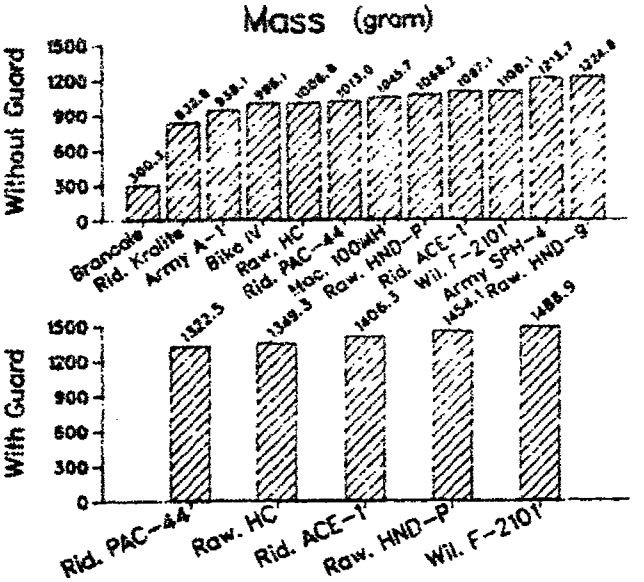

Figure 6—The mass of Army aviator, American football, and bicycle helmets. The abbreviations represent the following: 1) Brancale = bicycle helmet; 2) Rid Kralite = Riddell football helmet Model Kralite; 3) Army A-1 = Army aviator experimental helmet; 4) Bike IV = Bike football helmet Model IV; 5) Raw. HC = Rawlings football helmet Model HC; 6) Rid. PAC-44 = Riddell football helmet Model PAC-44; 7) Mac. 100MH = MacGregor football helmet Model 100-MH; 8) Raw. HND-P = Rawlings football helmet Model HND-P; 9) Rid. ACE-1 = Riddell football helmet Model ACE-1; 10) Wil. F-2101 = Wilson football helmet Model FS101; 11) Army SPH-4 = Army aviator helmet Model SPH-4; and, 12) Raw. HND-9 = Rawlings football helmet Model HND-9.

Experimentally, I_{xy} was obtained via the torsional pendulum technique and the direction cosines λ, μ, and ν were found by using the electronic caliper and the computer algorithm.

To obtain the principal mass moments of inertia and its associated directions, we can use either Mohr's circle or classic analysis (3). In either case, one gets

$$I_{1,2} = \frac{I_{xx} + I_{zz}}{2} \pm \left(\frac{I_{xx} - I_{zz}}{2} + I_{xz}^2\right)^{1/2}. \quad [15]$$

$$I_3 = I_{yy}, \quad [16]$$

and

$$2\theta = \tan^{-1}\frac{2I_{xz}}{I_{xx} - I_{zz}}, \quad [17]$$

where I_1, I_2, I_3 are the principal mass moments of inertial and θ is the needed rotation of the x and z axes about the y-y axis to yield the principal directions as shown in Figure 5.

RESULTS

The weight (mass), center of gravity (mass), and the principal mass moments of inertia of one bicycle, two Army aviator, and nine American football helmets were obtained. The mass in grams, with and without the face-guard, are shown in Figure 6. Using the upright position of the helmet, as the reference orientation, the CG is located by a vertical distance, Z_c, from a flat surface. The calculated distances a, b, and c serve as a measure of helmet size. These results are given in Table 1. From this reference orientation, the distance from the CG to any point can be measured. For example, when worn, the distance from the helmet's CG to the zero tangent point of the ear flap can be easily determined using the 3D digitization scheme delineated earlier.

The product moment of inertia, i.e., I_{xz}, and the angular rotation, θ, to obtain the principal directions are shown in bar graphs in Figure 7. The mass moments of inertia about the orthogonal coordinate system placed at the CG of the helmets in the reference configuration, with and without a face-guard, are shown in Table 2. The principal mass moments of inertia together with the angle of rotation, θ, defining the principal directions are given in Table 3.

DISCUSSION

Prior to the CG and the mass moment of inertia determination, the instruments were all calibrated. The CG determination was checked with a high-precision machined Plexiglas rectangular block. Its x-, y-, and z-axis intercepts are easily determined by geometry and checked

TABLE 1.The distances, a, b, and c, from the CG to the x, y, z axis intercepts, X, Y, and Z together with the vertical distance, Z_c, of the helmets studied. The a, b, and c lengths yield measures of the size of the helmet and Z_c, the height of the helmet's CG from a reference configuration.

	Geometrical Data (cm)			
	a	b	c	Z_c
Without Guard				
Army A-1	12.32	12.98	13.12	/
Army SPH-4	11.56	12.42	11.88	/
Bike IV	11.58	11.22	11.51	12.73
Brancale	10.41	9.30	8.67	5.97
Mac. 100MH	11.46	10.95	10.53	12.94
Raw. HC	11.93	10.81	10.85	/
Raw. HND-9	12.07	11.30	10.45	13.51
Raw. HND-P	12.58	11.48	10.75	12.39
Rid. ACE-1	11.38	11.01	10.77	12.39
Rid. Kraliie	11.31	10.67	11.17	12.01
Rid. PAC-44	10.88	10.95	10.63	12.39
Wil. F-2101	11.73	11.18	10.64	12.29
With Guard				
Raw. HC	15.57	10.70	12.00	/
Raw. HND-P	16.63	11.15	11.97	11.25
Rid. ACE-1	14.44	10.87	11.95	11.45
Rid. PAC-44	14.04	11.00	11.21	12.04
Wil. F-2101	15.56	12.80	11.70	11.51

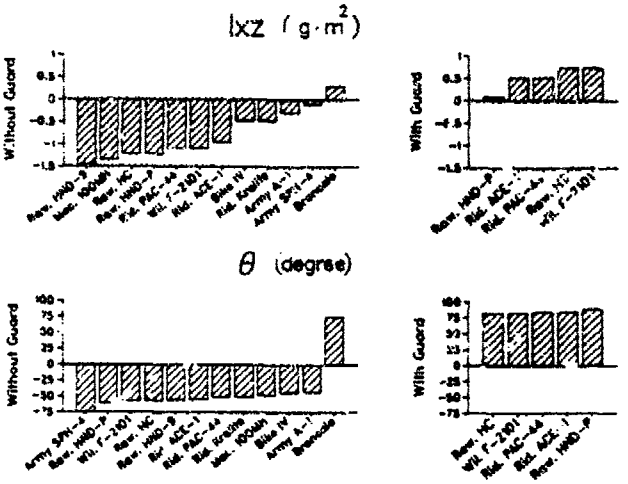

Figure 7—The product moment of inertia, I_{xz}, and the angular rotation, θ, required to obtain the principal directions, assuming midsagittal plane symmetry, for the helmets studied.

against the balance plate method. The resolution of the CG determination technique is 0.5 mm. The location of the x- and z-axis intercepts, i.e., X and Z points, invariably coincided closely with mold lines for the helmet shell, affirming the essential correctness of the midsagittal plane symmetry assumption.

The 3D digitization method was compared with one that has been commercially available (Graf-Pen 3-D Digitizer, Science Accessories Corporation, Southport, CT 06490). The operation of the Graf-pen system utilizes the essential constancy of the speed of sound in air. A spark gap, placed at the point to be digitized, when fired, creates a spherical sound wave which is picked up by three linear microphones arranged as an orthogonal array. The time it takes the sound wave to reach a given microphone yields the magnitude of the distance given the constancy of the velocity of sound. The system has the advantage of speed but is not without its problems, the spark gap sometimes misfires, and there are restrictions in terms of the location of the spark gap. No obstructions are allowed between the spark gap and the linear microphones. When compared against this sophisticated and expensive system on a standard rectangular calibration block, our system was more accurate, even though it took four times as long. On experimental helmets, the two methods provide similar results.

The center of gravity (mass) and the principal mass moments of inertia of a rigid body are measures of the mean and the distribution of mass points about the mean, i.e., about an orthogonal coordinate system fixed at the center of gravity. From the theoretical point of view, the helmet may be idealized as a hollow ellipsoid whose principal mass moments of inertia about its CG are:

$$\begin{aligned} \bar{I}_{xx} &= [m_o(b^2 + c^2) - m_i(b_i^2 + c_i^2)]/5 \\ \bar{I}_{yy} &= [m_o(a^2 + c^2) - m_i(a_i^2 + c_i^2)]/5 \\ \bar{I}_{zz} &= [m_o(a^2 + b^2) - m_i(a_i^2 + b_i^2)]/5, \end{aligned} \quad [18]$$

where m_o and m_i are the mass of outer and inner ellipsoid, respectively, and a_i, b_i, and c_i are the inner ellipsoid axis-intercepts with the x, y, and z axes, respectively.

If one defines the characteristic thickness in the three coordinate directions as:

$$\begin{aligned} r &= a - a_i \\ s &= b - b_i \\ t &= c - c_i, \end{aligned} \quad [19]$$

it is easily shown that

$$\begin{aligned} \bar{I}_{xx} &= [m(b^2 + c^2)/5] + m_i[(b^2 + c^2) - (b_i^2 + c_i^2)]/5 \\ \bar{I}_{yy} &= [m(a^2 + c^2)/5] + m_i[(a^2 + c^2) - (a_i^2 + c_i^2)]/5 \\ \bar{I}_{zz} &= [m(a^2 + b^2)/5] + m_i[(a^2 + b^2) - (a_i^2 + b_i^2)]/5, \end{aligned} \quad [20]$$

where $m = m_o - m_i$ = the mass of the hollow ellipsoid. Thus, for the nonhomogeneous helmets considered here, the most appropriate form of the regression equation for the three principal mass moments of inertia are:

$$\bar{I}_{xx} = C_1 m(b^2 + c^2) + C_2(b^2 + c^2) + C_3$$
$$\bar{I}_{yy} = C_4 m(a^2 + c^2) + C_5(a^2 + c^2) + C_6 \quad [21]$$
$$\bar{I}_{zz} = C_7 m(a^2 + b^2) + C_8(a^2 + b^2) + C_9,$$

where $C_1, C_2 \ldots C_9$ are regression coefficients.

For the helmets studied, it appears that the weight (mass) and the geometrical distances, a, b, and c, are highly correlated with the principal mass moments of inertia as shown in Table 4. For instance, even when football and Army aviator helmets were mixed, the correlation coefficients for the linear regression ranged from 0.88 to 0.98 in Table 4.

To validate these regression equations, a Riddell Model PAC-3 football helmet was weighed. Substituting its mass of 1049.9 g into the regression equations for football helmets without face-guards in Table 4 yielded the predicted inertial properties shown in Table 5. The difference between experimentally-determined and the predicted values shown in Table 5 is less than 3%.

An examination of Table 1 showed that a, b, and c for football helmets are all in the range of 10.5 to 12.6 cm, i.e., an ellipsoid with eccentricities small enough to be considered practically a sphere. For a sphere of radius R, the mass moment of inertia about any diameter is $I = 2mR^2/5$. It is not too far-fetched to assume that the principal mass moments of inertia might be linearly correlated with mass, i.e.,

TABLE 2. The numerical values of the mass moments of inertia about the orthogonal coordinate system fixed to the CG of the various helmets in the reference configuration with and without a face-guard. Midsagittal plane symmetry of the helmet is assumed.

	Moment of inertia (g · m²)			
	Without Guard			
	Ix	Iy	Iz	Ixz
Army A-1	9.8	6.4	9.8	−0.30
Army SPH-4	11.1	8.9	11.4	−0.11
Bike IV	8.9	8.7	8.9	−0.48
Brancale	1.6	1.9	2.6	0.30
Mac. 100MH	9.6	9.7	10.0	−1.35
Raw. HC	8.4	8.8	9.5	−1.23
Raw. HND-9	10.8	11.7	11.9	−1.46
Raw. HND-P	9.5	9.9	11.0	−1.23
Rid. ACE-I	9.2	9.7	9.9	−0.96
Rid. Kralite	7.0	6.9	7.3	−0.48
Rid. PAC-44	8.5	8.8	9.0	−1.10
Wil. F-2101	9.0	9.5	10.0	−1.10
	With Guard			
Raw. HC	11.6	15.4	16.8	0.75
Raw. HND-P	13.0	18.0	20.0	0.09
Rid. ACE-I	12.0	15.9	16.9	0.52
Rid. PAC-44	11.0	14.9	15.8	0.52
Wil. F-2101	12.7	17.5	18.5	0.75

TABLE 3. The numerical value of the principal mass moments of inertia together with the angular rotation, θ, required to yield the principal directions. Midsagittal plane symmetry is assumed.

	Principal inertia (g · m²)			
	Without Guard			
	$\bar{I}_x$	$\bar{I}_y$	$\bar{I}_z$	θ
Army A-1	9.5	6.4	10.1	−43.0
Army SPH-4	11.0	8.9	11.5	−74.7
Bike IV	8.4	8.7	9.4	−44.7
Brancale	1.5	1.9	2.7	74.7
Mac. 100MH	8.4	9.7	11.2	−48.5
Raw. HC	7.6	8.8	10.3	−56.6
Raw. HND-9	9.8	11.7	12.9	−55.8
Raw HND-P	8.8	9.9	11.7	−60.6
Rid. ACE-I	8.6	9.7	10.6	−54.8
Rid. Kralite	6.7	6.9	7.6	−51.1
Rid. PAC-44	7.6	8.8	9.9	−51.4
Wil. F-2101	8.3	9.5	10.7	−57.2
	With Guard			
Raw. HC	11.5	15.4	16.9	82.0
Raw. HND-P	13.0	18.0	20.0	89.3
Rid. ACE-I	12.0	15.9	17.0	84.0
Rid. PAC-44	10.9	14.9	15.8	84.0
Wil. F-2101	12.6	17.5	18.6	82.8

TABLE 4. The regression equations relating to the geometrical distances, a, b, and c and the mass m with the principal mass moments of inertia of helmets. Note the high correlation coefficients (0.88 to 0.98) even when Army aviator and football helmets were mixed.

Condition	Linear Regression Equation Principal Inertias	Correlation Coefficient
Army Helmets	$\bar{I}_x = 2.0896 + 0.3599(m[b^2 + c^2]) - 117.2587(b^2 + c^2)$	0.9802
Football Helmets	$\bar{I}_y = 14.4029 + 0.3532(m[a^2 + c^2]) - 576.3202(a^2 + c^2)$	0.8816
w/o guards	$\bar{I}_z = 5.3933 + 0.3993(m[a^2 + b^2]) - 224.7582(a^2 + b^2)$	0.9328
	$\bar{I}_x = 1.3404 + 0.3330(m[b^2 + c^2]) - 58.5445(b^2 + c^2)$	0.9640
Football Helmets	$\bar{I}_y = 7.6652 + 0.4676(m[a^2 + c^2]) - 442.7299(a^2 + c^2)$	0.9800
w/o guards	$\bar{I}_z = 5.5086 + 0.4518(m[a^2 + b^2]) - 280.4813(a^2 + b^2)$	0.9529

TABLE 5. Comparison between the inertial properties of a football helmet (Riddell PAC-3) predicted by the regression equations given in Table 4 and the experimentally-determined values.

Helmet	Calculated Principal Inertias	Experimental Principal Inertias	Percentage Error
Riddell	$\bar{I}_x = 8.33$	$\bar{I}_x = 8.1$	2.88
PAC-3	$\bar{I}_y = 9.37$	$\bar{I}_y = 9.2$	1.92
m = 1049.9 g	$\bar{I}_z = 10.31$	$\bar{I}_z = 10.2$	1.03

TABLE 6. The linear regression equations relating the principal mass moments of inertia to the mass of football helmets.

Condition	Linear Regression Equation Principal Inertias	Correlation Coefficient
Combined Army and	$I_x = 0.0078(m) + 0.4599$	0.7502
Football Helmets	$I_y = 0.0102(m) - 1.6414$	0.8011
(w/o guards)	$I_z = 0.0107(m) - 0.7238$	0.8866
	$I_x = 0.0077(m) + 0.2366$	0.9261
Football Helmets	$I_y = 0.0119(m) - 3.0531$	0.9768
(w/o guards)	$I_z = 0.0132(m) - 3.2626$	0.9332

$$I = C_{10}m + C_{11}, \qquad [22]$$

where C_{10} and C_{11} are linear regression coefficients. Table 6 yields the linear regression equations for the three principal mass moments of inertia for the helmets studied. Note that the correlation coefficients are only slightly lower than those in Table 4. Figure 8 displays the experimentally-determined principal mass moments of inertia as a function of the football helmet mass together with their linear regression lines. The slopes of these regression lines are slight, i.e., for the football helmets examined the inertial properties increase slowly with mass. For instance, the slope of $\bar{I}_z$ in Figure 8 is 0.013 g-m²/g.

If one were to substitute the Riddell Model PAC-3 data into the linear regression equations shown in Table 6, the difference between the experimentally-obtained data and the predicted values is less than 4%. Thus, in any dynamic

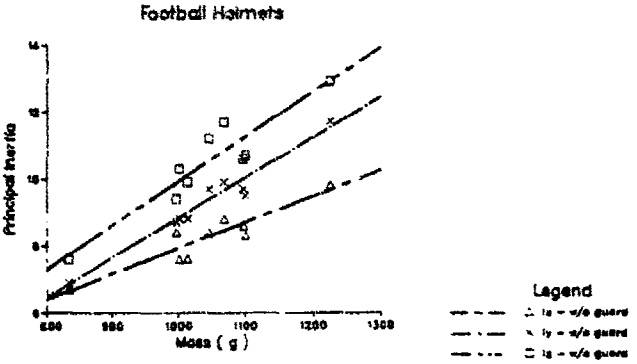

Figure 8—The linear regression equations relating the principal mass moments of inertia to the mass of the helmet together with the experimentally-determined principal mass moments of inertia of actual football helmets without face-guards.

study involving the current generation of football and Army aviator helmets, one can, given their mass, estimate their principal mass moments of inertia to within approximately 5% of their experimentally-determined values. The standard error of estimate for principal inertias of all helmets used in this study was 0.538 g-m² when using the linear regression equation. The above results are possible because the mass distribution of the current generation of helmets is primarily set by head size and secondarily by helmet size, shape, and materials. Should the size, shape, and material arrangement in the next generation of helmets be altered substantially, the more complex regression equations given in Table 4 will be more appropriate.

The present project was principally supported by the Helen Streiffer Fund of the University of Iowa Foundation. Partial funding was provided by Contract No. DAMD 17-81-C-1186 from the U.S. Army Aeromedical Research Laboratory, Ft. Rucker, Alabama and Grant No. GM 26608-03 from the National Institute for General Medical Sciences (NIGMS) of NIH.

REFERENCES

1. CHANDLER, R.F., J.T. CLAUSEN, H.M. MCCONVILLE, H.M. REYNOLDS, and J.W. YOUNG. *Investigation of Inertial Properties of the Human Body*. AMRL-TR-74-137, Wright-Patterson AFB, Ohio, 1974.
2. LIU, Y.K., J.M. LABORDE, and W.C. VAN BUSKIRK. Inertial properties of a segmented cadaver trunk: their implications in acceleration injuries. *Aerospace Med.* 42:650–657, 1971.
3. PLETTA, D.H. and D. FREDERICK. *Engineering Mechanics*. New York. Ronald Press, 1964, pp. 102–109.
4. WELLS, D.A. *LaGrangian Dynamics*, Schaum's Outline Series. New York: McGraw-Hill Book Co., 1967, pp. 132–133.
5. WILLIAMS, M. and H.R. LISSNER. *Biomechanics of Human Motion*. Philadelphia: W.B. Saunders Co., 1962, pp. 1–147.

Appendix B

The mode shapes of SPH-4 (Fig. B1) and A1 (Fig. B2) Army Aviator Helmets. The eigenvalues corresponding to these mode shapes are given in Table 2.

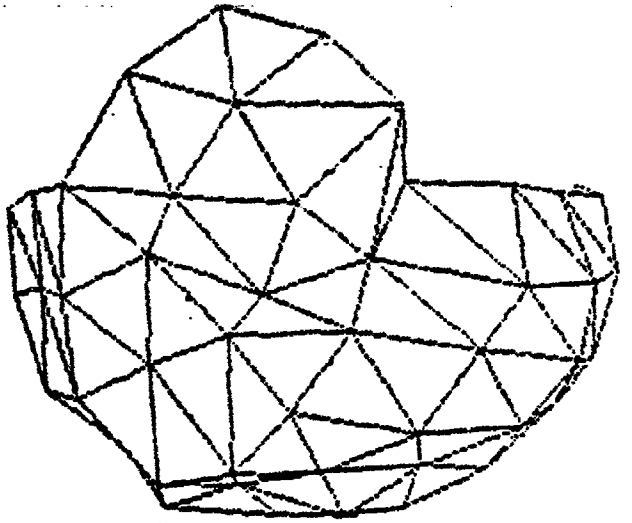

Mode 1 (SPH4)

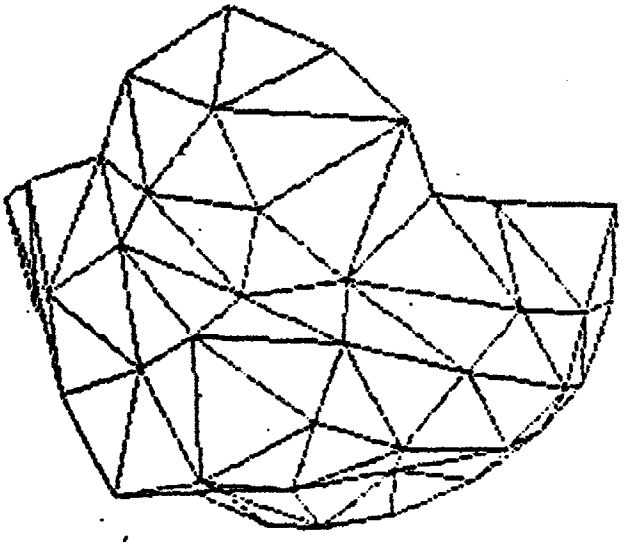

Mode 2 (SPH4)

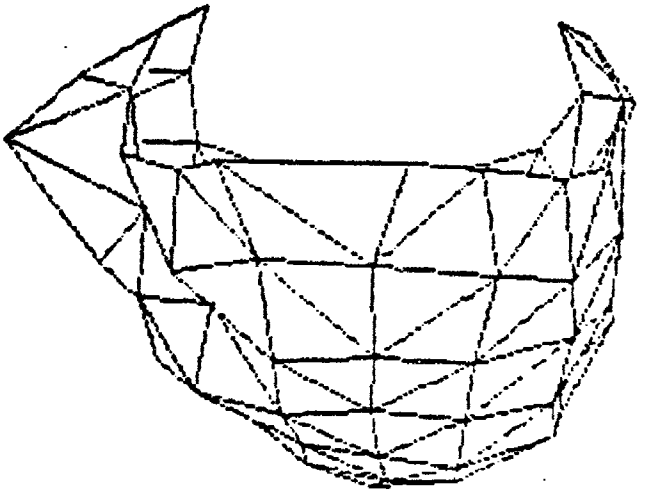

Mode 3 (SPH4)

Fig. B1 Vibration Modes for SPH4

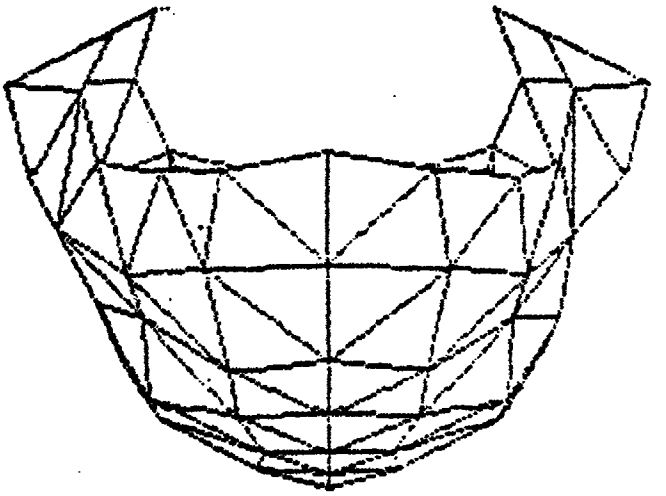

Mode 4 (SPH4)

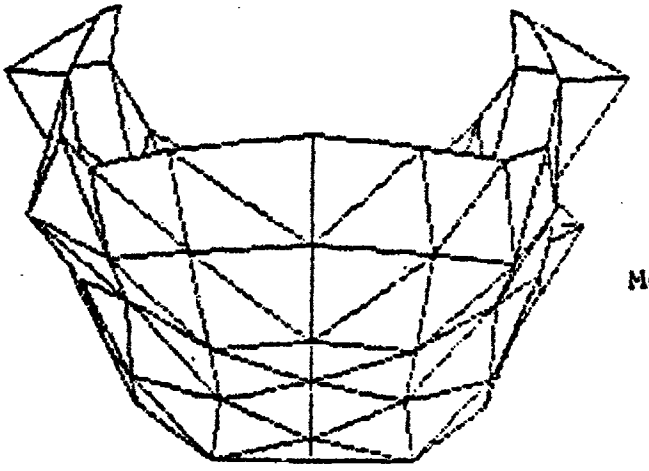

Mode 5 (SPH4)

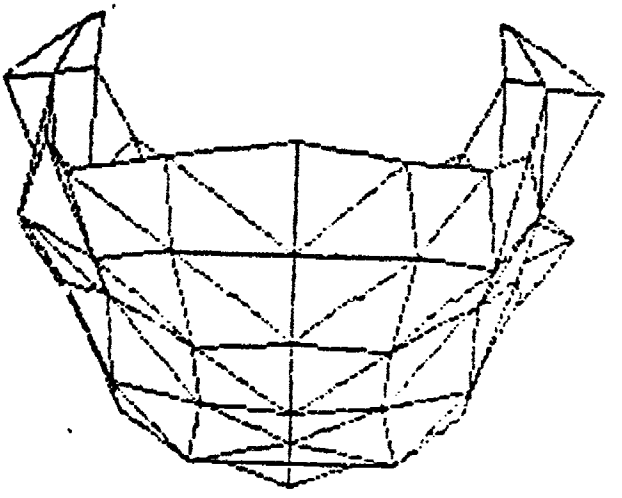

Mode 6 (SPH4)

Figure B1 (cont).

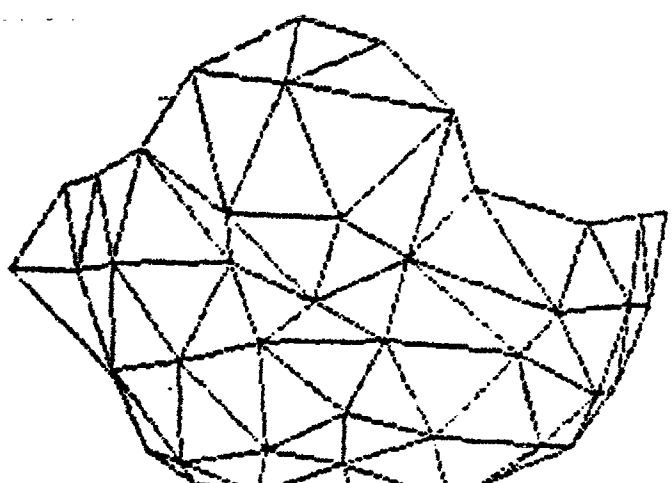

Mode 7 (SPH4)

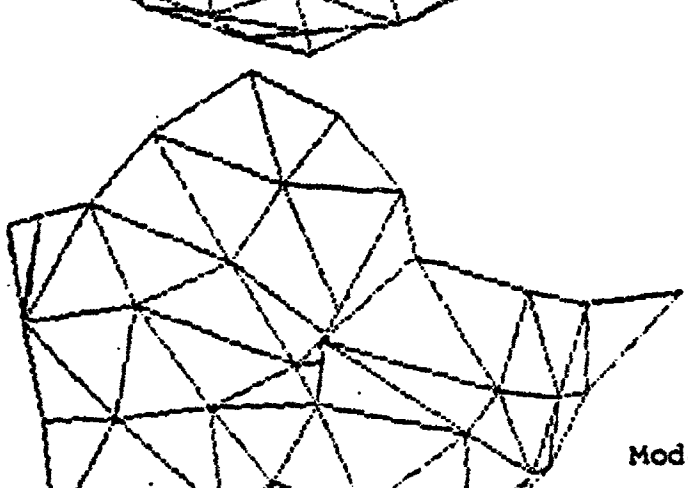

Mode 8 (SPH4)

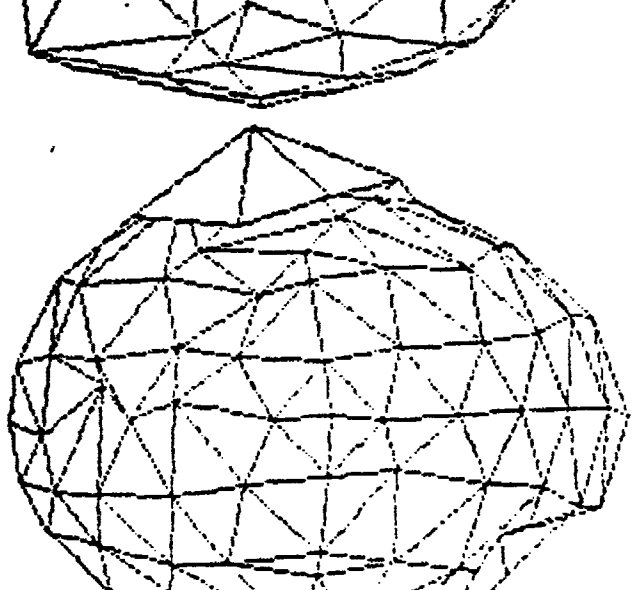

Mode 9 (SPH4)

Figure B1 (cont).

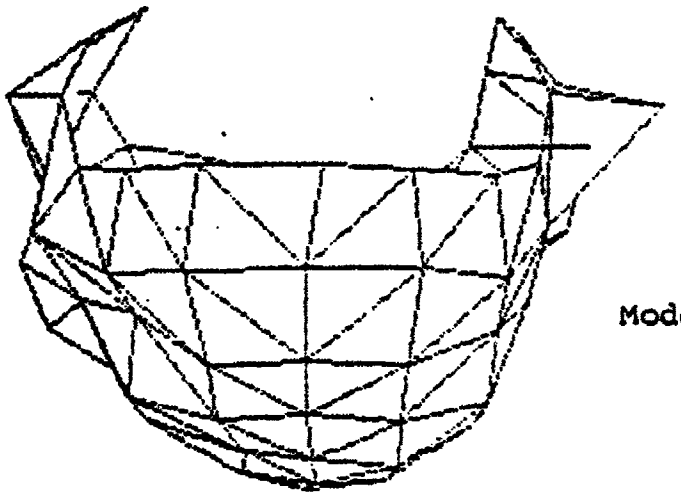

Mode 10 (SPH4)

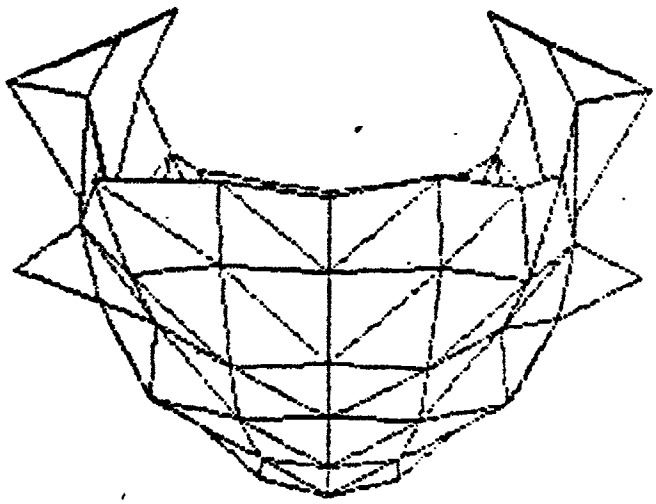

Mode 11 (SPH4)

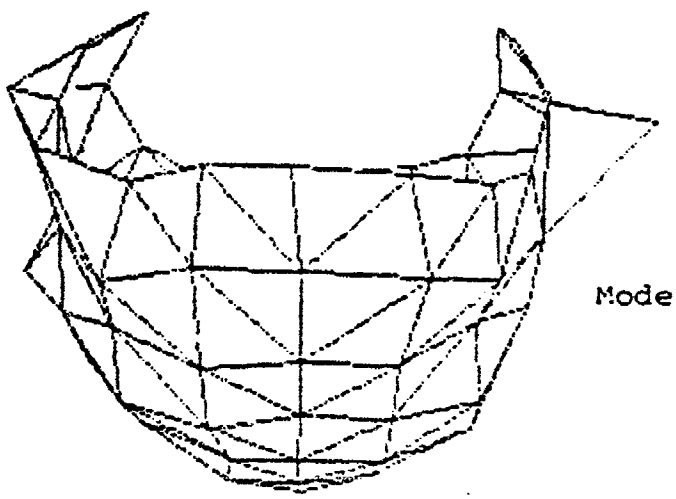

Mode 12 (SPH4)

Figure B1 (cont).

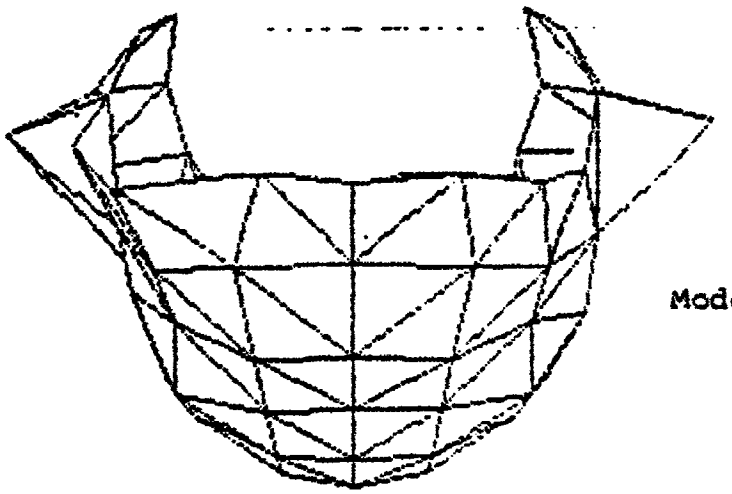

Mode 13 (SPH4)

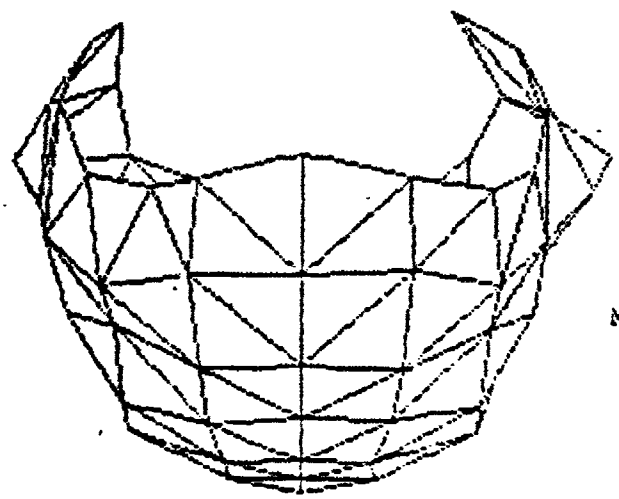

Mode 14 (SPH4)

Figure B1 (cont).

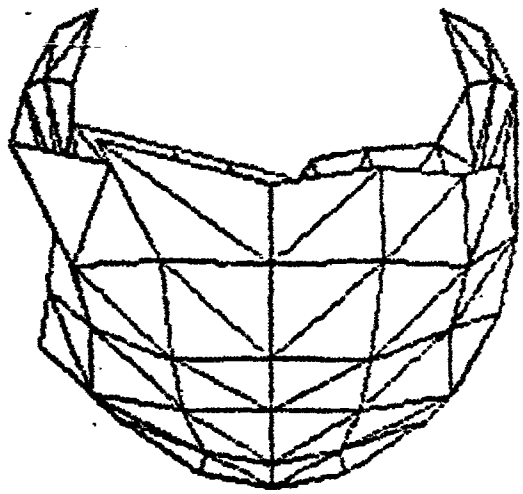

Mode 1 (A1)

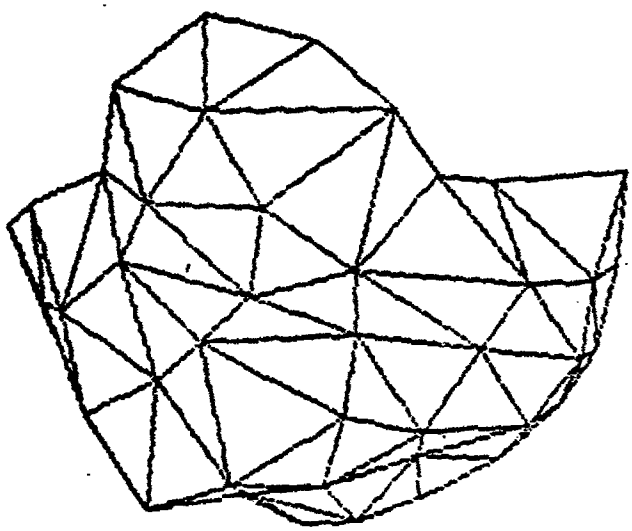

Mode 2 (A1)

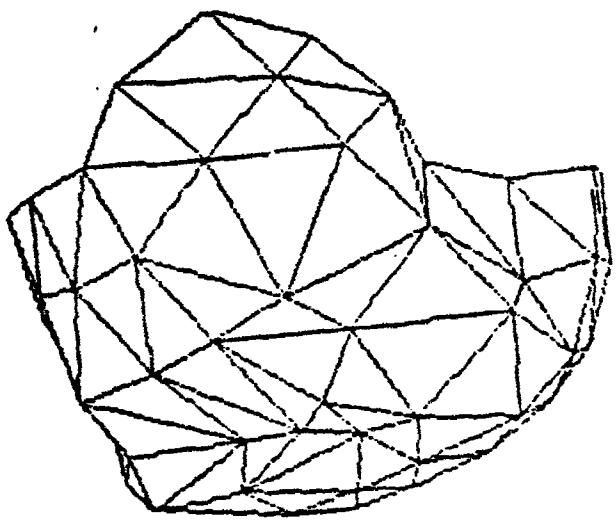

Mode 3 (A1)

Fig. B2: Vibration Modes for A1 Helmet

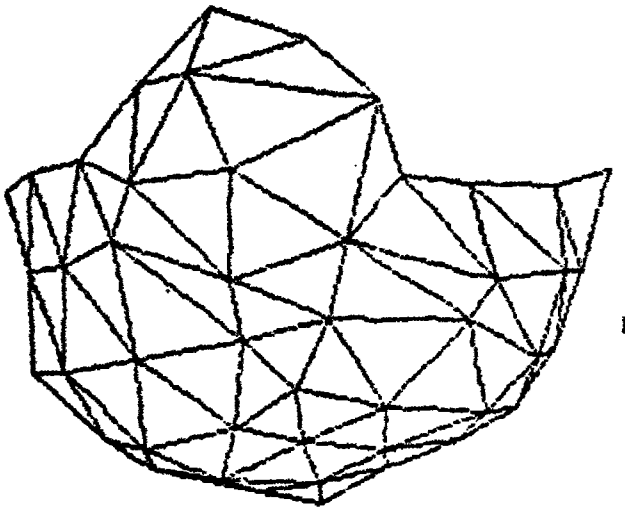

Mode 4 (A1)

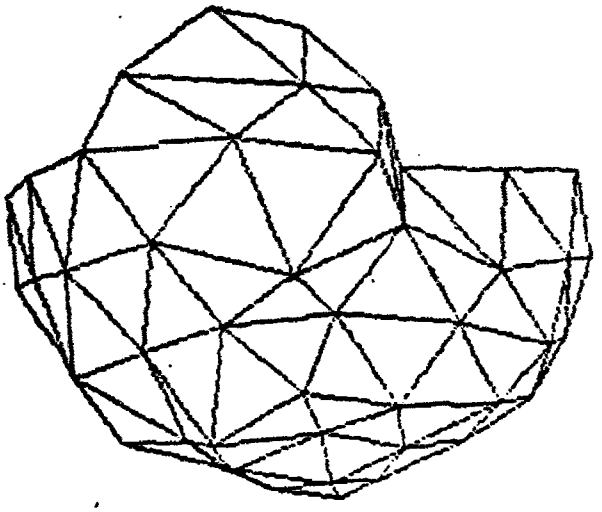

Mode 5 (A1)

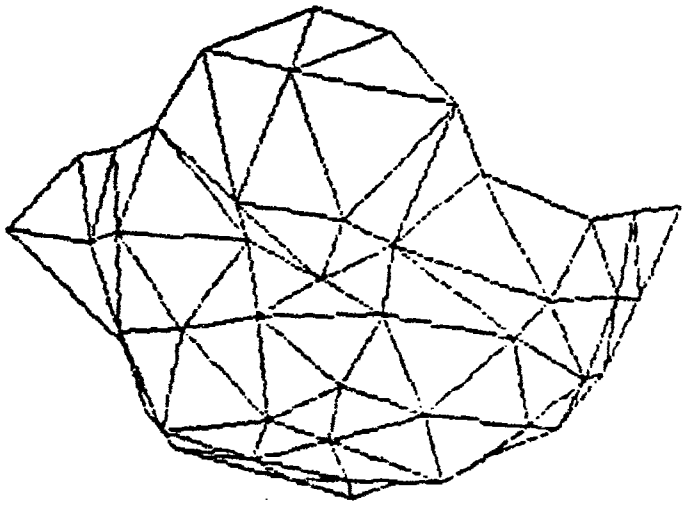

Mode 6 (A1)

Figure B2 (cont).

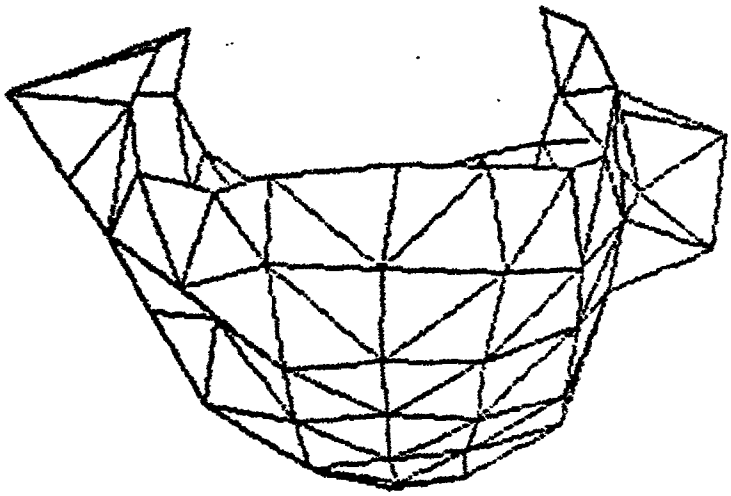

Mode 7 (A1)

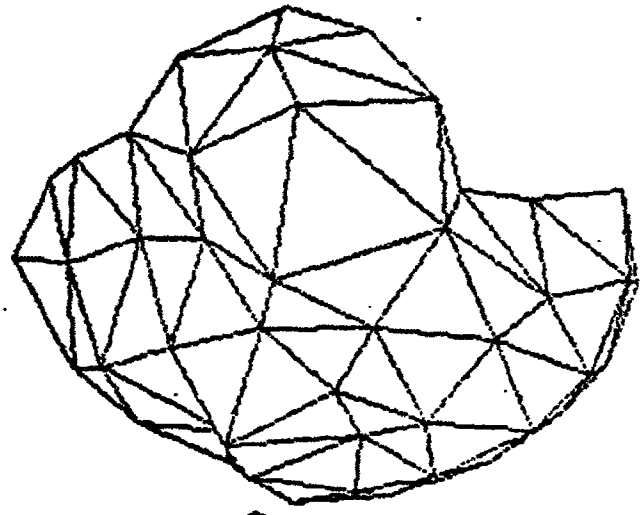

Mode 8 (A1)

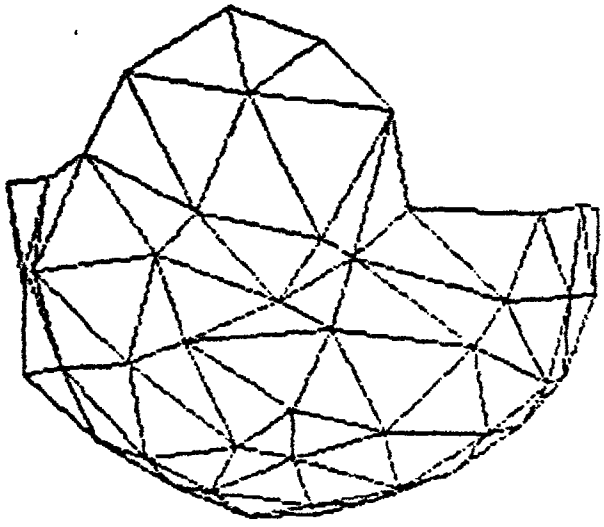

Mode 9 (A1)

Figure B2 (cont).

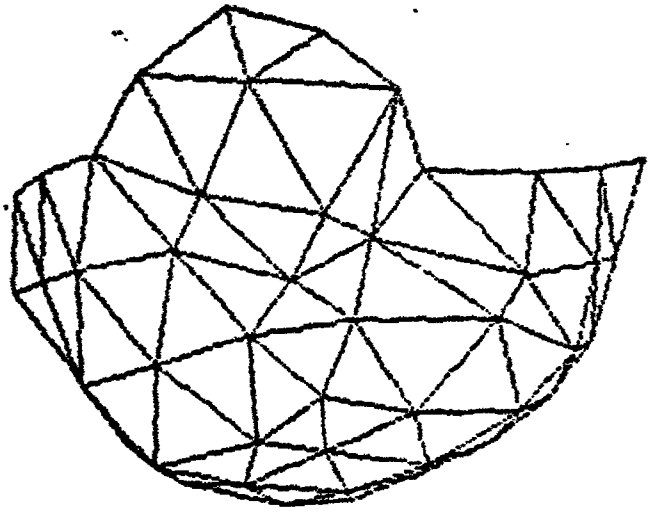

Mode 10 (A1)

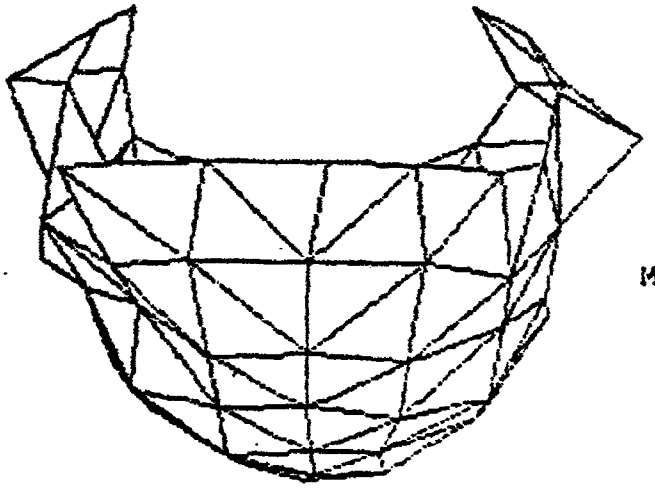

Mode 11 (A1)

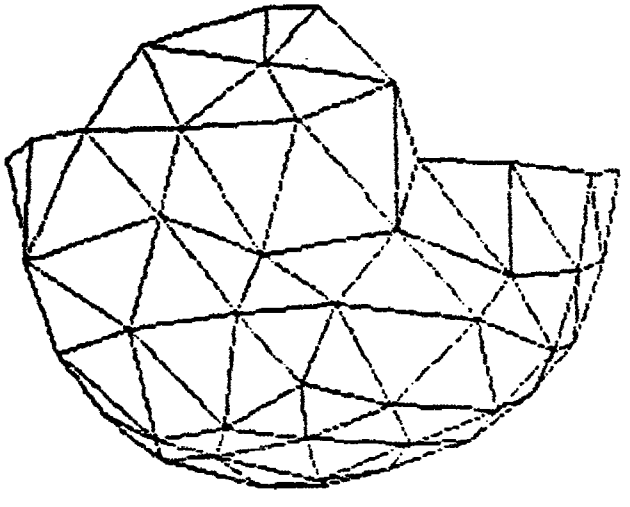

Mode 12 (A1)

Figure B2 (cont).

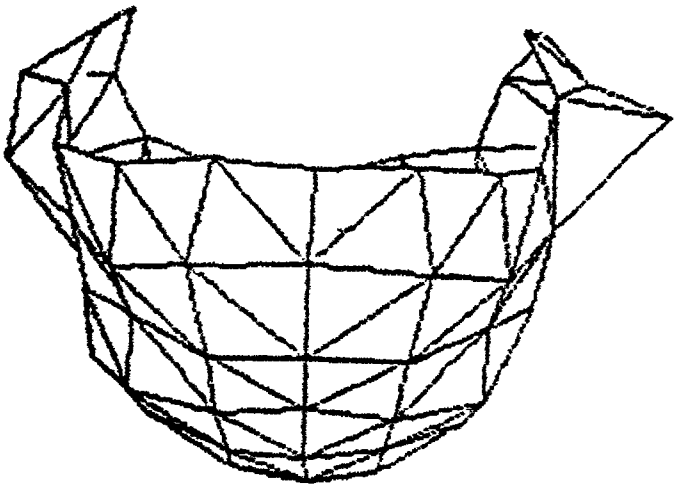

Mode 13 (A1)

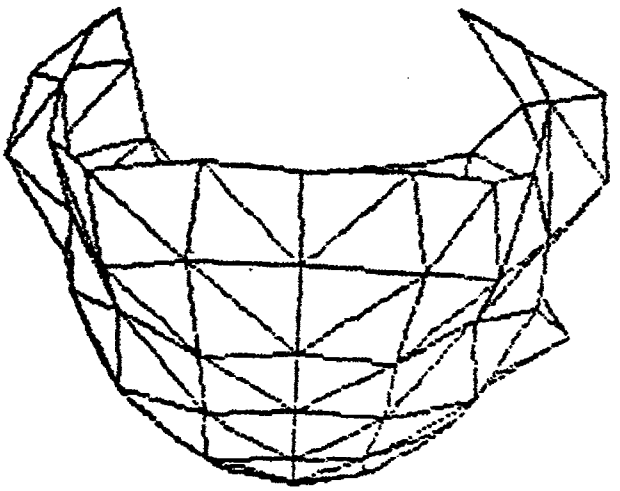

Mode 14 (A1)

Figure B2 (cont).

DISTRIBUTION LIST

4 copies	Commander US Army Medical Research and Development Command ATTN: SGRD-RMS Fort Detrick, Frederick, MD 21701
12 copies	Defense Technical Information Center (DTIC) ATTN: DTIC-DDA Cameron Station Alexandria, VA 22314
1 copy	Dean School of Medicine Uniformed Services University of the Health Sciences 4301 Jones Bridge Road Bethesda, MD 20014
1 copy	Commandant Academy of Health Sciences, US Army ATTN: AHS-CDM Fort Sam Houston, TX 78234